Micro-spot Two-photon Photoemission Spectroscopy Studies for Unoccupied Electronic Levels at Organic/Inorganic Interfaces

by

YAMAMOTO Ryota

Department of Chemistry, Graduate School of Science,

Osaka University

February 2012

Table of Contents

1. Introduction

The *electronic structures at interfaces* between inorganic substrates and functional organic films have attracted broad interest both in surface science and materials science [1-3]. Nowadays many basic researches of the interfaces are done from surface scientific approaches [4, 5]. *Photoelectron spectroscopy* (PES) has been a powerful tool to understand occupied electronic structure at surfaces [6]. Investigations by PES have been done in the past few decades and their results revealed important roles of the surface electronic structures as a channel of carrier transfers at the interfaces [7, 8]. One of the advantages of PES is direct observations of band structures by *angle-resolved* (AR) PES. Recent progress of two-dimensional electron analyzers enables easily to visualize band structures at the interfaces.

Despite of a lot of investigations of the occupied states, to understand unoccupied electronic structures at the interfaces is still a challenging issue [9-11]. Experiments on Unoccupied states at the interfaces are available by *Two-photon photoelectron spectroscopy* (2PPE) [12]. In 2PPE measurement, unoccupied states are temporally populated by a first photon and the excited states are detected by photoemission of excited electron with the second photon. The two-step process competes with the coherent 2PPE process from occupied levels. The two processes can be discriminated from photon energy dependence of 2PPE spectrum: When the photon energy is increased by $\Delta h\nu$, photoelectron energy from the two-step process increases by $1\Delta h\nu$ and that from coherent 2PPE process, by $2\Delta h\nu$. Thus we can measure the occupied and unoccupied levels at the same time. This method is superior to other method such as *inverse photoelectron spectroscopy* (IPES) and *photo absorption* or *emission spectroscopy* in the view point of high-energy resolution. Another advantage of 2PPE

experiments is direct observation of ultrafast dynamics by *time-resolved* measurements (TR-2PPE). By combining femtosecond pulse lasers with pump-probe spectroscopic technique, electron excitation and relaxation processes have been revealed in these two decades. It has been revealed that relaxations of hot-electrons by which excited inter- or intra- band transition in metal, is occurred in the order of 10 fs [13, 14].

To obtain reproducible results in 2PPE, well-ordered sample is required. However, one of the problems in the field of the interface electronic structure is the lateral inhomogeneity of organic films. Due to complicated substrate-molecule interactions and intermolecular interactions, growth of organic films is typically inhomogeneous, and the lateral inhomogeneity causes complexity in electronic structures and also in carrier transportations. In **chapter 3**, the micro-spot two-photon photoemission (micro-2PPE) spectroscopy in which fs-laser light is focused to sub-μm spot is applied to probe the inhomogeneity of the electronic structures [15, 16]. In the chapter it is shown that highly-resolved and well reproducible 2PPE spectroscopy for lead phthalocyanine (PbPc) film became feasible by the micro-2PPE method [17]. All molecule-derived occupied and unoccupied levels in the vicinity of the Fermi level (E_F) for the well-ordered one monolayer (ML) film formed on highly oriented pyrolytic graphite (HOPG) substrate are assigned. Also detected were the unoccupied *image potential states* (IPS) on the HOPG surface and on the 1 ML film. Photo-excitation processes between occupied and occupied levels were discussed in detail [18, 19]. In the following chapters, details of the nature of unoccupied states on PbPc/HOPG surface are discussed by using micro-scanning 2PPE and angle-resolved 2PPE study.

In **chapter 4**, the unoccupied electronic states on a sub-ML film are focused on [20,

21]. Environments of molecules in sub-ML films are less uniform than in the well-ordered 1 ML film. The fluctuation of the environment modulates the interface electronic structure. Especially, unoccupied levels are considered to be more sensitive to the environment than the occupied levels. Because of the anti-bonding character, the unoccupied molecular orbital extends to outside of molecule increasing interaction with neighboring molecules. The environment-induced modulations of occupied and unoccupied levels are investigated with micro-2PPE spectroscopy and with surface imaging. In the chapter we discuss how the unoccupied levels of PbPc film are affected by the lateral distribution of molecules is shown. It is revealed that the unoccupied levels are sensitive to surface morphology in nm-scale. The results points out the meaning of uniformity of the organic films.

In the latter part of this thesis **(chapter 5** and **6**), the main issue is that unoccupied levels on monolayer of organic films are *delocalized* or not. Band structures of metals and semiconductors (Si, Ge, GaAs etc.) have been one of the main issues of solid physics [22]. The reason is that band diagrams are essential to understand *electron* or *hole transportation*. In case of organic semiconductors, mobility of careers is strongly depends on the sample, even if the samples are same composition. For example, reported mobility values of pentacene OFET are spread to wide range; 0.01-40 $cm^2V^{-1}s^{-1}$ [23, 24]. Many factors evolve in the electron transportation and there is no consensus opinion about the mechanism of career transportation at organic/inorganic interfaces. To explain electron conductivity, two major mechanisms are proposed; *hopping* and band *conduction* [25]. In *hopping* mechanism, an excited carrier is localized to a molecular orbital and then transfer to neighboring molecules by diffusion, with overcoming barriers step-by-step. The mobility is determined by degree of the

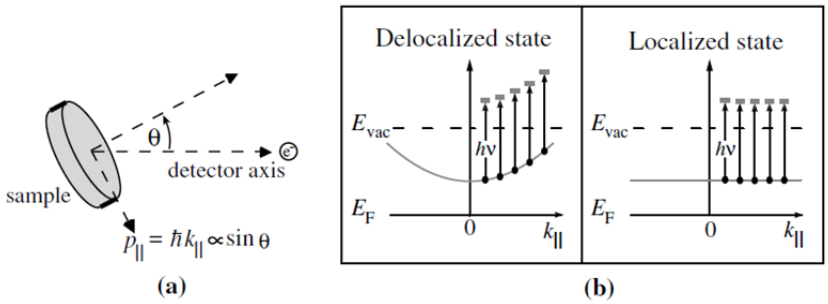

Fig. 1.1: These images are referred from ref. [41]. (a) Schematic diagram for the photoemission process of angle-resolved 2PPE. (b) The dependence of photoelectron kinetic energy on parallel momentum $\hbar k_{//}$ is illustrated for delocalized and localized states.

hopping integration and estimated lower than 1 $cm^2V^{-1}s^{-1}$. To explain high-mobility (> 1 $cm^2V^{-1}s^{-1}$), band conduction is a reasonable idea. In band conduction model, careers are delocalized and transports coherently, except Umklapp process. A Hall Effect measurement on an OFET, which made of single-crystal of rubrene, is reported [26]. Their result suggests that the band conduction model is suitable for explanation to their results. From angle-resolved measurement we can know that the electronic levels are localized ($k_{//}$ is not conserved) or delocalized ($k_{//}$ is conserved). UPS spectra show dispersion of HOMO level (hole) on pentacene and rubrene thin film surfaces [27, 28]. The results means that HOMO forms band and holes excited in the HOMO are delocalized.

We focus on the issue that localization or delocalization of the unoccupied states of the organic monolayers on substrates. *Angle-resolved* photoelectron spectroscopy (AR-PES or 2PPE) can be used to examine dispersions (see, **Fig. 1.1**). However, there are only few investigations about band structures of unoccupied states at organic semiconductors / metal interfaces by AR-2PPE [11, 29-35]. A common method to do AR-PES or -2PPE is conducted by tilting samples towards an analyzer and detects photoelectrons at different emission angles. The problem of this method is that the

positions of light spots may be changed. If the electronic structure is laterally inhomogeneous, it is difficult to get reproducible results. The other problem is difficulty of collection of low-energy electrons conserving information of their emission angle. Aberration of electron lens must be reduced for proper AR measurement. To obtain reproducible experimental results, newly-developed micro- AR 2PPE equipment is used [36].

In **chapter 5**, band structures of image potential states on HOPG substrate and on PbPc films are measured by this equipment. On the surface, unoccupied surface states which are called '*Image Potential States*' (IPS) are formed on. Their dynamics are extensively studied by TR-2PPE. Relaxation mechanisms of excited electrons on them are revealed [37-39]. In the cases of interfaces between dielectric layer and metals, electrons in which excited to unoccupied surface state are localized and stabilized after picosecond, because of reorientation of electrons in dielectric layers; solvation process [40-44]. The wave functions of Image potential states are localized between image potential and bulk band gap toward the surface normal direction, but delocalized toward the surface parallel direction. Thus their band structures are expected to be sensitive to surface structures. Owing to the high-energy resolutions of micro-spot AR 2PPE, details of IPS band structures on HOPG enable to discuss. Effects of the absorbed molecular films on IPS band structures are also discussed. A monolayer film of PbPc on HOPG is known for well-ordered structure [20, 45] and experimental results show strong influences of the periodic potential formed on band structures of IPS on the film.

In **chapter 6**, band structures of an unoccupied, molecular derived state on PbPc films are measured by micro-AR 2PPE. We studied dispersion of the L2 level (which derived from LUMO+2 state of the molecule) of a 1ML PbPc / HOPG surface. From

chapter 4, even if we measure dispersion of well-ordered organic films, the observed dispersion has position dependence. The results suggest that band structures of unoccupied level are sensitive to intermolecular interactions. AR Micro-2PPE can get reproducible dispersions by choosing the light spots on highly well-ordered domains. We can detect dispersion and discuss delocalization of the L2 from the dispersion. Furthermore, from intensity-wave momentum relation of photoelectrons from L2, momentum distribution of excited electrons in L2 is derived. From the distribution, we can know extent of wave function of L2 in real space.

Experiments in this thesis are one of attempts for understanding unoccupied states on organic / inorganic interfaces. There are only few knowledge is revealed in the PbPc/HOPG interfaces, however, I believe that further systematic study on various organic / inorganic interfaces will give clues for solid understand the nature of electron transportation at the interfaces.

2. Experimental setup and sample preparation

This chapter outlines details of experimental setups and sample preparations. It begins with descriptions of the employed techniques, two-photon photoelectron (2PPE) spectroscopy and angle-resolved two-photon photoelectron spectroscopy (AR-2PPE). Then our two types of "home-made", Micro-spot 2PPE equipment are presented. Details of optical setup, ultra-high vacuum (UHV) chambers and control systems for microscopy are included in the section. Last parts explain the ways of sample preparations.

2.1 Principles of Two-Photon Photoelectron Spectroscopy (2PPE)

2.1.1 One-Photon Photoelectron Spectroscopy (PES)

Photoelectron spectroscopy (PES) has been a powerful tool for investigating the electronic structure of solids [6]. Electron emission from solids occurs when the photon energy ($h\nu$) is higher than the vacuum level (E_{vac}). Measurements of kinetic energies and their emission angles enable to obtain initial energies of the electrons and dispersions parallel to the surface. Kinetic energies of photoelectrons are given by

$$E_k = h\nu - (\Phi - E_i) \qquad (2.1)$$

E_i (< 0) is the *initial energy* with respect to *the Fermi level* (E_F) and Φ (= E_{vac} - E_F) is called as the *work function*. The work function defined as a minimum energy for removing an electron from a solid. More accurately, Φ is defined as the chemical potential of electrons in solid. *Ultraviolet photoelectron spectroscopy* (UPS) is a popular method to probe density of states of valence occupied states. Important point of PES is its surface sensitivity. Shifts of the cut-off on the UPS spectra represent sensitivities of the work functions to their surroundings. The curve of the **Fig. 2.1** shows that in the

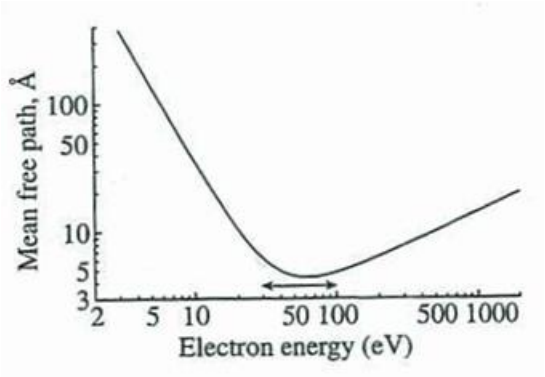

Fig. 2.1: 'Universal curve' showing, schematically how the inelastic mean free path of an electron in a solid varies with its kinetic energy, from ref. [46]. The double arrow indicates the range where surface sensitivity is greatest. To obtain accurate values of the inelastic mean free path, see ref. [46].

range of 10 - 100 eV, which is the usual range of measured kinetic energies for the valence band spectroscopy, the escape depth of electrons is of the order of few Å. The requirement for ordered, clean surfaces is very strict. The experiments are therefore conducted in the ultra-high vacuum environment (UHV) and the surfaces are specially prepared before the measurements, depending on the sample, by cleaving, annealing, scraping or similar. The measured electronic states are relevant only for the first few atomic layers of the material. Low-dimensional layered materials with weak bonds between layers – and no surface reconstruction – are therefore particularly suited for the PES measurements. Many detailed overviews of photoemission techniques can be found in the literature.

2.1.2 Two-Photon Photoelectron Spectroscopy (2PPE)

The application of *two-photon photoelectron spectroscopy* (2PPE) enables the study of the unoccupied band structures in addition to occupied states [12]. The principle of this technique is shown in **Fig. 2.2**. By absorption of a first photon (pump), an electron below the Fermi Level (*initial state*) is excited to a normally unoccupied level (*intermediate state*) below E_{vac}. A second photon (probe) excites the electron above the vacuum level (*final state*), where it can be detected by an electron energy analyzer. If a same energy of photon for pump and probe pulse is used, it is called *one color* 2PPE. In

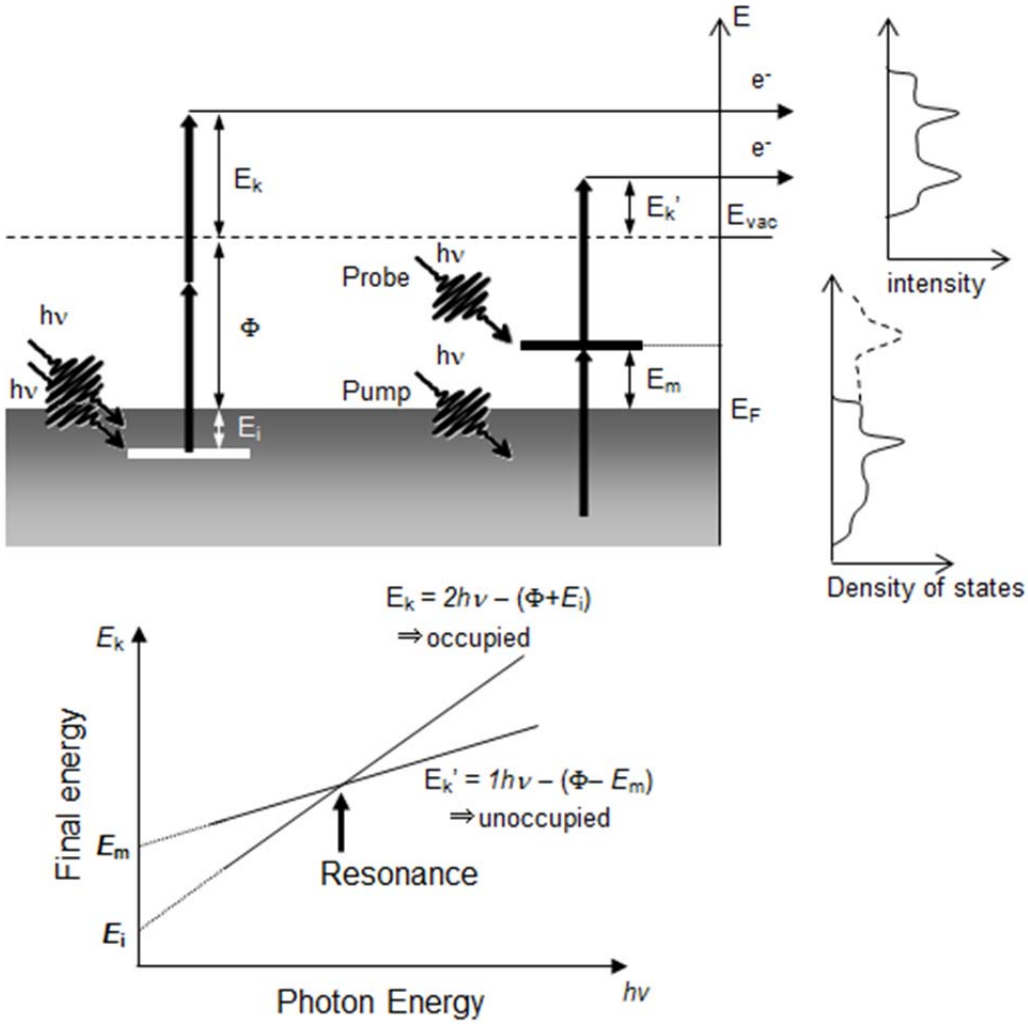

Fig. 2.2: Two processes of 2PPE; (a) 2PPE from unoccupied level E_m and (b) coherent 2PPE from occupied level are shown. (c) Photon energy dependence of observed level. When the energy positions of observed peaks were plotted against the photon energy, the structure of occupied and unoccupied levels are aligned the slope of 2 and 1, respectively, related with the photon energy. Another remarkable point is the resonance at $h\nu = E_m - E_i$. At the resonance, 2PPE signal is resonantly enhanced.

the condition of *two-color* 2PPE, different energies of photon is used for the pump and the probe pulse. For the efficient excitation of electrons to intermediate states, the right choice of photon energy is very important. Transition probability is an important factor like other optical absorption spectroscopic methods. Studying the dynamics of excited electrons with femtosecond time resolution can be possible by using ultra-short laser

pulses with durations less than 100 fs. All experiments in this thesis were done in the condition of zero-delayed one color 2PPE.

We must consider photoemission pathways from its initial state via an intermediate state to its final state. Two different excitation mechanisms are shown in **Fig. 2.2**. "*The two-step process*" competes with "coherent 2PPE process" from occupied levels. "*The two-step process*" depicts resonant excitation to a "*real*" intermediate state. The second photon probes transient population of the intermediate state. In "coherent 2PPE process", no resonant intermediate state is available. Electrons leave the sample directly in a two-photon absorption, which occurs within the pulse duration. It is called via "*virtual*" intermediate states; which are not occupied for a finite time. These two processes can be discriminated from photon energy dependence of 2PPE spectrum. When the photon energy is of pump and pulse is the same and increased by $\Delta h\nu$, photoelectron energy from the two-step process increases by $1\Delta h\nu$ and that from coherent 2PPE process, by $2\Delta h\nu$. Thus we can measure the occupied and unoccupied levels at the same time. If photon energy is corresponding to E_m - E_i, 2PPE signal is resonantly enhanced by interference of these two processes. The energy resolution of 2PPE is better than 30 meV, superior to the resolution of *inverse photoelectron spectroscopy* (IPES); a common method to measure unoccupied energy levels. Note that IPES gives only an anionic state as a final state, but 2PPE can detect both of a natural excitation state and an anionic state (via charge transfer at the interfaces).

2PPE has been widely applied to probe image potential states above surfaces and dynamics of hot-carrier on metal or semiconductor surfaces [9-14]. But 2PPE has been applied to few investigations focused on the unoccupied states in functional organic thin-films [11, 29-35].

2.1.3 Angle-resolved 2PPE (AR2PPE)

Photoelectrons are collected with a detector, in which their kinetic energy and momentum are counted. If we gather both of momentum and energy information, we call the measurement, *angler-solved photoemission spectroscopy* (AR PES) [6]. In the case of collection only on energy, we call it angle-integrated PES, explained at **section 2.1.1**.

A typical AR PES experimental setup is shown in **Fig. 2.3**. Photoelectrons ejected by the monochromatic light are collected by the analyzer that gathers them as a function of energy and angle. Single channel analyzers usually collect intensity as a function of kinetic energy repeatedly for several emission angles by tilting the sample. Owing to recent progresses of electron analyzer, Energy and angle resolutions of UPS are drastically improved. A two-dimensional analyzer, that can collect (θ, E_{kin}) maps in a certain energy-angle window at once, is available now. As a result signal-to-noise ratio is improved. In the AR PES, if there is no scatter inside the solid, electrons conserve the "*energy*" and "*parallel momentum*" during photoemission process. The momentum perpendicular to surface is not conserved due to the refraction. New wave-variable light sources such as lasers and synchrotron radiations enable to investigate dispersions perpendicular to the surface, but it is challenged tasks. The two operational relations are

$$E_{kin} = h\nu - \Phi - E_i \qquad (2.2)$$

$$|k_{//}| = \sqrt{(2m_e E_{kin})} / \hbar \times \sin\theta = 0.512 \sqrt{(E_{kin})} \times \sin\theta \qquad (2.3)$$

m_e is mass of an electron, and $h\nu$ the photon energy. Kinetic energies of electrons reflect their initial energy, as Equation 2.2. Equation 2.3 gives momentum in $Å^{-1}$, if kinetic energy E_{kin} in eV is given. The first equation demonstrates that electrons have to overcome a potential Φ to escape from the surface. Equation 2.2 is simplified for the

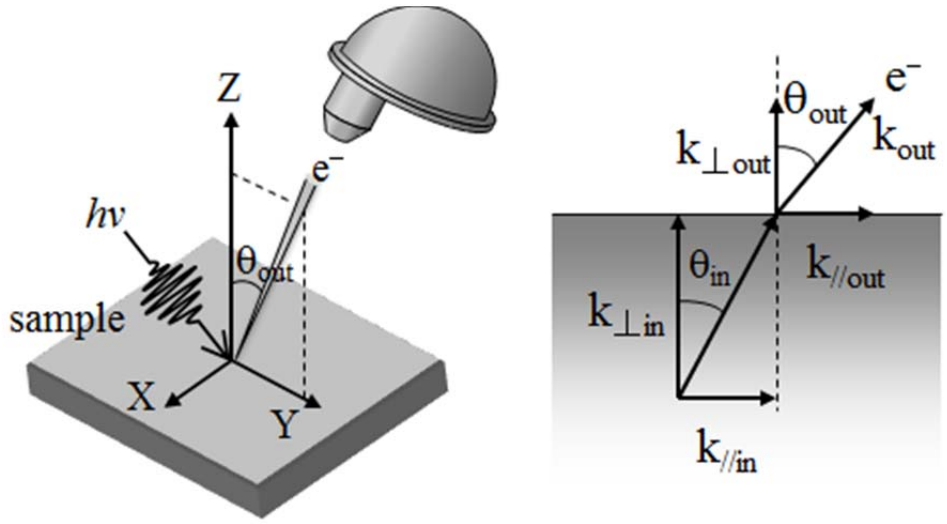

Fig. 2.3: Illustration of an ARPES experiment. Photoelectrons are emitted from the surface and collected with an analyzer as a function of the emission angle and kinetic energy. The obtained information is usually summed up in intensity maps. Spectra can be analyzed in two equivalent representations - as energy distribution curves, or as momentum distribution curves.

following reason. The Fermi energy E_F corresponding to $E_i = 0$ is determined by the work function of the analyzer. By measuring the Fermi edge on a metallic sample we can calibrate the instrument to take measurements in binding energy directly since it does not depend on the sample. Note the sample has to be in electrical contact with the analyzer. Equations 2.2 and 2.3 underline two important requirements on the photoemission experiment. One requirement is obtained from Equation 2.2; the sample "must" be grounded, and to the same ground as the analyzer. As photoelectrons leave the surface, there has to be a compensating current of electrons that prevents charging of the surface. If charging of the surface may occur, external electronic fields are formed, and speed of the photoelectrons is changed. The other requirement is obtained from Equation 2.3; "absence of magnetic fields" is required. Magnetic fields would interfere with trajectories of photoelectrons. All the materials inside main (analyze) chamber have to be demagnetized and sample holders made from preferably nonmagnetic metals. Conversion obtained (θ, E_{kin}) maps to (k, E_{kin}) maps by using equation 2.3 enables to

obtain dispersion relations. Note that equation 2.3 has a non-linear relation of θ to the emission angle and the kinetic energy E_{kin}. We are interested in the electronic states in the material, initial (occupied) states or intermediate (unoccupied) states of the electrons. 2PPE process involves the transition from the initial state, via intermediate state, which may or may not be available, to a final state. These processes also depend on their symmetries. Obviously, the interpretation of AR 2PPE results is not straightforward for many reasons; the influence of final state effects or dynamics of intermediate state may beyond the single-particle interpretation. We must consider such effects to interpret obtained results.

2.2 Experimental setup1: Micro-spot 2PPE (Chapter 3, 4)

2.2.1 Ultrahigh vacuum chamber system

Outlines of main UHV chamber is shown in **Fig. 2.4**. Their outer wall was shielded from external magnetic field by μ-metal. It is equipped an electron energy analyzer (VG100AX), quadruple-mass spectrometer to confirm the impurity of UHV. Samples is mounted a high-precision stage, described in section 2.2.5. Incident window of laser light is made of lithium fluoride (LiF). LiF highly transmit UV and VUV light. we adopt this material, considering to perform PES measurement using vacuum ultraviolet laser light (8.86 eV). The chamber is vacuumed by a turbo molecular pump. Base pressure of the main chamber was generally better than 1×10^{-10} Torr. For microscopic measurement we must turn off the turbo molecular pump, to avoid vibration of sample stage. During microscopic measurement, an ion pump and a titan getter pump is used to keep base pressure below 3×10^{-10} Torr. For micro-UPS measurement, we need to generate VUV lights. In our experiment, third nonlinear optical effect of Xenon gas is

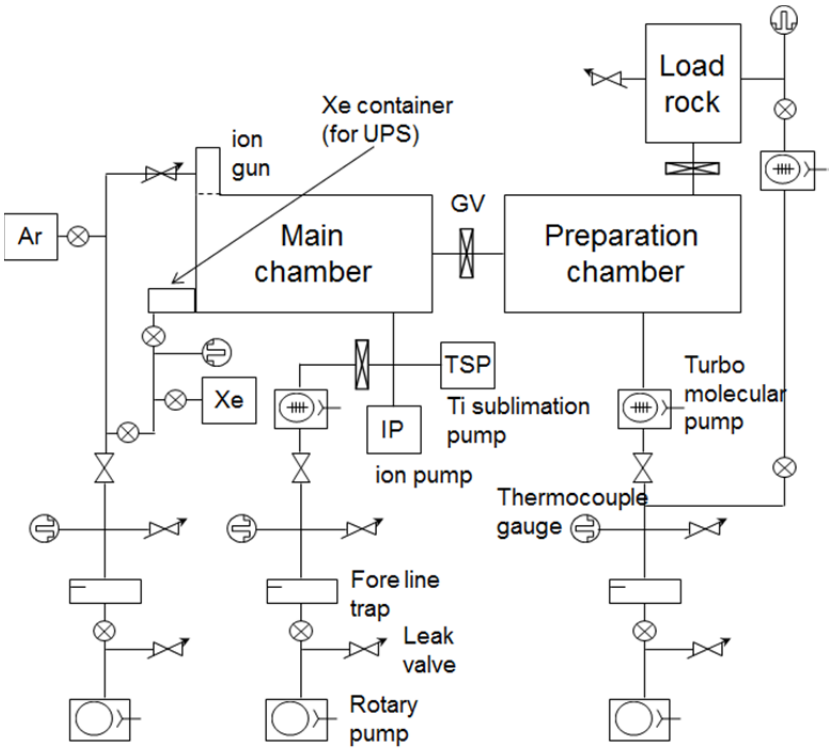

Fig. 2.4: UHV system of micro-2PPE equipment is shown. To achieve ultra-high vacuum, each turbo molecular pumps are combined with a rotary pump. A titanium sublimation pump is equipped in main chamber to reduce remaining gas (water, hydrogen etc.). The main chamber is evacuated by a ion pump and the turbo molecular pump is turn off during measurements, to reduce mechanical vibration. An Argon gas cylinder is connected to an ion gun, used for sputtering of metal samples during sample cleaning processes. A Xenon gas cylinder is connected to a container in which 6^{th} harmonics laser output is formed by nonlinear optical effects. The container must be evacuated to reduce oxygen which absorbs VUV lasers.

used to generate VUV light. Oxygen absorb VUV light, therefore, Xenon gas container is vacuumed by a rotary pump.

A preparation chamber is separated from the main chamber, to avoid contamination of main chamber during deposition process of organic molecule. The preparation chamber is equipped material source, quartz microbalance (INFICON, IC/5) to monitor film thickness, and transfer rod. The preparation chamber is connected a load-rock chamber. Thus samples can be loaded without breaking vacuum of the main and the

preparation chamber. The Preparation chamber and the load-rock chamber are pumped by separate turbo molecular pumps, respectively.

2.2.2 Laser system

The optical setup is described in **Fig. 2.5**. The light source is p-polarized frequency tripling of tunable titanium-doped sapphire (Ti: Sa) laser output. The fs-laser pulses are generated in a commercial laser system; Mira 900-F (Coherent). The laser oscillator is pumped by frequency doubled Neodymium Yttrium Vanadate (Nd: YVO4) laser (Coherent, Verdi V-6). Mode-locked titanium sapphire laser can generate tunable ultra-short pulse. Pulse repetition rate of the laser is 76 MHz. Pulse durations of fundamental output are ~150 fs, measured their autocorrelation. The photon energy region of the TH was 4.13~4.77 eV. The power of the incident light was reduced to 0.2 nJ par pulse in order to avoid surface destruction. Details of third harmonics generation is described in the following section.

2.2.3 Third harmonic generation

A commercial third harmonics generator (inrad, model 5-050) is used for frequency tripling of laser output. Details of *third harmonic generation* (THG) will be show in **section 2.3.3**, brief explanation is only shown here. Optical configuration of the generator is shown in **Fig. 2.6**. The output pulse of Ti: Sa oscillator is focused to a LBO crystal (t = 2.0 mm) to generate the second harmonics. Fundamental wave (FW) and frequency doubled wave (SH) is divided by beam splitter. Fundamental outputs pass a delay stage to compensate group velocity dispersion. FW and SH are combined again. After passing $\lambda/2$ wave plates, these waves has same polarization plane. These lights are focused to a BBO crystal (t = 0.5 mm), the third harmonics (TH) is generated.

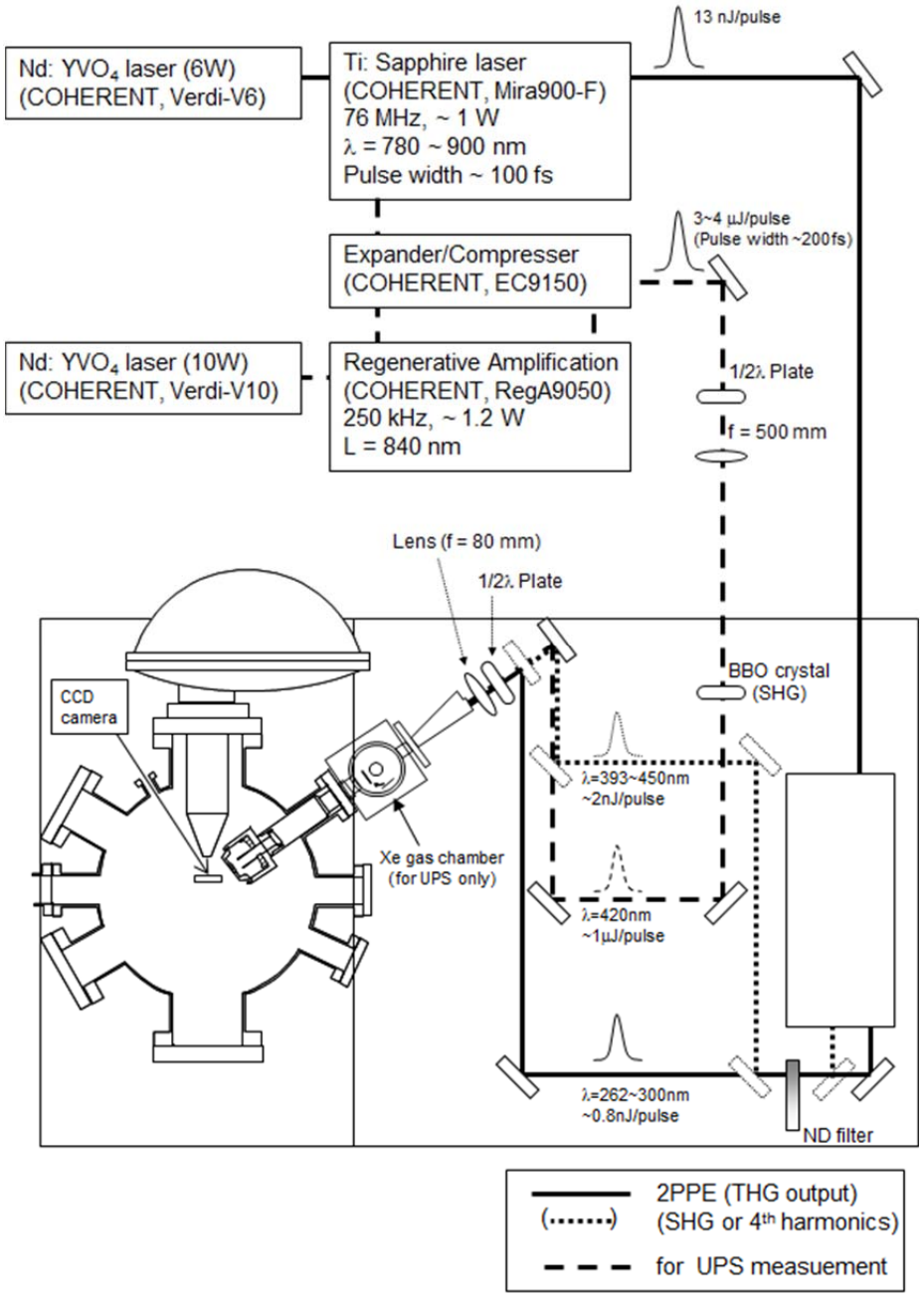

Fig. 2.5: Laser pathway of the Micro-2PPE equipment is shown. Two type of experimental method (2PPE/UPS) is enabled. For 2PPE experiment, laser output is converted to SHG and THG. To check sample position is the focal point of the light, we incident SHG and check light spot by a CCD camera. After that THG output is incident passing the same pathway and SHG is shuttered. For UPS measurement 6^{th} harmonics output is required but the efficiency is very low. Therefore, laser pulse must be enhanced by a regenerate oscillator. SHG, generated by a BBO crystal is also used to determine sample position. After that Xe gas container is pressed before the incident viewport. In the container, the 6^{th} harmonic is generated and separated to SHG by passing a band-pass filter.

2.2.4 Objective Mirror for microscopic measurement

The third harmonic output (UV light) enters the main chamber through a LiF window, and is then focused onto a sample surface by a Schwarzschild objective of 0.29 numerical apertures. Advantages of using objective are, (1) there is no chromatic aberration, (2) big mirror has large numerical aperture, as a result, small spot size at the focal point is achieved. Configurations of optics are shown in **Fig. 2.7**. The objective consists of a pair of aluminum-coated mirrors, mounted in a Cu–Be housing. Graphite is coated on the surface of the housing. The objective is fixed in UHV chamber. The incident angle was 55º from the surface normal. The focal point is 40 mm from the front surface of the objective. The diffraction-limited spot diameter of the 280 nm wavelength light is estimated to be 0.6 μm. If laser light is gauss beam, the intensity of 2PPE process is represented as a gauss square. Thus lateral resolution of micro-spot 2PPE is determined; the lateral resolution is 400 nm, a factor of √2 smaller than the diffraction limited diameter of the laser spot. This is ultimate value for the lateral resolution of the present system. From geometrical restriction, the first mirror of objective reflects light in center of optical axis. Laser beam can be regarding as a gauss beam, intensity takes maxima at center of optical axis and intensity is drastically decreased at off-center position. Thus we must optimize size of the incident laser beam. A lens (f = 80 mm) is used to expand the beam size. The position of the lens can be calculated to have same focal point to the objective mirror. From our empirical trial, the size of incident UV light is around 15 mm at the incident LiF window of main chamber. To check the beam size, a paper with fluorescent ink is put in front of LiF window, and the size of fluorescence spot is checked. The laser pathway is checked by a rotatable small copper plate with fluorescent ink. The incident laser beam forms doughnut pattern on the plate.

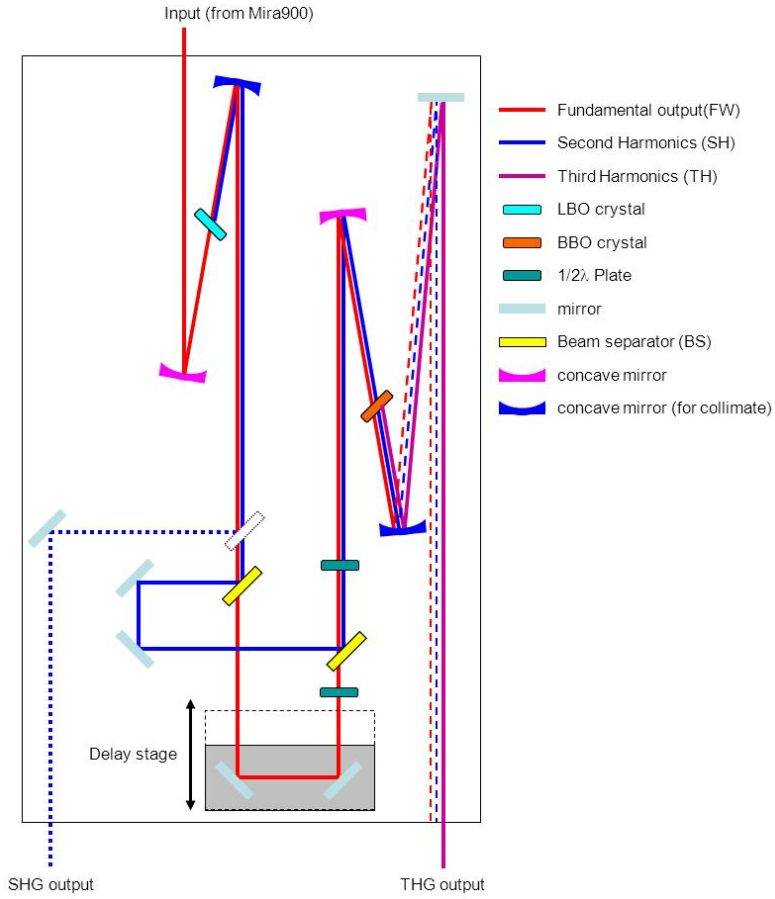

Fig. 2.6: Configuration of optics in the THG generator (inrad, 5-050) is shown. Laser pulses are focused to the first BBO crystal to generate second harmonics. Fundamental and second harmonic pulses are passing delay stages and a polarization plate to penetrate delay and coincidence the polarization. Both pulse are focused on the second BBO crystal, then Third hermonic pulses are generated.

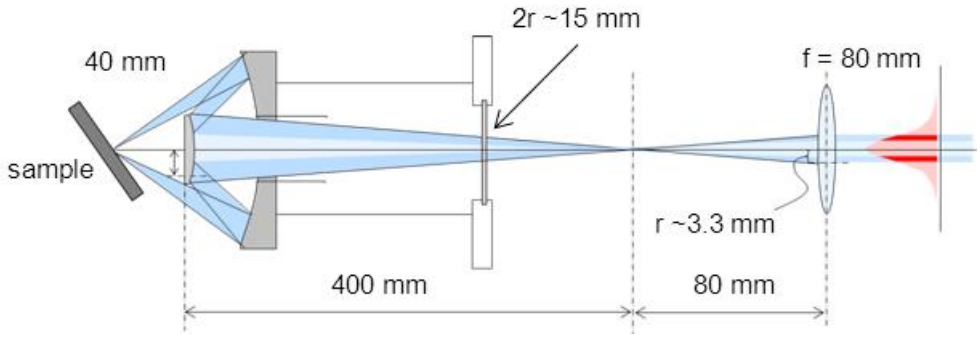

Fig. 2.7: Optical configuration of Schwarzschild objective mirror is shown. The objective mirror is composed of two sapphire mirrors with aluminum coating. These mirrors are bonded to mirror holder (made of beryllium copper) in the UHV chamber. To avoid electronic field by charging effect of dielectric parts, the mirror holder is coated by graphite. The incident laser light is regard as a gauss beam (the intensity curve of a gauss beam is drawn by pink polygon). Intensity of light axis is strong; however, light near axis is reflected by the first mirror. Only red part is reach to the sample. Thus, we must optimize to the size of laser pulse before the magnifying lens to maximize the intensity of photoelectron.

2.2.5 High-precision stage and sample holder

High-precision positioning and scanning of a sample in ultrahigh vacuum (UHV) is an indispensable requirement for investigations to laterally-inhomogeneous surfaces. The sample should be translated over a few mm in vertical and horizontal directions (denoted as X- and Y-directions, respectively) to find an area of interest. The area is found by long and precise translations from a suitable mark on the sample. Stepping

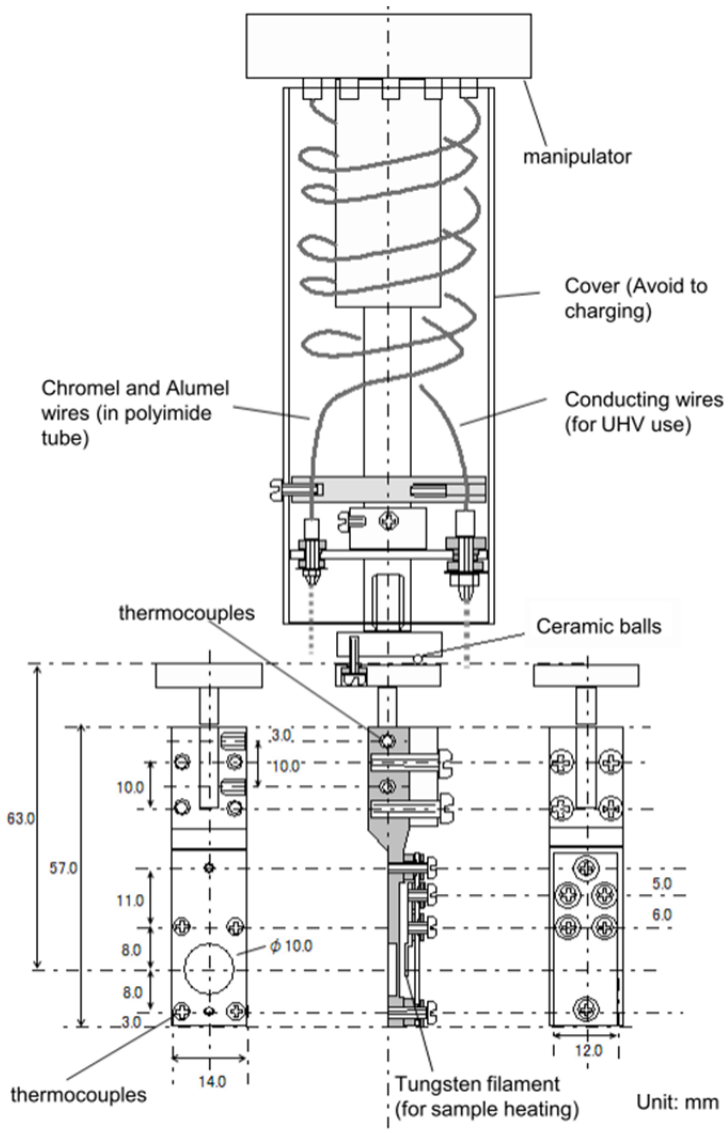

Fig. 2.8: The sample holder is illustrated. The sample holder is consisting of oxygen free copper and tantalum screws. Each part is insulated from the vacuum by ceramics parts. The ceramic insulator, conducting wire and thermocouple wires are covered by metal covers to avoid charging effects which effect on 2PPE measurements.

motor system has benefits for high power and long range movement compare to other precise motors, such as piezo actuators. The error of the positioning should be smaller than the spot diameter of the focused light (300 nm), that is, the accuracy of positioning should be better than 100 nm. In our micro-UPS, we used a partially upgraded standard UHV manipulator (VG, OMNIAX); actuated by step motors placed outside of UHV. This makes baking of UHV system easy. A typical sample holder for photoemission experiments is connected on the end of the manipulator. The resolution of the sample translation was improved by mounting two sets of step-motors with glass scales. The resolution of 0.1 μm was achieved. But the vertical accuracy of repeated positioning was poorer than that of horizontal, maybe because of thermal drift was inevitable. We can do heating or cooling samples for sample preparations; however, the measurement condition is limited at room temperature. In order to improve the performance, the new stage was constructed. But an old type of stage is still used during works in the thesis. Manipulation for the direction (Y-direction) to an analyzer is done manually, using a micrometer, originally attached to the OMNIAX. The Y-direction is adjusted to set the sample surface at the focus of the light with precision of < 3 μm, because the length of the beam waist of the light is about 3 μm. By checking 2PPE signals (derived from electronic structure of sample, not secondary electrons), we adjust a sample at the focus of the light. The manipulator can manually rotatable in θ direction; we can tilt a sample towards analyzer. But because of limitations of the focus of the light, to obtain a lateral image due to electronic structure, the sample must be perpendicular to analyzer (within ± 1°).

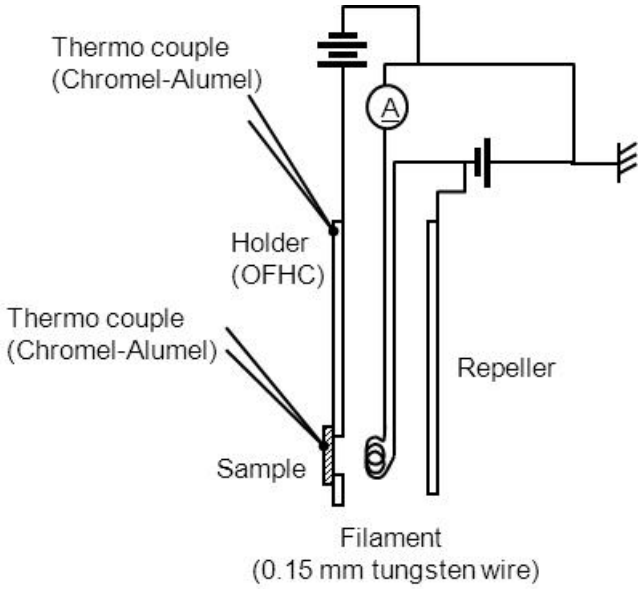

Fig. 2.9: Circuit around the sample holder is shown. A sample is heated by bombardment of electron; thermal-electrons emitted from a filament, accelerated by bias voltage (150 V), reach to sample.

A sample holder is connected to the stage. Their appearance is shown in **Fig. 2.8**. The sample is inserted to a sample holder; made of copper. The holder is insulated from the ground. They has a sample heating circuit; shown in

Fig. 2.9. Thermo-electrons are emitted from a tungsten filament, accelerated by bias voltage (~150 V), and bombard to a sample career from backside to a sample. The sample is heated and their maximum temperature can be achieved to 700 K. All insulate parts of the sample holder is covered by metals to avoid charging effects in 2PPE measurement processes.

2.2.6 Hemispherical electron energy analyzer

A hemispherical electron energy analyzer (VG100AX) is used for the detection of the photoelectron. Time of flight (TOF) spectrometer is also popular for 2PPE experiments, but there are advantages of using hemispherical analyzer for 2PPE of organic films. Organic films are easily damaged by laser radiation, thus we must reduce maximum intensity of laser pulse. So, laser systems must have high repetition rate to collect many electrons, however, TOF spectrometer has limitation for responsible time. Hemispherical analyzer has no limitation, like this. Another advantage of the

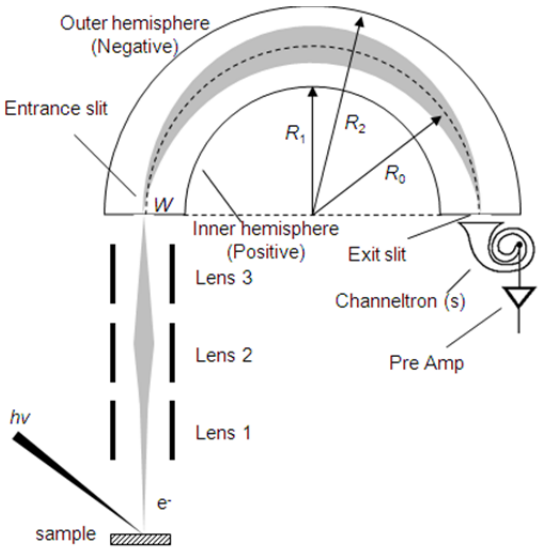

Fig. 2.10: Schematic image of the hemispherical energy analyzer is shown.

hemispherical type is its constant energy resolution. Energy resolution of TOF type is depend on the electron energy. A schematic image of a hemispherical analyzer is shown in **Fig. 2.10**. Energy resolution of a hemispherical analyzer, ΔE, is given as

$$\Delta E = \frac{W}{2R_0} E_0$$

where W is width of entrance slit, R_0 is average radiuses of outer and inner hemisphere, and E_0 is energy of passing hemisphere (pass energy). If energy of electron is different from E_0, they can't pass through the hemisphere. An acceptance angle for photoelectrons of the analyzer is speculated around ~4°. The pass energy is set to 3 eV. Photoelectron spectra are obtained by varying voltages of electrostatic lens at entrance. Monochromatic photoelectrons through the exit slit are amplified by a channeltron, and detected.

Whole energy resolution of Micro-spot 2PPE is determined from the band width of the laser pulse (18 meV) and energy resolution of the analyzer (20 meV). The total energy resolution of Micro-spot 2PPE is $\sqrt{(18^2 + 20^2)} = 27$ meV.

2.2.7 Control system

In the Micro-spot 2PPE, 2 types of measurement are done; energy spectrum mode

and lateral imaging mode. To obtain those data, several devices are connected to a GPIB port; an A/D- and D/A-converter (Stanford Research systems, SR-245), a photon counter (Stanford Research systems, SR-400), and a stage controller (Sigma Tec, FC-101). These devices are controlled by BASIC programs running on a MS-DOS operating system (NEC PC98-01), see **Fig. 2.11**.

In energy spectrum mode, we scanning (5 mV/step, 1000 steps) applied voltage of an electronic lens of an analyzer, to select energy of photoelectron. Photoelectron is amplified by a channeltron and their intensity is integrated by a photon counter. 60 ms of integration is done at one data acquisition. To improve signal-to-noise ratio, scanning process is repeated more than 5 times.

In lateral imaging mode, energy selection of photoelectron is done manually or automatically. Detection areas are changed by scanning a sample (light spot is fixed). The scanning process is like this; vertical scanning of the stage is done at first, the stage goes back to start point, then 1 step moving in horizontal direction is done. 300 ms of data acquisition is done at each position, only one tome. To ensure sufficient measurement and check time evolution, however, several scans are done in the same place. The measurement time is increased due to dead-times during stage movement and repeated feed-back process for assuring sample position. Scanning speed of the sample is usually 50 μm/s, deformation of the stage is not so serious. It takes 15 minutes to obtain a lateral image of 30×30 scanning steps in a typical measurement. (There is no obvious time difference depending on their sizes.)

A Hemispherical analyzer measures energy of photoelectrons by applying voltage on electrostatic lens part. Energy of detected photoelectron is referenced to the vacuum levels of the analyzer. Thus the vacuum level of a sample must be higher than the

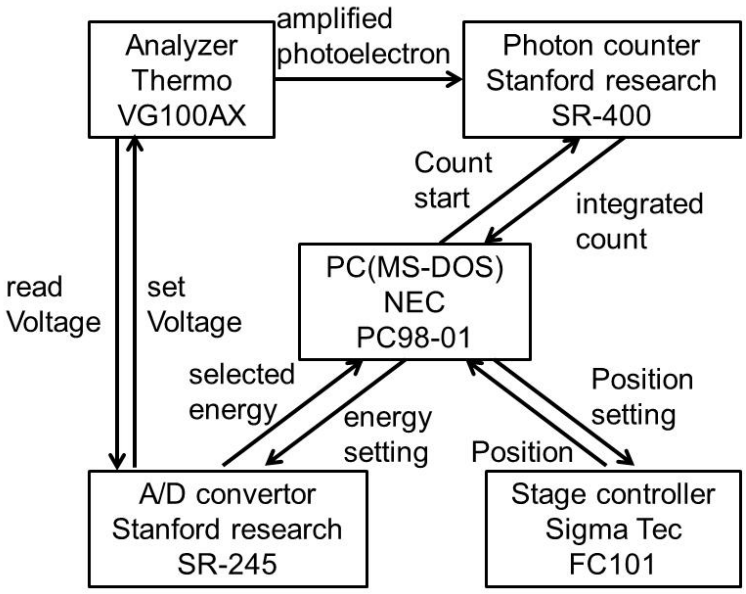

Fig. 2.11: Schematic sketch of the control systems of Micro-2PPE. Photoelectron measurement and sample manipulation are performed by a MS-DOS based PC.

vacuum level of the analyzer for whole measurement, so that the slowest photoelectrons are detected. If we need to 2PPE measurements samples with lower work functions than the analyzer, applying a bias voltage between sample and the analyzer is needed. Deposition of organics usually lowers the work function of the sample; we applied to bias voltage of 1 V, to ensure correct measurement condition.

2.3 Experimental setup2: AR Micro-spot 2PPE (Chapter 5, 6)

2.3.1 Ultrahigh vacuum chamber system

Outlines of main UHV chamber is described in **section 2.2.1**. The electron energy analyzer is replaced to a two dimensional, display type analyzer. The detail of the analyzer and angle resolved measurement is written in **section 2.1.3** and **2.3.4**.

2.3.2 Laser system

For AR Micro-spot 2PPE measurement, the fs-laser pulses are generated in a

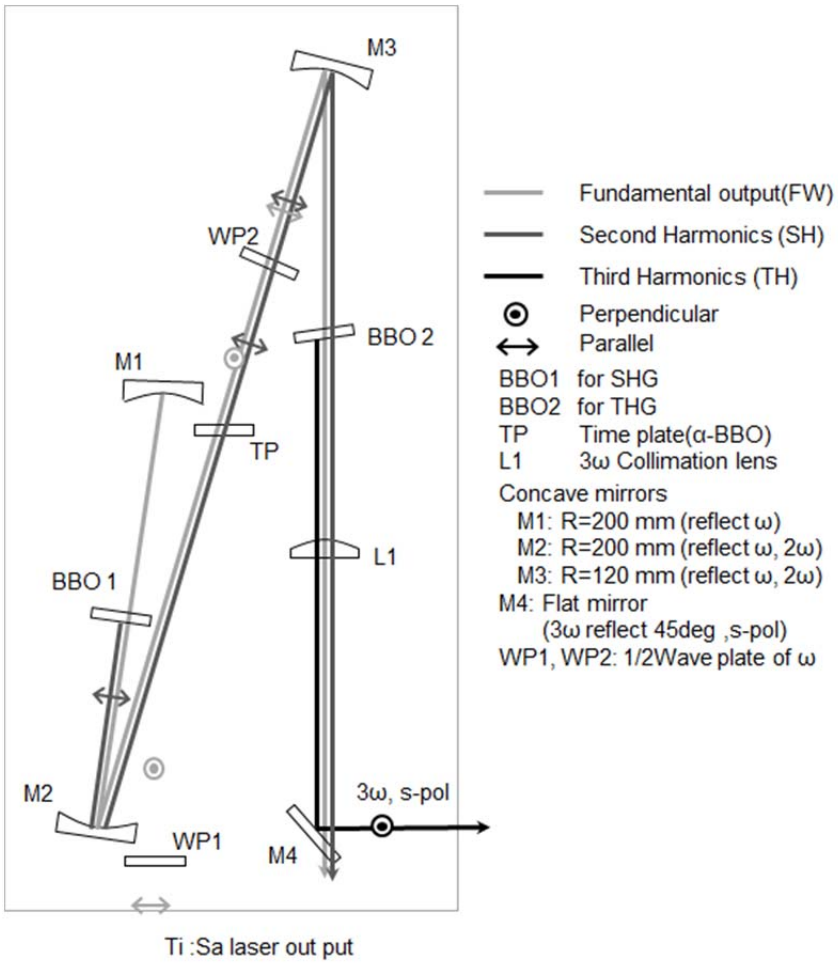

Fig. 2.12: Optical configuration of a 3rd Harmonics generator. The Third Harmonics is generated by a couple of BBO crystals. Phase matching between the fundamental waves and the Second Harmonics can be achieved by time plate without a delay stage. Third Harmonics is separated and introduced to the sample through quartz UHV window.

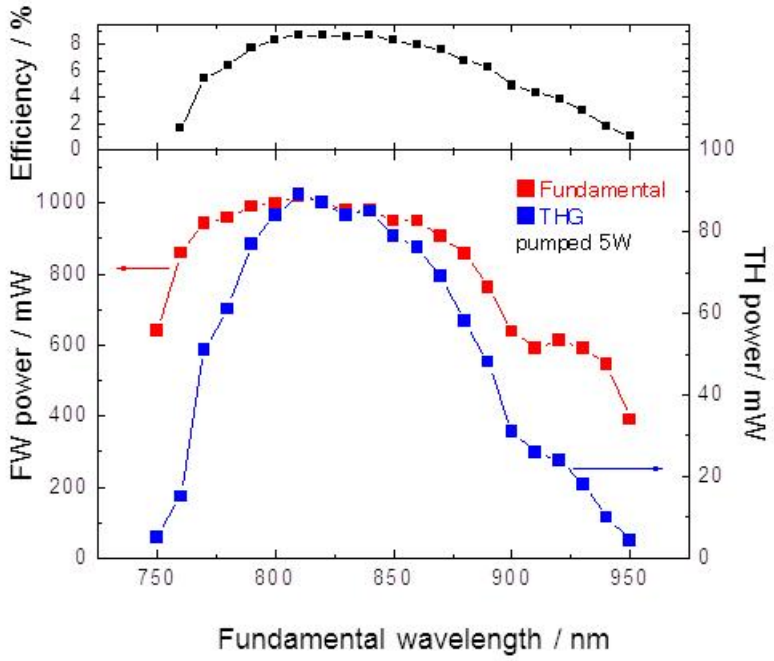

Fig. 2.13: Powers of the Fundamental outputs (red squares) and Third Harmonics (blue squares) are plotted against wavelengths of fundamentals. Conversion efficiency (black squares) is also indicated.

commercial laser system; “Maitai” (Spectra Physics). Pulse repetition rates of the “Maitai” are 80 MHz. Pulse durations of fundamental output are ~120 fs, measured their autocorrelation. The photon energy region of the TH was 4.04~4.77 eV. The power of the incident light was reduced to 0.2 nJ par pulse in order to avoid surface destruction. We used a “home-made” THG generator to generate UV pulse. Details of third harmonics generation is described in the following section.

2.3.3 Third harmonic generation

The third harmonic generation (THG) for 2PPE light source is generated by a couple of nonlinear crystals, β-BBO. **Fig. 2.12** shows the optical configuration of home-made TH generator. The output pulse of Ti: Sa oscillator is focused to the first BBO crystal (type I, θ = 27.18°, thickness of 1.0 mm) by a dielectric concave mirror (M1, r = 200 mm) to generate the second harmonic generation (SHG) of fundamental wave (FW). After SHG and transmitted FW are collimated by a dielectric concave mirror (M2, r = 200 mm), Polarization and time delay between the SHG and FW are compensated each other by λ/2 wave plate (WP2) and time plate (TP; α-BBO). Then both pulses are focused again to the second BBO crystal (type I, θ = 40.80°, thickness of 0.5 mm) by a dielectric concave mirror (M3, r = 120 mm). Collimated THG is separated for FW and SHG, and is guided to the UHV chamber. Conversion efficiency of THG is ~8 % at 840 nm; Fundamental output of 980 mW converted to THG of 76 mW. Relations of powers of fundamental outputs and THG outputs are shown in **Fig. 2.13**.

2.3.4 Micro-spot AR 2PPE

All measurements are performed in a newly developed micro-spot AR-2PPE spectrometer. The third harmonic output of a titanium sapphire laser is focused onto the sample surface with a Schwarzschild objective of 0.29 numerical apertures. The light

source was p-polarized. The incident angle is 65º from the surface normal. The spot size of incident light at the sample is close to the diffraction limited diameter of 0.6 μm, and achieves lateral resolution of 0.4 μm in 2PPE experiment. Photoelectrons are detected with an angle-resolved hemispherical energy analyzer (SCIENTA; R3000). In micro-spot 2PPE experiment, several procedures are required to record correct angle resolved results. The position of the light spot is determined by the Schwarzschild objective. The electron lens of the analyzer should be adjusted to the focus point. The kinetic energy of electrons in 2PPE is smaller than 5 eV, thus the electron lens of analyzer should properly collect low energy electrons. In optimized condition, the usable acceptance angle is about ±7° in the micro-spot AR 2PPE setup. Aberration correction at energy region smaller than 2 eV is not accomplished as yet. The whole of measurement was done with zero bias voltage between sample and analyzer in order to avoid the electronic field between sample and the tip part of the analyzer.

2.3.5 Data analysis

Hemispherical electron energy analyzer is frequently used for the detection of the photoelectron. Note that field-free measurement is must for angle-resolved 2PPE. It is necessary to apply a bias voltage that is sufficient to cancel out the work function difference between sample and spectrometer.

2.4 Sample preparation

2.4.1 Substrate; HOPG

HOPG, well-ordered polycrystalline graphite crystal, is used for standard sample of scanning probe microscope (SPM). HOPG takes two dimensional layer structures. The ideal construction of graphite crystal is shown in **Fig. 2.14**. Weak van der Waals

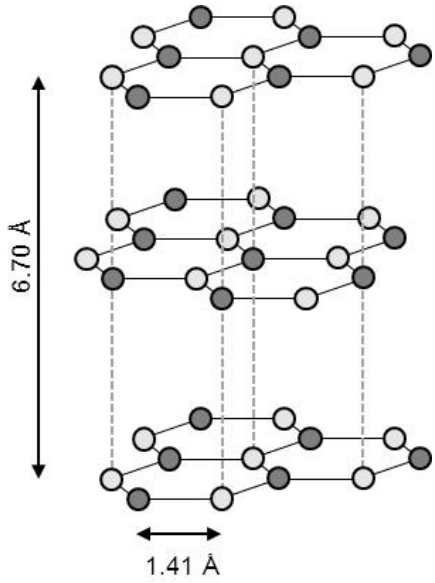

Fig. 2.14 Crystal structure of graphite is shown. Hexagonal layers are formed by sp_2 hybridized orbital of carbon, free electrons are delocalized in a two-dimensional layer. A flat surface is easily obtained by cleave processes, because that only weak van der Waals interaction works between layers.

interaction works between 2D layers, thus HOPG can be easily cleaved by scotch tape. We purchased HOPG from two manufactures. One of sample is SPI-I grade HOPG procured from SPI. Inc. The other one is from Panasonic. HOPG was cleaved in air and load to UHV chamber as soon. To degas intercalation comportment, HOPG are annealed at 673 K for 60 h. We evaluate quality of samples from 2PPE spectra. Work function of clean HOPG is 4.45 eV and contaminated HOPG usually shows lower value of work function. Energy position and peak width of Image Potential states is sensitive to terrace width of HOPG surface. Secondary electron near low-energy cutoff enhanced by roughness of sample surface; scratch or scattering by graphene, which is formed during cleave processes.

2.4.2 Lead phthalocyanine (PbPc)

Phthalocyanine (Pc) which has porphyrin like ring, is a very stable chemical compound. It is able to coordinate many kinds of metal ions in its center cavity). Some kind of Pc is used for pigments because that it absorb of visible and UV lights. Their

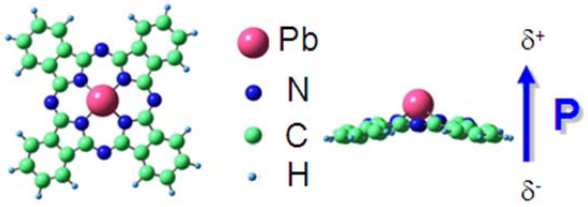

Fig. 2.15: Optimized molecular geometry by DFT calculation (see, ref. [45]) of a PbPc molecule is shown.

optical properties and stability enables wide application for organic devices, oxidation-reduction catalyst, and optical nonlinear materials.

In this thesis we adopt Lead-Pc (PbPc) ultrathin film for sample. PbPc is an organic semiconductor which has small band gap. The color of PbPc is green and they also absorb near infrared lights. Molecular geometry of PbPc is shown in **Fig. 2.15**. In the case of PbPc, The Pc ring is deformed by a large lead atom like a shuttlecock type configuration. Therefore, the molecule has a C4v symmetry and permanent molecular dipole moment directing perpendicular to the Pc ling. The UPS work for PbPc films on HOPG has been performed and discussed with hopping mobility of holes and reorganization energy [8, 45]. One the reason why we adopt the PbPc/HOPG system for our study is that we can obtain well-ordered films in the range of 0 ~ 1 ML. We can estimate the thickness of the films easily by monitoring the work function.

2.4.2 Purification of organic materials

Purification of organic materials is important to assure that deposited organics are reasonably free of impurities. Commercial organic materials are generally in the purity better than 95%, however, further purification is required before loading into the UHV chamber to prevent contaminations of the chamber. Pure grade of organic semiconductors should be comparable to that of inorganic semiconductors (better thanseven nine) for reproducible measurement. There are several techniques for

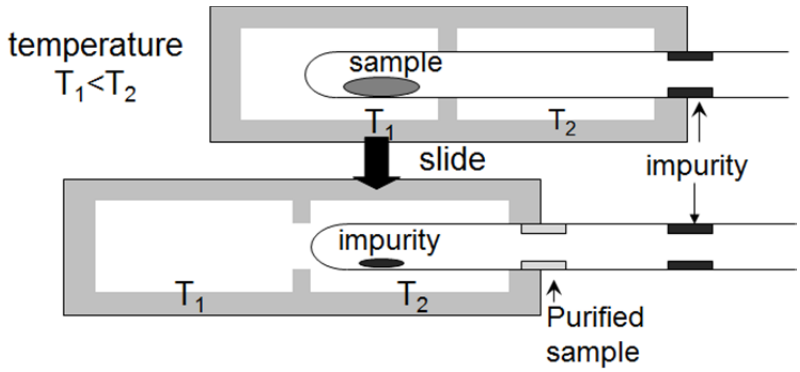

Fig. 2.16: Purification of organics is done by cycles of step-sublimation. Pure sample and impurities has different sublimate temperature, they are geometrically separated by sliding pair of furnaces.

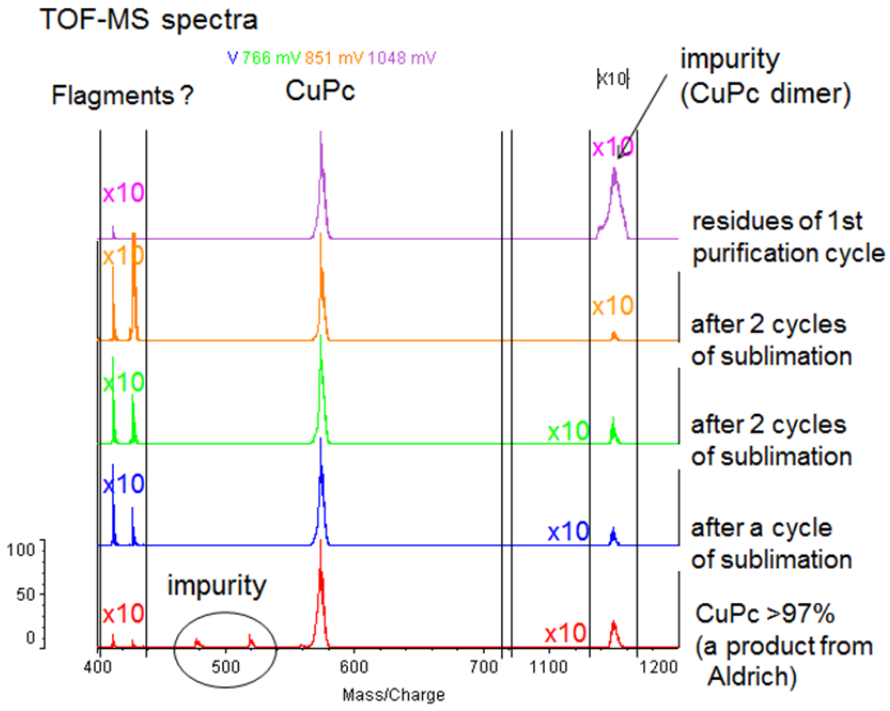

Fig. 2.17: Pure grade of sublimated Copper phthalocyanine (CuPc) is evaluated by MALDI (Laser Desorption Ionization) mass spectra. A product from Aldrich (97% purity) is purified 3 times of sublimation cycles at 673 K. A peak at 574 is derived from pure CuPc. A peak derived from impurity (at 1150, derived from CuPc dimer) is gradually decreased by repeated sublimation cycles. Origins of two peaks around 410 are unknown; maybe they derived from fragments of CuPc (metal-free phthalocyanine).

purification. High purification for powdered organic materials is achieved by Gradient sublimation. **Fig. 2.16** shows a home-made gradient sublimation system. The system is composed of vacuum pumps, an electronic furnace and long quartz tube. The quartz

tube is inserted into the furnace and is evacuated to the pressure of 10^{-5} Pa by a turbo molecular pump. A Pyrex tube, half-cut and joined again, is placed inside the tube. Typically 1 g of powdered source materials is loaded into the end of the Pyrex tube. The temperature of the furnace is gradually increased until the sublimation point of the material is reached. Purified organic crystals grow on inside wall of the Pyrex tube. Impurities, which have lower sublimation temperature, deposit different position in the tube. Impurities, which have higher sublimation temperature, are left at the hottest end of the glass tube. One heating process takes half days. Organic sources are purified 3 cycles in the pre-purification system before loading into the UHV chamber. Quantitative evaluation of pure grade is difficult for organic materials in the order of the seven nine. Only qualitative analysis is available. MALDI (Mass-spectra), IR-spectra in solution and chemical composition analysis are applied to confirm absence of impurities. **Fig. 2.17** shows MALDI spectra during the sublimation processes. Before pre-purification cycle, signals from impurities are observed in MALDI spectra, but these signals are disappeared after one cycle of purification.

2.4.3 Film preparation; deposition and annealing

Deposition of organic films in the UHV chamber assures impurity free films. To reduce defects and to get well-ordered film, deposition rate should be controlled. **Fig. 2.18** shows a schematic illustration of preparation chamber. Deposition of PbPc molecule is done in preparation chamber, to avoid contamination of main chamber. In this work, PbPc was carefully evaporated to substrate at rate of 0.02~0.05 nm / min. PbPc in a quartz tube was heated by applied current to tungsten coils around the tube. The flex of PbPc molecule is monitored quarts micro valance, same distance to sample from source material. After constant flux is obtained, the deposition rate is calculated.

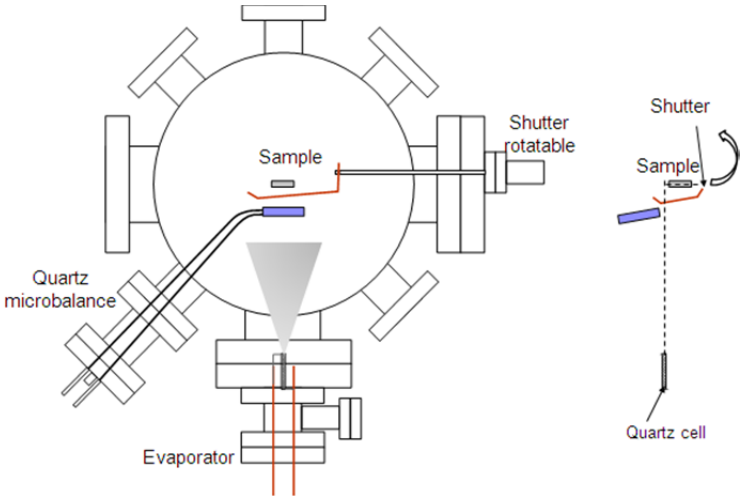

Fig. 2.18: The configuration of the preparation chamber. The PbPc in the Quartz cell is heated by applied electricity. The thickness of the PbPc film is monitored by quartz microbalance. Thickness is tuned by changing time of the shutter opening.

By opening a shutter for several seconds, sample is uncovered and PbPc is deposited on it. As-deposit film is usually inhomogeneous; a typical example will be shown in **section 4.1**. Metastable structure is observed by PEEM measurement. PbPc molecules tend to form dimers; therefore, we couldn't form well-ordered 1 ML film by heating multilayers and desorb excess molecules. To obtain well-ordered films, deposit 1 ML equivalent and then annealing is essential. We keep the sample at 370K for 1 h for annealing process.

3. Electronic structure of well-ordered lead phthalocyanine films studied by combined use of Micro-spot UPS and Micro-spot 2PPE

In this chapter, summary of our former study is described [17, 20]. These results are essential for discussions in following chapters. The first section presents knowledge to discuss unoccupied states on the interfaces; the electronic structure of graphite substrate, nature of Image Potential States. Second section summarizes film growth of PbPc on HOPG and occupied electronic structures on the film. In the last section, unoccupied electronic structures observed in the well-ordered monolayer film described. Occupied and unoccupied electronic states of PbPc films of 1 ML thickness formed on HOPG have been measured by Micro-spot 2PPE. Highly-reproducible and well-resolved Micro-spot 2PPE spectra were obtained by selecting sample positions with sub-micrometer light spot. The molecule-derived states is identified originated from HOMO-1, HOMO, LUMO, LUMO+1, LUMO+2 as well as the first image-potential state (IPS). The occupied states are in good agreement with Micro-spot UPS results. Resonant excitations between HOMO and LUMO+2-related levels as well as that between the HOMO level and IPS were observed in consistency with energies of relevant levels determined from off-resonant conditions.

3.1 Electronic structure of graphite substrate and Image Potential States

3.1.1 Electronic structure of HOPG

Fig. 3.1 shows 2PPE spectrum for HOPG substrate measured at room temperature. Incident light was p-polarized. The photon energy was 4.43 eV. The horizontal axes show energy positions of ejected photoelectron and temporally occupied unoccupied

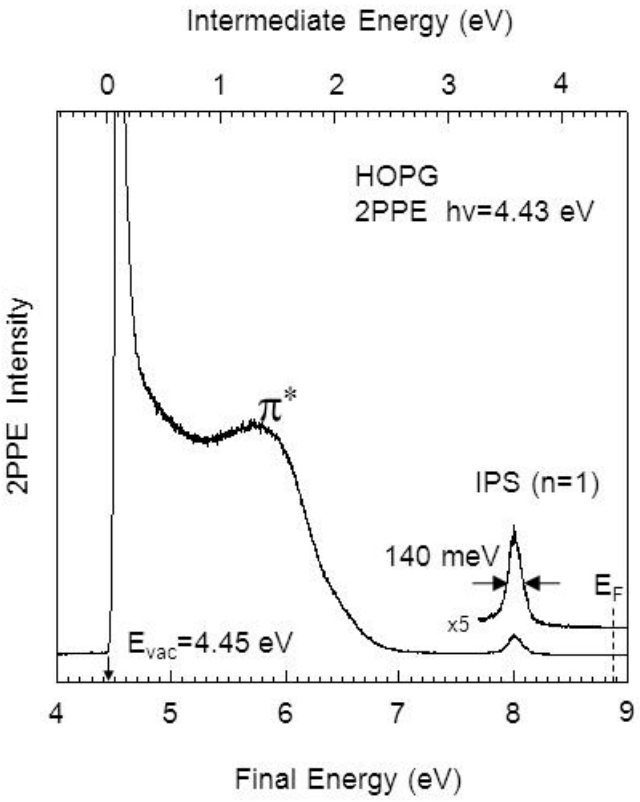

Fig. 3.1: A typical 2PPE spectrum of clean HOPG substrate, measured at room temperature. Incident light was p-polarized and photon energy of it was 4.43 eV. The lower and upper horizontal axes show final and intermediate energy, respectively. Work function was 4.45 eV, determined by lower energy cut-off of the spectrum. A broad structure at 1.7 eV is π*-band of graphite. A sharp peak at 3.58 eV shows IPS (n=1) at surface.

states from E_F; the lower axis shows final energy (for ejected photoelectron) and the upper axis shows intermediate energy (for temporally occupied unoccupied states; final energy - 1$h\nu$). Work function of 4.45 eV for the clean HOPG was determined by lower energy cut-off of the spectrum in final energy scaling. In the 2PPE spectra, two unoccupied structure is observed. They assigned to unoccupied structure by checking peak positions of 2PPE spectra, with varying incident photon energy. A broad structure is observed at around 1.7 eV of intermediate energy. The peak is assigned to the unoccupied π*-band of graphite [48]; reported in the inverse photoemission spectroscopy [49-51]. The peak at 3.58 eV is Image Potential State (IPS, n = 1), agreed

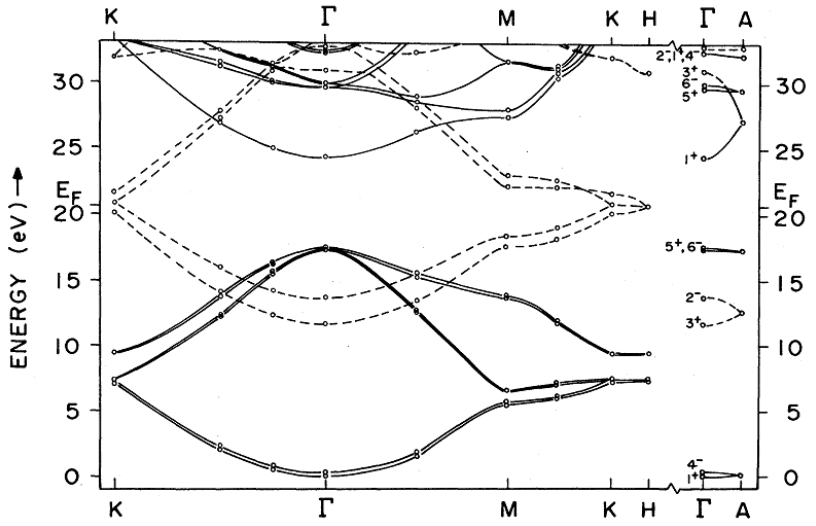

Fig. 3.2: Self-consistent band structure of graphite (Hedin-Lundqvist exchange-correlation potential) from ref. [52]. Dashed lines denote π bands, solid lines denote σ bands.

Table 3-1: Band energies (in eV) for graphite from ref. [52].

	Present results				
	Hedin-Lundqvist	Slater	Previous calculations		Experimental
Γ-point states					
bottom σ band[a]	0	0	0[b]	0[c]	0[d]
	0.3	0.2	0.5[b]	0.3[c]	
bottom π band	11.7	12.9	12.5[b]	11.3[c]	12.5[d]
	13.7	14.5	14.2[b]	13.0[c]	13.4[d], 16.8[e]
top σ band	17.4	17.2	16.1[b]	15.2[c]	16.0[d]
	17.5	17.4		15.2[c]	
unoccupied σ bands	24.5	26.9	28.3[b]	26.6[c]	
	29.8	30.1	28.0[b]	26.8[c]	27.5[f]
	30.1	30.4	28.7[b]	26.8[c]	
E_F	20.8	21.5	20.5[b]	19.5[c]	20.6[d], 22.5[e]
π bands near E_F[g]					
$E_2^0 - E_3^0$	0.7	0.5	0.44[h]	0.44[c]	0.72[i]
$E_3^0 - E_1^0$	0.8	0.6	0.55[h]	0.61[c]	0.84[i]

[a]Lowest σ band chosen as zero of energy; all energies in eV.
[b]Reference 12.
[c]Reference 13.
[d]Angle-resolved photoemission, Ref. 2.
[e]Angle-integrated photoemission, Ref. 10.
[f]Reference 8.
[g]Notation of Slonczewski and Weiss, Ref. 23.
[h]Reference 11.
[i]Reference 9.

with former studies. Electronic properties of IPS are explained in the next session.

Peak positions and intensity ratio between π* band and IPS fluctuates by many factors; roughness of surface, amount of intercalation compounds, cleanness of the

surface, *etc*. Thus, it is required to check those peaks carefully to obtain clean and flat substrate. In the idealized condition, work function is 4.45 eV and width of n = 1 IPS peak is less than 140 meV [17]. Amount of contaminates can be reduced by annealing the sample at 600 K, around 60 h. It is interesting that we can observe the π* structure in 2PPE spectra.

Band structure of graphite is calculated by many researchers [52-55]. However, there are discussions about the position of σ* bands. Holzwarth *et al.* calculate a σ* minimum at 3.7 eV above E_F, below the vacuum level [52]. In contrast, Willis et al. and Tatar et al. suggests that the bottom of σ* is 7.5 eV above E_F [53, 55]. One of the calculated results is shown in **Fig. 3.2** and **Table 3-1**[52]. We collect photoelectrons emitted toward surface normal in the spectrum of **Fig. 3.1**. Thus we probed the $\bar{\Gamma}$-point of the surface Brillouin zone. At the $\bar{\Gamma}$-point, there is no accessible unoccupied bands between from 0 to 4 eV. However, we observed the peak structure around 1.7 eV. The π*-band at 1.7 eV exists around M, K to H points [55, 56]. Intensity of the π*-band in the 2PPE spectra decreases at low temperatures and the result suggests inelastic scattering of electrons by electron-phonon interactions [18, 57]. Other group suggests that π-π* band gap of 4.4 eV in equilibrium is renormalized to 3.9 eV after excitation by UV-pulse laser and they proposed interactions between π-π* excitations and IPS is observed in 2PPE [58].

3.1.2 Image Potential State

This part describes image potential states (IPS) which formed on the substrate. To discuss band structures of IPS on **chapter 6**, summary of the IPS model is described in the section. Following statements are brief extract of chemisorption model taken from ref. [78] To obtain more detail information, see the ref. [59]. Charges in front of a

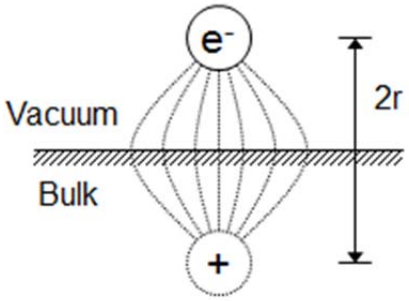

Fig. 3.3: The inducement of an "image charge" in a surface opposite to a test charge distance from surface, *r*.

surface are attracted by a force which can be described by charges of opposite sign positioned behind surface at the same distance of the charge (see **Fig. 3.3**). These forces form a potential described as

$$V = -\frac{e^2}{4\pi\varepsilon_0 \cdot 4r} \qquad (3.1)$$

where r is the distance from the solid. If electrons have energy below E_{vac} and if they are reflected at the metal surface because of the energy is forbidden in the bulk, electrons trapped in the potential well between image potential and the crystal potential. The image potential resembles to radial part of the hydrogen problem, therefore, the solution of IPS are expected Rydberg like series. Binding energies of IPS take discrete values is explained by a modified Rydberg formula, like as

$$E_n = E_{vac} - \frac{Ry}{16(n+a)^2} = E_{vac} - \frac{0.85}{(n+a)^2} \text{ eV} \qquad (3.2)$$

n is the quantum number, a is called for quantum defect independent of n. The explanation of quantum defect theory is described later part of the section. In **Fig. 3.4**, schematic image of IPS is shown.

Binding energies of IPS and lifetimes of their electrons on metal surface are well studied [59, 60]. As shown in **Table 3-2**, the binding energies of the n = 1 states on clean metal surfaces lie in the range 0.5 to 0.8 eV. Binding energies of IPS on Cu(111), Ni(111) and Ag(111) are close to 0.85 eV. The binding energies of IPS on Ag(100), Pd(111) and Cu(100) are close to 0.55 eV. From these results, the binding energies seem

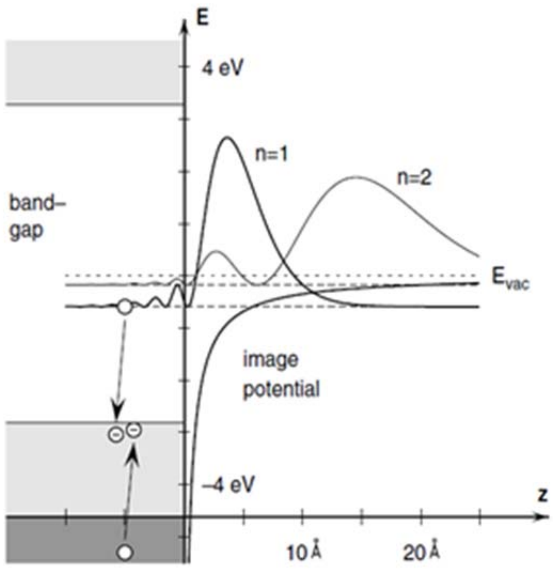

Fig. 3.4: Image potential in front of a metal surface, from ref. [60]. The band gap forbids the penetration into the metal and bound states can be formed. For the lowest two IPS the square of the wave function is shown.

Table 3-2: Measured work function and binding energies of IPS for various surfaces from ref. [59].

		Φ	$E_b(1)$	$E_b(2)$	$E_b(3)$	m^*	Ref.
Ag(100)	expt.	4.43	0.533	0.162	0.075	1.15	25, 32
	calc.	4.435	0.529	0.169	0.080	1.0	
Ag(111)	expt.	4.56	0.77	0.23	0.10	1.3	28, 32
	calc.	4.54	0.75	0.21	0.09	1.3	
Cu(100)	expt.	4.63	0.57	0.18	—	0.9	32, 59
	calc.	4.62	0.52	0.17	0.08	1.0	
Cu(111)	expt.	4.93	0.83	0.25	—	1.0	29, 16
	calc.	4.89	0.83	0.21	0.09	1.1	
Pd(111)	expt.	5.44	0.55	0.15	—	1.0	31
	calc.	5.46	0.58	0.18	0.08	0.9	
Ni(100)	expt.	5.09	0.61	0.18	—	0.95	27, 56
	calc.	5.09	0.50	0.16	0.08	0.9	
Ni(111)	expt.	5.25	0.80	0.25	0.10	1.12	30
	calc.	5.22	0.64	0.19	0.09	1.0	
Co(0001)	expt.	5.20	0.73	0.18	—	—	36
	calc.	5.22	0.64	0.19	0.09		
Fe(110)	expt.	5.12	0.73	0.18	0.05	—	36
	calc.	5.15	0.57	0.18	0.08		

not related to band structures and chemical properties of materials.

Quantum defect theory is concerned with properties of an electron in the field of a positive ion and, in particular, with expressing those properties in terms of analytical functions of the energy [61]. It provides a unified theory of bound states, including

series perturbations, autoionisation, and electron-ion elastic and inelastic scattering. One of example is the energy level of alkali metal atom [62]. The energies of electrons of hydrogen atoms depends only on its principal quantum numbers *n*, thus, the 3s, 3p, 3d configurations has same energy. However, these orbitals do *not degenerate* in any atom with more than one electron. The s-electrons penetrated inside the ion core. Thus the screening of the nuclear charge by the other electrons in the atom is less effective for *n*s configurations than *n*d, and s-electrons have lower energy than d-electrons with the same principal quantum number. For the atom, we consider effective principle quantum number $n^* = n - a$, a is quantum defect. The d-electron has a very small quantum defect since the influence of the ion core is small. On the other hand, s-electron affected serious influence. From analysis of the energy levels of sodium shows quantum defects is below formula and there is a small variation with n.

$$\delta_s = 1.35, \qquad \delta_p = 0.86, \qquad \delta_d = 0.01, \qquad \delta_l \sim 0.00 \text{ for } l > 2 \qquad (3.3)$$

Now, we back on the quantum defect theory on surfaces. Charges in IPS are confirmed between surface potential and image potential. There are no ion cores in the region. Now we consider multi-reflection and phase much at surfaces. When electrons move toward outside, they reflected by image potential and return with phase shift ϕ_b. On the surface they also reflected with phase shift ϕ_c.by bulk potential because of their energies correspond to bulk band gap. If $\phi_b + \phi_c$ correspond to 2π, stationary state is obtained. For the case of an image potential state at middle of band gap above phase-shift explanation is correct. The binding energy is hydrogen-like (0.85 eV) and quantum defect $a \sim 0$. If image state is located near or above band gap, the situation is changed. We must consider the solution of Schrödinger equation at the boundary condition. Wave function and their derivation *must be* match at the surface. Thus, as

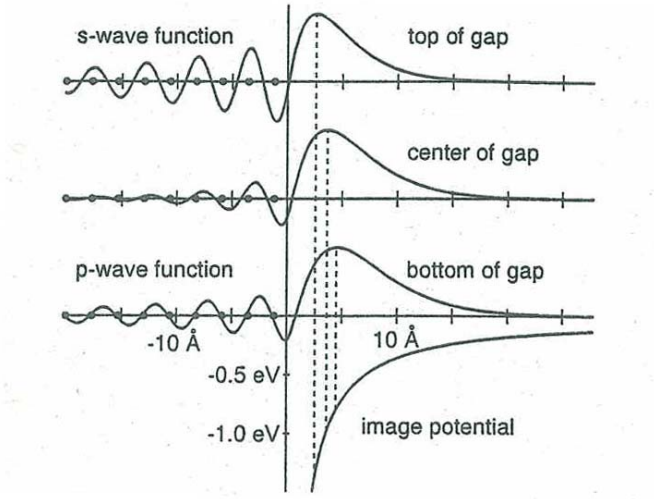

Fig. 3.5: Wave functions for IPS at energies near top, center bottom of the band gap, from ref. [59]. The bulk solution changes from s-(top) to p-like (bottom) and influences the boundary conditions at the surfaces. The shift of the maximum of the wave function away from the surface leads to a reduced binding energy.

Fig. 3.5, phase shift at the surface ϕ_c is varied. The main parameter determining the binding energy of image states is the phase shift ϕ_c of the bulk wave function at the surface which changes from 0 to π when going from the bottom to the top of the band gap. If ϕ_c does not change considerably with the energy range of the image potential state series, the following relation to be quantum defect derived as:

$$a = (1 - \phi_c / \pi) / 2 \qquad (3.4)$$

During above discussion, we consider the image potential is same as that of hydrogen. But there is not good approximation. The potential must be connected smoothly at the interfaces. Ref. [63] is suggests more proper potentials at the surfaces and their calculations shows good agreement with experimental results. In cases of dielectric / metal surfaces we need to consider image charge in dielectric layers. For detailed discussion, see ref. [64].

3.2 Film growth of lead phthalocyanine from Micro-UPS study

Previous works of our laboratory demonstrated the capability of our micro-spot photoemission spectroscopy (Micro-UPS), which achieved the lateral resolution of 300

nm and the energy resolution of 30 meV. The high-energy resolution spectroscopy resolved molecules in different environments [65-67].

PbPc film formed on HOPG substrate system has been studied by UPS in detail [9]. PbPc molecule has a shuttlecock-like chemical structure and an electric dipole moment perpendicular to the molecular plane owing to the C_{4v} symmetry [45, 68]. The well-ordered film of PbPc can be obtained by annealing. PbPc molecules in the first layer are oriented flat with the lead atom directed to the vacuum side, causing decrease of Φ. In the second layer, the molecules are oriented in the reverse direction, canceling the electric dipoles. Thus the Φ increases close to that of HOPG. The HOMO band of the bilayer splits into two peaks due to formation of PbPc dimer [45]. The drastic changes of electronic structure and Φ are advantageous to clarify the correlation between PEEM contrast and the electronic structure measured by Micro-UPS.

3.2.1 Experimental

Experimental setup of Micro-spot UPS is described briefly. Micro-spot UPS is done at the Micro-2PPE chamber, which explained in **section 2.2**. For Micro-spot UPS measurement, the light source is changed from that of Micro-spot 2PPE. The VUV light source was amplified regenerator (Coherent, RegA) operated at a repetition rate of 250 kHz. The output (~ 800 mW) is focused on a BBO crystal and SHG is generated. SHG light is focused to Xe container, which placed between lens and the incident port of the UHV chamber. The 6th harmonics (8.86 eV) is formed by nonlinear optical effect. To avoid absorption of air, the container is evacuated by a rotatory pump, and Xe gas is contained (~ 150 Torr). SHG and IR light is cut by a band-pass filter, which is placed in the container. Ti: Sa laser operated at a repetition rate of 250 kHz. The VUV light was focused onto a sample surface with a Schwarzschild objective of 0.29 numerical

apertures. The spot size of the light was 0.3 μm. The incident angle of the light was 55 degree from the surface normal. Photoelectrons emitted to the surface normal were detected with a hemispherical energy analyzer.

3.2.2 Micro-UPS for PbPc films

Fig. 3.6 shows Micro-spot UPS results for PbPc films as a function of the thickness measured by the microbalance. All spectra were measured after annealing at 373 K for 1h. In **Fig. 3.6**, spectra in the energy region of HOMO band (left panel) are put on the initial energy, and spectra in the region of E_{vac} (right panel) are put on the final energy of electron with respect to the Fermi level (E_F). Φ's were determined from the cutoffs at the E_{vac} in **Fig. 3.6**. The work function changes (ΔΦ) relative to the clean HOPG substrate is shown in **Fig. 3.7**. As the thickness increased from 0 nm [trace (a) in **Fig. 3.6**] to 0.3 nm (d), Φ gradually decreased from 4.45 to 4.27 eV (ΔΦ = 0.18 eV), and the HOMO band appeared as a sharp peak at 1.35 eV for (d). At further deposition, Φ increased up to 4.46 eV (ΔΦ = 0.01 eV) for 0.7 nm thickness (e), and the HOMO band split to two peaks at 1.16 eV and 1.49 eV. These variations of E_{vac} and the HOMO band structures are consistent with Ref. [45]. According to the variations of Φ and the HOMO band peak in Ref. [45], It is defined that thickness of 0.3 nm (d) corresponds to 1 ML, and 0.7 nm (e), to 2 ML. The Micro-UPS results for as-deposited films of < 0.3 nm-thickness were similar to **Fig. 3.6b–d** except for slight broadening of the HOMO features. The HOMO peak position and Φ of the as-deposited films were close to those of the annealed films slightly thinner than the nominal thicknesses. The broad HOMO feature suggests that ordering of molecules is imperfect [17, 67].

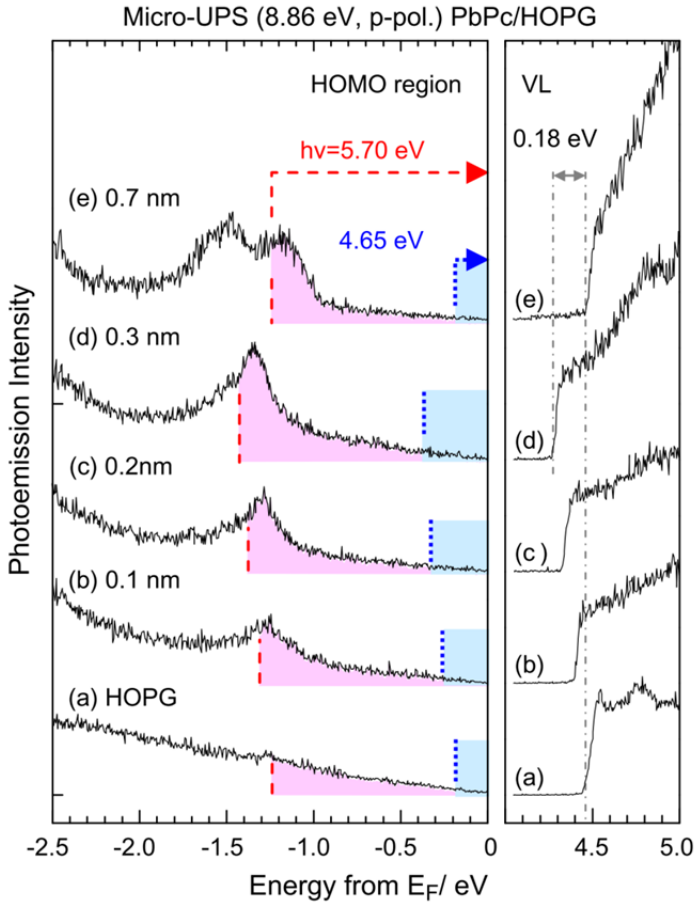

Fig. 3.6: The Micro-UPS results measured with p-polarized light at a photon energy of 8.86 eV for different thickness of PbPc, (a) clean HOPG substrate, (b) 0.1 nm, (c) 0.2 nm, (d) 0.3 nm, (e) 0.7 nm film. All PbPc films in the spectra were measured after annealing at 373 K for 1 h. The left panel with the initial energy scale shows the spectra in HOMO region. The right panel with the final energy scale shows spectra in VL region. In PEEM measurements with the photon energies of 5.70 eV and 4.65 eV, photoemission occurs from the energy regions labeled by red and blue colors, respectively

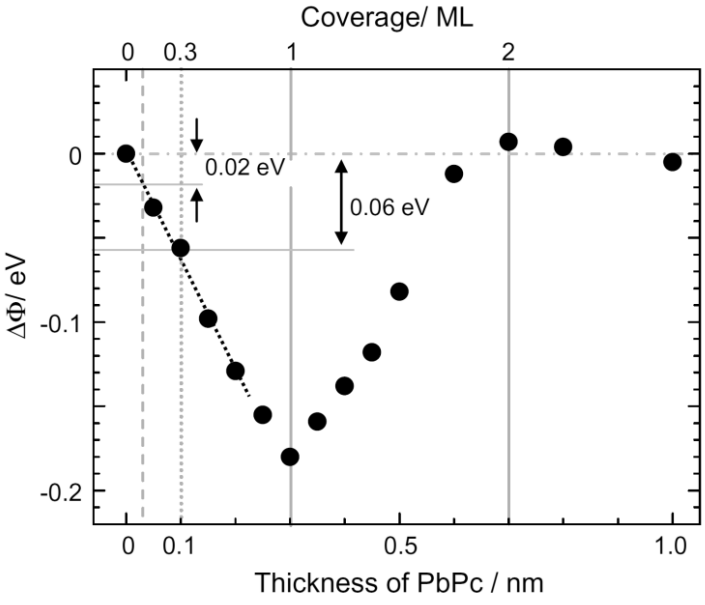

Fig. 3.7: The work function change (ΔΦ) relative to the clean HOPG substrate as a function of the thickness. The ΔΦ were determined from the cutoffs of the VL region spectra in **Fig. 3.6**. The thicknesses of 0.3 and 0.7 nm correspond to the coverage of 1 ML and 2 ML, respectively. The coverage scale in the top is meaningful between 0 and 1 ML and at 2 ML where uniform films were formed. The values of ΔΦ for 0.3 and 0.1 ML films, indicated by dotted and dashed vertical lines, are estimated to be 0.06 and 0.02 eV, respectively.

3.3 Resonant two-photon photoemission study on electronically excited states at an interface of lead phthalocyanine (PbPc)/graphite

In the section, 2PPE spectroscopy for 1 ML of PbPc films grown on a HOPG is shown. Special attention was devoted to the resonant excitations. When photon energy is equal to the energy difference between the occupied and unoccupied states, photoemission is enhanced by resonant excitation [69-71]. The resonance allows identification of both the initial and the intermediate states.

3.3.1 Coverage Dependence

2PPE results measured with p-polarized light at photon energy of 4.33 eV are shown in **Fig. 3.8** for PbPc films of different coverage. By adsorption of PbPc, four peaks (H0, H-1, L0, L1) appeared in addition to a peak, labeled by IPS, which was seen for the bare HOPG, the 0.3 ML and the 1 ML films. The horizontal axis is the final energy of photoelectron with respect to E_F. The spectra were measured at a uniform surface area shown in **Fig. 3.9**. **Fig. 3.9** shows the surface image of an as-deposited film of 0.3 ML coverage. The image was measured by fixing the energy analyzer to the peak H0 in **Fig. 3.8** while scanning the sample across the light focus. Intensity of the peak H0 varied depending on the domains. Regions of bare HOPG have not been found. In addition to the large domains of different brightness, we identified several features due to defects and step bunches of the substrate (see, ref. [21]). The detailed images of PbPc/HOPG surfaces are discussed in ref. [21] on photoelectron emission microscopy (PEEM). We selected typical spectra which showed sharp features and were observed at majority of the surface areas. The selection of the sampling point was effective to improve the reproducibility of the 2PPE spectroscopy.

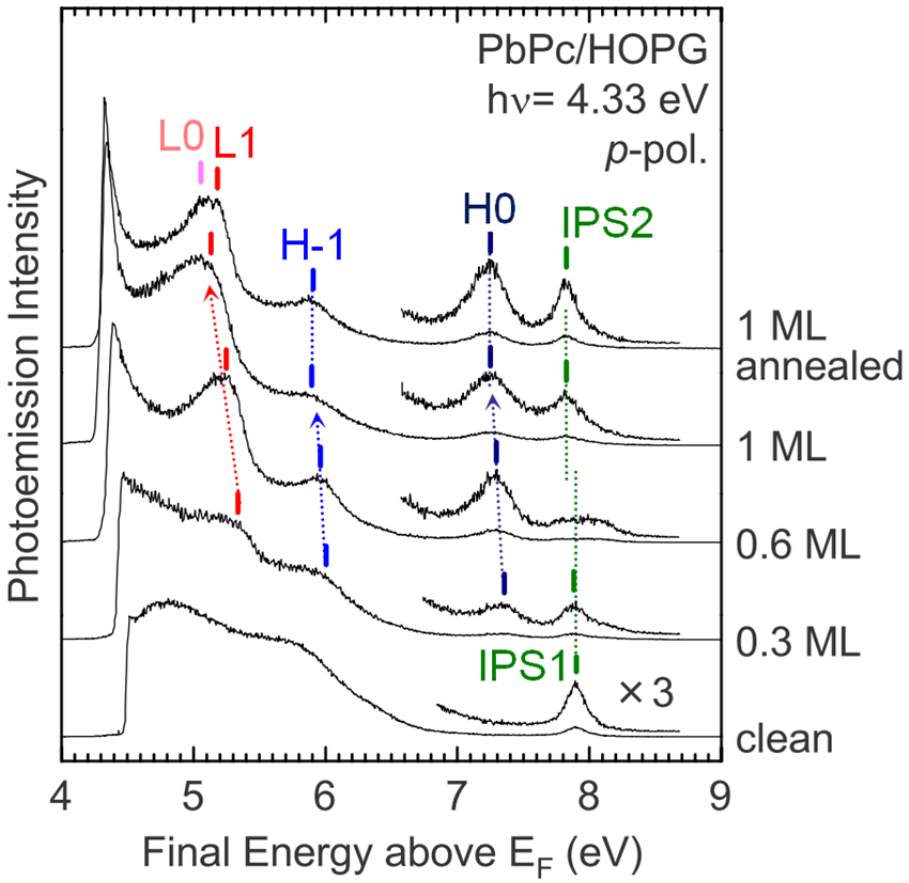

Fig. 3.8: 2PPE results measured with p-polarized light at photon energy of 4.33 eV for different coverage. 2PPE spectrum for an annealed 1 ML film is also shown at the top. The horizontal axis is the final energy of photoelectron with respect to E_F. All spectra were measured at room temperature. The molecule-derived peaks H0, H-1 and L1 shift to lower final energy with increasing coverage. By annealing the film, the L1 peak split into L0 and L1, and the other peaks became sharper while the work function unchanged. The shift of IPS (0.07 eV) is smaller than that of the vacuum level (0.19 eV).

In **Fig. 3.8**, the work function (Φ) determined from the low energy cutoff smoothly decreased from 4.47 eV for the clean surface to 4.28 eV for the nominal thickness of 0.3 nm. Φ became higher at further deposition up to about 0.7 nm nominal thickness where a double layer film is formed. According to the shift of Φ in Ref. [45], we assume 1 ML film was formed at the deposition amount of 0.3 nm. By annealing the 1 ML film at

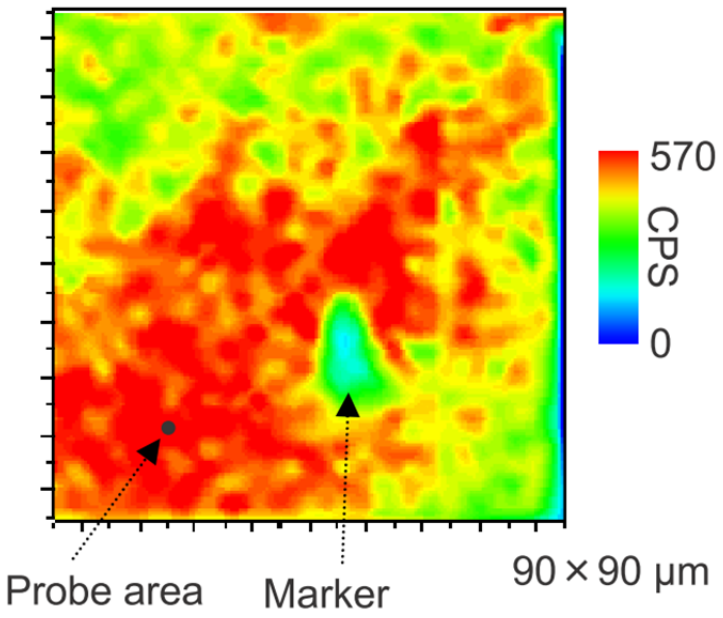

Fig. 3.9: 90×90 μm surface image of PbPc/HOPG (0.3 ML film without annealing) based on the photoemission intensity at the H0 peak in **Fig. 3.8**. The right-hand-scale shows the photoelectron counting rate. We selected sample position in large domains. Maker near the center was made with an intense laser irradiation.

about 373 K for 1 h, the spectra became slightly sharper and the L1 peak split into two components L0 and L1. The value of Φ was not changed. This suggests that the annealing of the as-deposited 1 ML film improved the ordering of the molecules. Actually, sampling position dependence became moderate after annealing.

In the spectrum of the bare HOPG (**Fig. 3.8**, bottom trace), the peak at 7.91 eV is due to the first image-potential state (n = 1, IPS). The IPS feature nearly reproduced those of Refs. [48] and [50] with higher resolution. The IPS peak became weak at 0.3 ML, largely broadened at 0.6 ML, and became sharp again at 1 ML. The peak position forthe 0.3 ML film is close to that for the bare HOPG. The IPS peak for the 1 ML film shifted by -0.07 eV from that for the bare HOPG. The shift is apparently different from the vacuum level shift of -0.19 eV. We consider the broadening as a confinement of the image-state electrons in spaces among adsorbed molecules as discussed in **chapter 4**. At

coverage higher than 0.6 ML the IPS orbital should be located on the molecular film causing the shift of the peak position. The sharp feature of the IPS peak for the 1 ML film support again that PbPc molecules formed an ordered film.

The molecular-induced features, H0, H-1 and L0, L1, L2, shifted to lower final energies with increasing coverage. The clear features for ≤ 1 ML films are characteristic of this adsorption system, in contrast to molecular films on metal surfaces

3.3.2 Photon energy dependence for 1 ML films

In order to assign the molecular-induced peaks, the 2PPE spectra with p-polarized light of different photon energies were measured for annealed 1 ML films as shown in **Fig. 3.10**. The energies of these peaks (marked by bars in **Fig. 3.10**) are plotted as a function of photon energy in **Fig. 3.10**. The data sets for **Fig. 3.11** accumulate the results of several experimental runs for 1 ML films before and after annealing. The data sets also include experiments with HOPG substrates from different origins. All the peak positions align well on the lines of slope 1 or 2 in **Fig. 3.11**: the peaks on the slope 1 lines are due to 1Δhν process arising from unoccupied states, and those on the slope 2 lines are due to 2Δhν process arising from occupied states. The line fitting allows us clear identification of the origins of the peaks. Further inspections of the spectral features are made on the expanded spectra put on the initial energy, defined as (final energy)-2hν, as shown in **Fig. 3.12**. The spectra were the same as those in **Fig. 3.10**. The peaks H0 and H-1 align vertically in **Fig. 3.12**, indicating that the peaks arose from fixed initial states at -1.33 eV and -2.76 eV, respectively. On the other hand, peak positions due to unoccupied states such as IPS shift on this energy scale. The assignments for the occupied states are further confirmed by comparison with a micro-spot 1PPE result at the top in **Fig. 3.12**. The peak positions for H0 and H-1

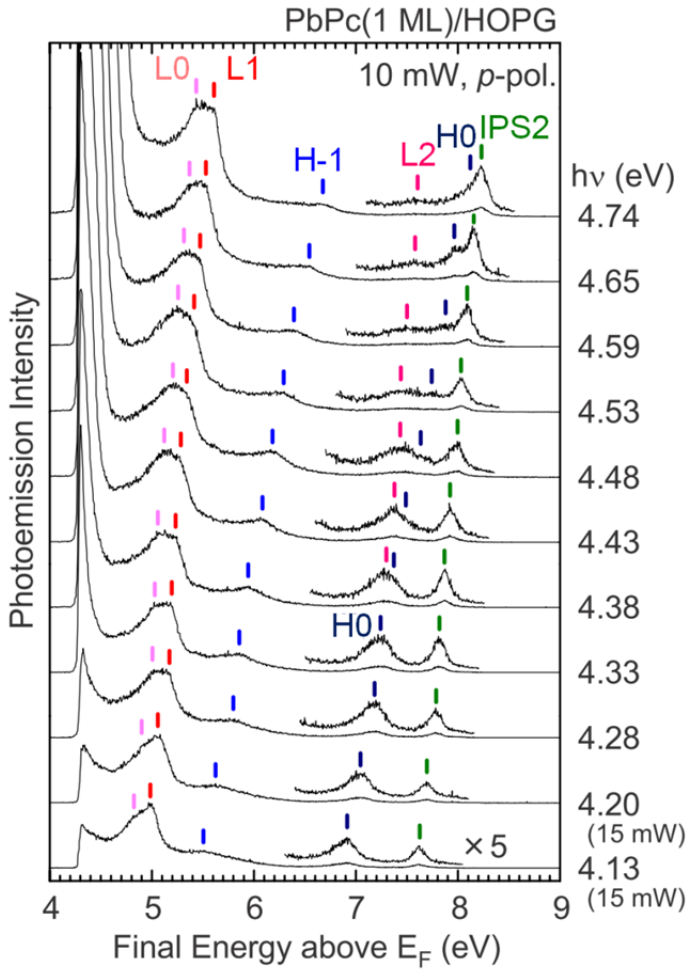

Fig. 3.10: 2PPE spectra for a PbPc film (annealed, 1 ML) on HOPG measured with p-polarized light. The photon energies are shown at the right-hand side. The spectra for hν > 4.38 eV were measured with nearly constant laser power of 10 mW. The spectra for photon energies of 4.20 eV and 4.13 eV were measured with the laser power of 15 mW. No normalization was made on the spectra. The spectra at high final energy region were magnified by 5 times. The energies of each peak are marked by bars. At photon energy higher than 4.3 eV, the peak H0 split into two components, L2 and H0.

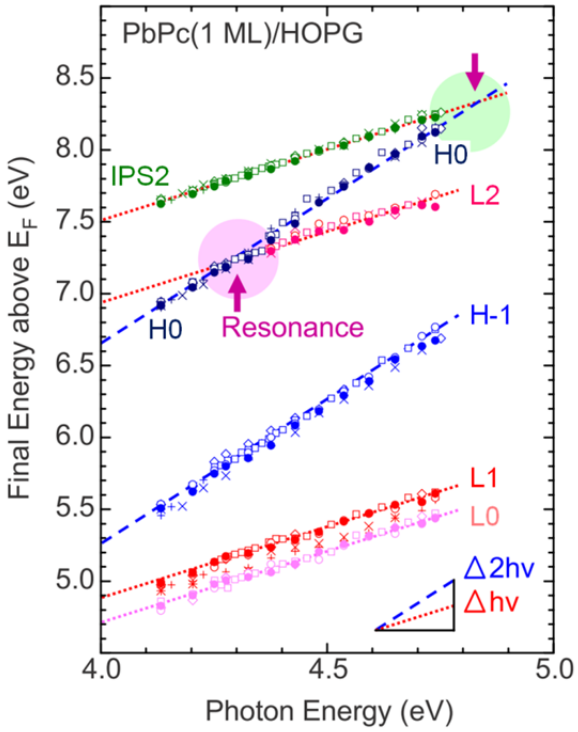

Fig. 3.11: Final energies of the peaks for PbPc (1 ML)/HOPG are plotted as a function of photon energy. The closed circles correspond to the peak energies in Fig. 3. Experimental points for different 1 ML films before (+, ×,*) and after annealing (circle, square, diamond) are shown with different symbols. The slopes of dotted and dashed lines are 1 and 2, respectively. The resonances were observed at photon energies of 4.3 and 4.8 eV.

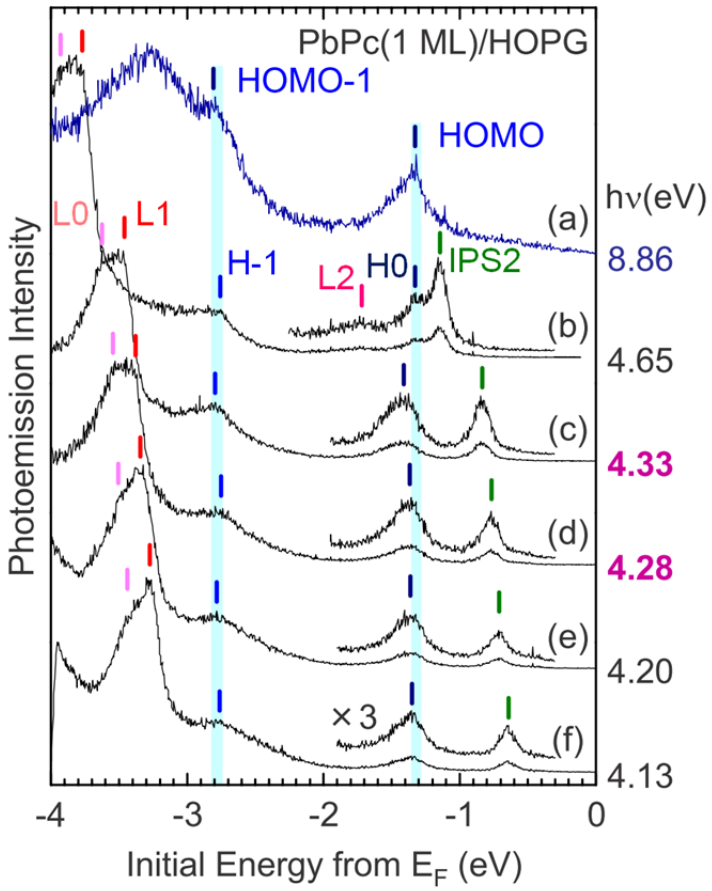

Fig. 3.12: Comparison between UPS (a) and 2PPE (b-e) spectra of PbPc (annealed, 1 ML). The horizontal axis is the initial energy with respect to E_F. Traces at the high initial energy region are magnified by 3 times. The peaks due to occupied states align vertically, while the peaks due to unoccupied states shift with photon energy. The peaks H0 and H-1 in 2PPE spectra (b-e) coincide with the UPS peaks due to the HOMO and HOMO-1 bands.

probed by 2PPE are in good agreement with the UPS result. Initial energies of the peaks H0 and H-1 are also in good agreement with the UPS results for the HOMO and the next-HOMO (HOMO-1) bands, respectively [45].

The features due to the unoccupied states are clearly seen by putting the same spectra in **Fig. 3.10** on the intermediate energy, defined as (final energy) - hν, as shown in **Fig. 3.13**. The IS peak aligns vertically in **Fig. 3.13**, confirming the peak arose from the unoccupied state at +3.51 eV above E_F. The binding energy of IPS with respect to

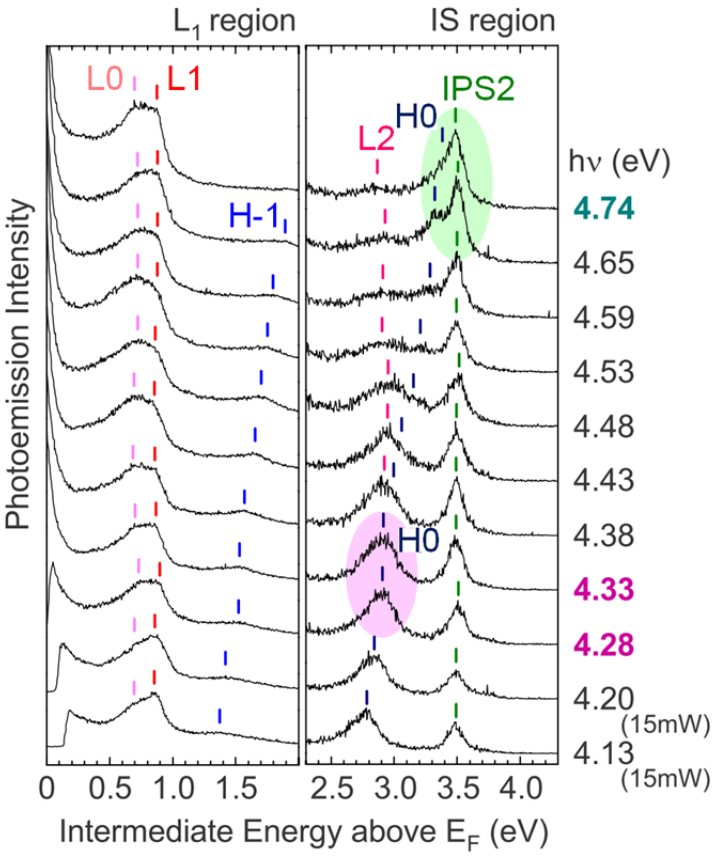

Fig. 3.13: 2PPE results of PbPc (annealed, 1 ML) are plotted on the horizontal axis of the intermediate energy with respect to E_F. The traces of the right panel are expanded by about 10 times to those of the left panel. The peak positions of unoccupied states align on the vertical lines, while those of occupied states moves by one of the photon energy increment. Photoemission is enhanced at photon energy of about 4.3 eV by the resonant between levels for the H0 and L2 features. The H0 peak is enhanced again when it comes closer to the IPS peak, reflecting the resonance between the levels of the H0 and IPS features at the photon energy of about 4.8 eV.

the vacuum level was 0.77 eV, slightly smaller than that for the clean HOPG, 0.89 eV. Similarly, the peaks L0 and L1 arose from unoccupied states at +0.71 and +0.87 eV above E_F, respectively. At photon energies lower than 4.3 eV, the occupied state feature H0 shifted on this axis. At photon energies higher than 4.3 eV, the peak split into two components, H0 and L2. The component L2 aligns vertically in **Fig. 3.13**: the component is due to an unoccupied state at +2.94 eV above E_F. The component H0 lies on the line of slope 2 in **Fig. 3.11** throughout the present photon energy region. Thus the

photon energy of 4.3 eV is resonant with the transition between the occupied state at -1.33 eV (H0) and the unoccupied state at +2.94 eV (L2). Intensities of both components became weaker as the photon energy was increased above the resonance: the intensity variation is in accordance with the trend of resonance in 2PPE [69-71]. On the other hand, the component H0 became clear and intense again at photon energies higher than 4.6 eV where the peak H0 approached the peak IPS. Enhancement of the H0 feature near the IPS peak is due to the resonance between the occupied state of H0 andthe unoccupied IPS. The energy difference between the states for H0 and L2, 1.33+2.94 = 4.27 eV, determined from the line fits of **Fig. 3.11** is in good agreement with the resonance photon energy of 4.3 eV. The energy difference between the states for H0 and IPS, 1.33+3.51 = 4.84 eV, is close to the photon energy of 4.74 eV, at which H0 and IPS features are enhanced by the resonance.

3.3.3 Assignment of observed levels

Fig. 3.14 compares the observed energy levels with results of density functional theory (DFT) calculation. DFT calculations of a free PbPc molecule were performed with B3LYP method and LANL2DZ basis set. The results of the calculation were similar to those of Refs. [45] and [72].

The occupied states for H0 and H-1 were assigned to HOMO and HOMO-1 with reference to the UPS results [45, 68, 73]. The DFT calculation suggests that the unoccupied states for L0 and L1 are related with the twofold degenerate LUMO and LUMO+1, and that for L2, with the LUMO+2. The resonance at 4.8 eV corresponds to the excitation of electron in the HOMO to the free-electron like orbital of IPS. The resonance energy of 4.3 eV corresponds to the optical excitation between the levels due to the HOMO and the LUMO+2. The optical transition between the HOMO and the

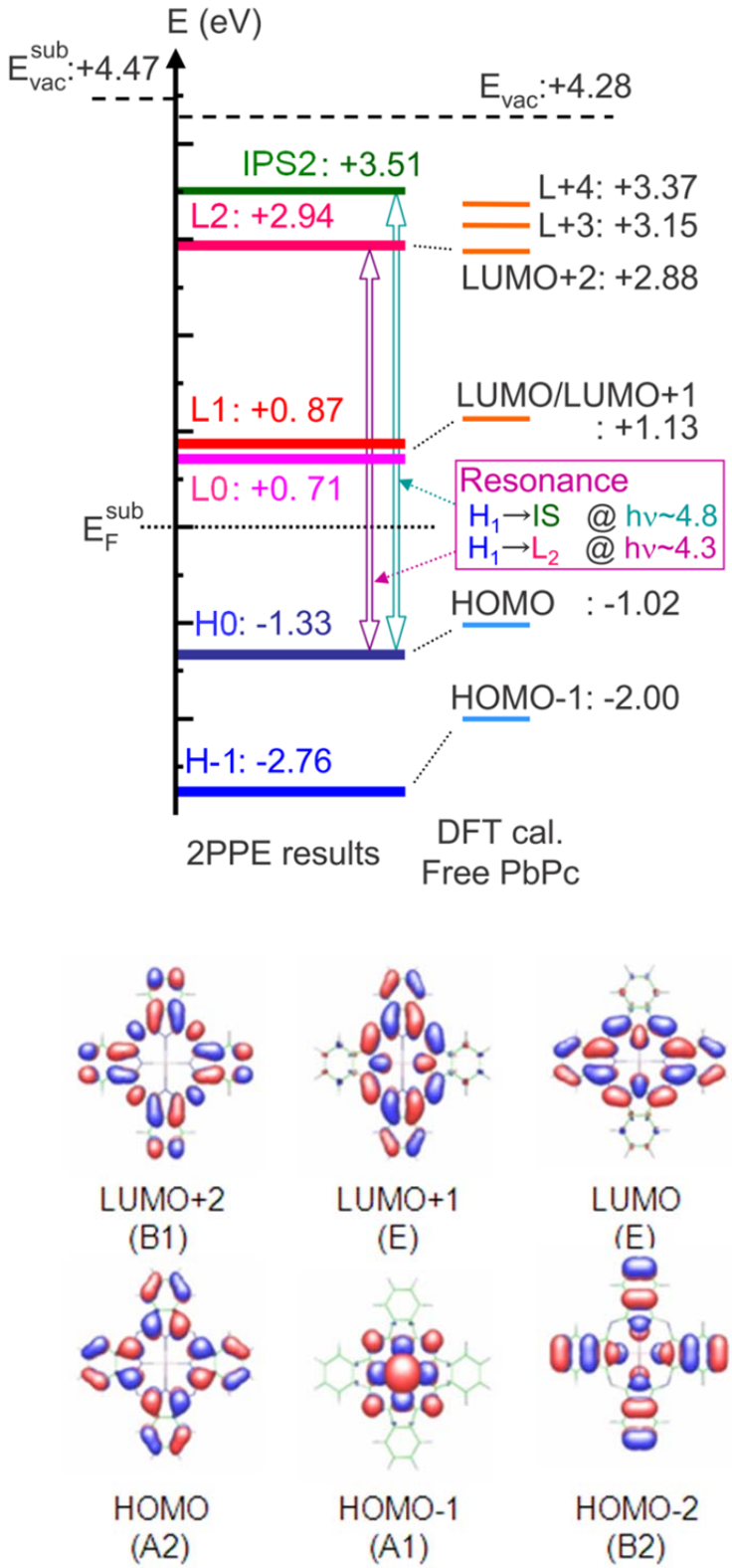

Fig. 3.14: (Top) The energy levels of PbPc (annealed, 1 ML) and the calculated molecular orbital energies from HOMO-1 to LUMO+4 (L+4) of free PbPc. The molecular orbital energies are aligned with the experimental vacuum level. LUMO and LUMO+1 are degenerated in a free PbPc molecule. The block-arrows show the observed resonances from the H0 level to the L2 and to IPS. (bottom) The molecular orbital of PbPc from HOMO-2 to LUMO+2 calculated by DFT with B3LYP method and LANL2DZ basis set. Except for HOMO-1, the molecular orbitals mainly composed with π orbital of phthalocyanine ring.

LUMO+2 is forbidden in free molecules. Along with the split feature of L0 and L1, which are degenerate in free molecule, the observed resonance indicates that the electronic states of the adsorbed molecules are fairy perturbed by interactions with the surface. Here, we keep the limited meaning in mind to compare the experimentally determined unoccupied levels with the calculated orbitals in which there are no electrons.

Initial energies for H0 and H-1 observed in 2PPE reproduced those in UPS. The agreement is reasonable for the off-resonant 2PPE case, because the final states are the same one-hole state irrespective of the number of photons involved in photoemission. On the other hand, we must consider the effect of the real intermediate state at the resonant 2PPE condition. In **Fig. 3.12**, the H1 peak at photon energy of 4.33 eV shifts by about 0.1 eV to lower initial energy. The shift was found to be reproducible for repeated experiments. At the resonant condition, an electron in the HOMO level is excited to the LUMO+2-related level. The resulting electron-hole pair may cause some relaxation processes within the pulse duration of the laser pulse, 100 fs. The shift of the H0 peak at the resonance should be a result of the relaxation. It is interesting to note that when the electron is excited, it is not necessarily localized on a molecule, but may be delocalized. The delocalization of electrons in low lying normally unoccupied levels has been assumed in X-ray emission spectroscopy of adsorbed molecules on metal surfaces [74]. Free electron like character of the LUMO band and formation of the singlet exciton after few ps from a pump laser pulse was reported for a multilayer film of C60 [75]. The interaction of the delocalized electron with the hole in the HOMO level should be negligibly weak. On the other hand, when an electron-hole pair is localized within a molecule (molecular exciton), the charge correlation energy may be about 0.5 ~

1.5 eV as estimated from the stabilization energy of excitons in organic films [76]. The exciton formation from delocalized excited electron should be an event occurring at time region after 100 fs from the pump pulse, and should cause rather large change of the 2PPE spectrum, fairly significant than the observed shift of the peak H0. Time-resolved experiment is in progress to confirm the delocalization/localization of excited electron. Comparison of resonances to L2 and to IS is interesting, because the real intermediate state formed by the resonance to IS involves an excited electron in the delocalized, free-electron like orbital.

The resonance from the HOMO level confirms that the LUMO+2-related level was not populated by photon-induced electron transfer from the substrate to the molecule. The electron transfers from the substrate produces negatively charged states which should be compared with IPES results. Unfortunately, no IPES work has been reported for PbPc/HOPG. No resonance was identified for the LUMO- and LUMO+1-related levels L0 and L1. Photo excitation to the L0 and L1 levels from the occupied levels lower than HOMO-2 is possible within the present photon energy region. However, the broadly overlapped occupied levels below HOMO-2 [45, 68] may smear out the resonance feature. Photon energy dependence of the intensity ratio between the L0 and L1 peaks suggests that the levels were also populated by photo excitation from the occupied levels. The L0 peak became more intense relative to the L1 peak as the photon energy was increased as shown in **Fig. 3.10** and **Fig. 3.13**. The enhancement of the lower energy level for the L0 feature with higher excitation energy is not very probable by transfer of hot electron in the bulk.

The energy difference between the HOMO level and the LUMO-related level observed by 2PPE was 2.04 eV. The value is different from the optical gap determined

from optical absorption of PbPc in solutions, 1.76~1.84 eV [74], and from EELS of thick films, 1.6~1.8 eV [77]. Comparison of the present results with the optical band gaps is left without discussion before the localization/delocalization of excited electron becomes clear from the time-resolved experiments.

3.4 Supplemental material: adsorption on surface and shift and broadening of electronic structures

In the **section 3.2** and **3.3**, we have discussed electronic structures of an organic / inorganic interface. In this section, summary of theory of electronic structures of molecule absorbed surface is described. During discussions in **section 3.2** and **3.3**, we regard occupied / unoccupied electronic structures like as molecular orbitals of PbPc. But observed electronic structures are broad and stabilized than that of free molecules. Therefore, the observed energy levels in PbPc film are hybridized to bulk structures of HOPG. In following chapters, we discuss obtained results with this weak-chemisorption model. The theories of surface are summarized in ref. [78]. Following statements are brief extract of chemisorption model, taken from ref. [78].

3.4.1 Newns-Anderson Model

The modification of the electronic structures upon absorption in term of the adsorbate-substrate coupling can derive using a semi-quantitative, Newns-Anderson model [78]. To establish qualitative trends and basic mechanisms, it is often useful to describe a complex system by a simplified Hamiltonian with limited parameters.

Consider a substrate characterized by a quasi-continuum of Bloch states ϕ_k with eigenenergies ε_k and an adatom interacting with the substrate. The adatom shall be described by a single valence state ϕ_a with energy ε_a. The interaction can be described in

its simplest form by the following model Hamiltonian

$$H = \varepsilon_a \widehat{n_a} + \sum_k \varepsilon_k \widehat{n_k} + \sum_k \left(V_{ak} \widehat{b_a^+} \widehat{b_k} + V_{ka} \widehat{b_k^+} \widehat{b_a} \right) \qquad (3.4)$$

with

$$\widehat{n_\iota} = \widehat{b_\iota^+} \widehat{b_\iota}, \quad i = a, k, \qquad (3.5)$$

where $\widehat{n_\iota}$ is the number operator, and $\widehat{b_\iota^+}$ and $\widehat{b_\iota}$ are the creation and annihilation operator of the orbital ϕ_i, respectively. The interaction of the substrate and adatom states is given by the matrix element V_{ak}. Note that equation (3.4) is a single-particle Hamiltonian, thus, the Hamiltonian could in principle be written as a sum over independent one-particle states $H = \sum_i \varepsilon_i \widehat{n_\iota}$. Still, a direct solution of the Schrödinger equation

$$Hc_i = \varepsilon_a c_i \qquad (3.6)$$

by diagonalization is intractable due to the infinite number of substrate states. Nonetheless, the Newns-Anderson Hamiltonian (3.4) can be used to derive some fundamental aspects of the behavior of the adatom valence state ϕ_a upon adsorption. We rewrite the projected density of states as

$$G = \sum_i |\langle \phi_i | \phi_a \rangle|^2 \, \delta(\varepsilon - \varepsilon_i) = -\frac{1}{\pi} Im \sum_i \left(\frac{\langle \phi_i | \phi_a \rangle \langle \phi_i | \phi_a \rangle}{\varepsilon - \varepsilon_i + i\delta} \right) = -\frac{1}{\pi} Im \, G_{aa}(\varepsilon) \qquad (3.7)$$

where G is the single particle Green function.

$$G = \sum_i \frac{|\phi_i><\phi_i|}{\varepsilon - \varepsilon_i + i\delta} \qquad (3.8)$$

where, as usual, δ is assumed to be a small positive number, $\delta = 0^+$, and G is formally defined by

$$(\varepsilon - \varepsilon_i + i\delta) G(\varepsilon) = 1. \qquad (3.9)$$

By writing (3.9) in matrix form and eliminating $G_{ka} = \langle \phi_k | G | \phi_a \rangle$, $G_{aa}(\varepsilon)$ can be written as

$$G_{aa}(\varepsilon) = \frac{1}{\varepsilon - \varepsilon_a + \sum(\varepsilon)} \tag{3.10}$$

where the self-energy $\sum(\varepsilon) = \Lambda(\varepsilon) - i\Delta(\varepsilon)$ is given by

$$\Delta(\varepsilon) = \pi \sum_k |V_{ak}|^2 \ \delta(\varepsilon - \varepsilon_k) \tag{3.11}$$

and

$$\Lambda(\varepsilon) = \frac{1}{\pi} P \int \frac{\Delta(\varepsilon\prime)}{\varepsilon - \varepsilon\prime} d\varepsilon'. \tag{3.12}$$

Here P denotes the principal part integral. Inserting (3.10) into (3.7) yields the projected density of states in terms of $\Lambda(\varepsilon)$ and $\Delta(\varepsilon)$,

$$n_a(\varepsilon) = \frac{1}{\pi} \frac{\Delta(\varepsilon)}{\left(\varepsilon - \varepsilon_a - \Lambda(\varepsilon)\right)^2 + \Delta^2(\varepsilon)}. \tag{3.13}$$

Now we consider a limiting case. Let us donate the substrate band width by *W*. If $V_{ak} \ll W$, then we may just take the average value $V_{av} = \langle V_{ak} \rangle$ and insert it in (3.11)

$$\Delta(\varepsilon) \approx \pi \sum_k |V_{\mathrm{aV}}|^2 \ \delta(\varepsilon - \varepsilon_k) = \pi {V_{\mathrm{aV}}}^2 n_k(\varepsilon) \tag{3.14}$$

where $n_k(\varepsilon)$ is the density of states of the unperturbed substrate. In the wide-band limit, we may assume that $n_k(\varepsilon)$ and consequently also Δ is independent of the energy. Such a situation is typical for the *sp*-band of a simple metal. In this case Λ is zero, and the projected density of state simply corresponds to a Lorentzian of width Δ centerd around ε_a. Physically, this means that the adatom valence level is broadened into a resonance with a finite lifetime $\tau = \Delta^{-1}$. This scenario is called the *weak chemisorption case*. Our PbPc /HOPG results are this case.

3.4.2 Energy shift and broadening of adatom state

The energetic location of the adatom resonance $\varepsilon_a^*(z) = \varepsilon_a(z) + \Lambda(z)$ is variable parameter. The presence of asurface will modify both the ionization energy *I* and the electron affinity *A*. Let us consider a hydrogen atom in front of a perfect conductor, as in

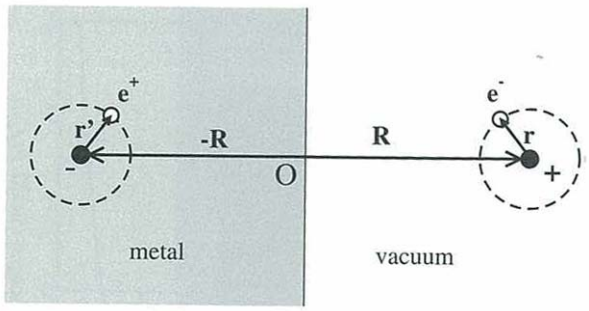

Fig. 3.15: image potential formed by substrate, from ref. [78]

Fig. 3.15.We must consider image potential formed by substrate, because I and A are influenced by image potential (see, **Fig. 3.16**). The attraction of the electron to its own image is overcompensated by the repulsion with respect to the negatively charged image of the ion which stays at –Z. The effective ionization energy in front of a perfect conductor is given by

$$\mathrm{I}_{\mathrm{eff}}(z) = I - \frac{e^2}{4\pi\varepsilon_0}. \qquad (3.15)$$

On the other hand, we want to add an electron to a neutral atom in front of a surface, we gain the additional energy due to the interaction of the electron with its own charge. Therefore, the electron affinity is increased to

$$\mathrm{A}_{\mathrm{eff}}(z) = A + \frac{e^2}{4\pi\varepsilon_0}. \qquad (3.16)$$

Depending on whether the affinity or the ionization level crosses E_{F} when the atom approaches the surface, the adatom will become negatively or positively charged, respectively. However, the adatom may well be neutral, if the Fermi energy remains between the ionization and the affinity levels.

The considerations with respect to the ionization and affinity levels of a hydrogen atom can be extended to occupied and unoccupied atomic levels in general. Thus the energy of unoccupied levels tends to shift down in front of a conductor while occupied

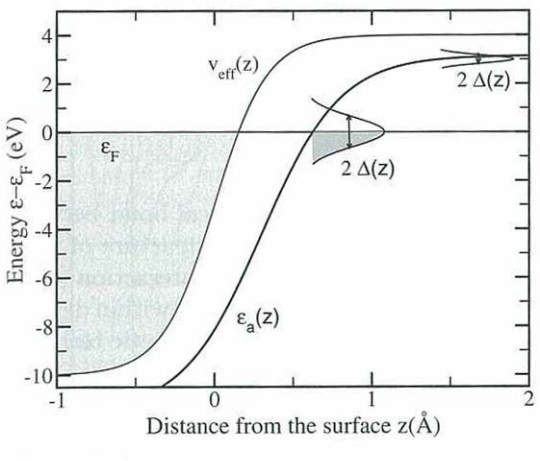

Fig. 3.16: Schematic sketch of the shift of the ionization energy *I* and the electron affinity *A* in front of a perfect conductor caused by the image potential, from ref. [78]. The metal work function is denoted by Φ.

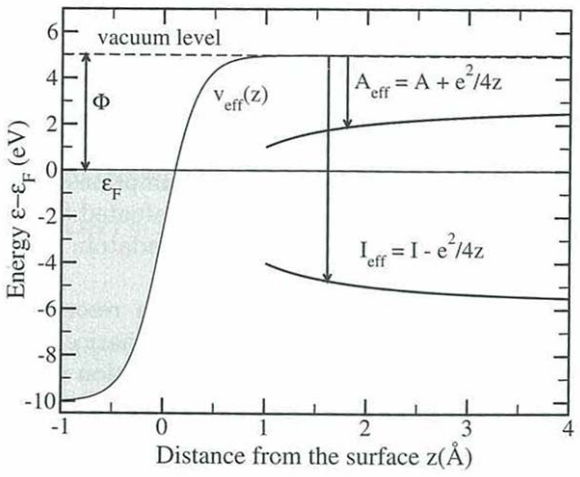

Fig. 3.17: Schematic sketch of the shift and the broadening of an adatom valence level $\varepsilon_a(z)$ upon approaching a surface, from ref. [78]. $V_{eff}(z)$ corresponds to the effective one-electron potential of the bare substrate. The shaded areas illustrates the filled levels

levels are shifted up. This is only true as long as there is negligible overlap with the substrate wave functions. Close to surface, there is the additional modification of the adatom levels due to the interaction with the substrate states. A typical example of the shift and broadening of an affinity level is plotted in **Fig. 3.17**. Close to the surface the

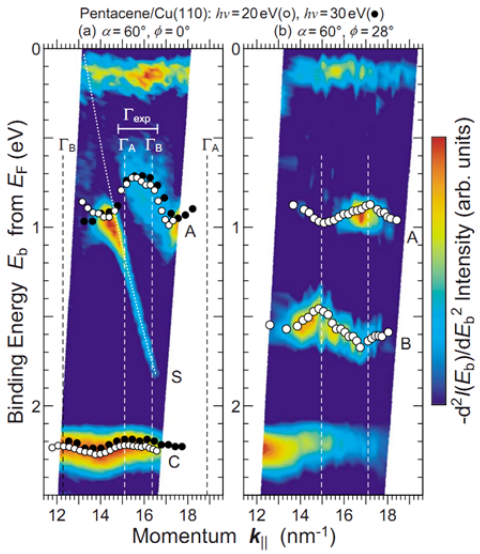

Fig. 3.18: In-plane intermolecular energy-band dispersion in the pentacene monolayer on Cu(110) at ϕ = 0° (the [1 -1 0] substrate direction) and ϕ = 28°, from ref. [80]. The abscissa is the parallel component of the wave vector ($k_{//}$), and the ordinate is the binding energy (E_b) relative to the Fermi level (E_F) of the substrate. In order to map out the energy-band dispersion, we took the second derivative of the ARUPS spectra [$-d^2I(E_b) / dE_b^2$] at $h\nu$ = 20 eV after smoothing to specify the energies of the spectral features. Open and filled circles indicate the position of the pentacene-derived peaks in the raw ARUPS spectra measured at $h\nu$ = 20 and 30 eV, respectively.

pure 1/z dependence of the level becomes modified due to the hybridization with the substrate states.

If molecular orbital and bulk bands strongly hybrid, we observe bonding and anti-bonding states at surfaces. Especially on metal surface, these effect drastically change the electronic structures at the surface [79]. On pentacene / Cu (110) surface, pentacene forms well-ordered lattice structures. HOMO states of pentacene shows dispersion, reflected the film structures, as **Fig. 3.18** [80]. From the result, the observed HOMO level on film is not localized state but surface-mediated intermolecular interaction is evolved, like the Newns-Anderson model described in **section 3.4.1**.

3.5 Chapter summary

Occupied levels (HOMO-1, HOMO) and the unoccupied levels related to LUMO, LUMO+1 and LUMO+2 as well as IPS state of PbPc 1 ML films on HOPG is probed. Energy positions of occupied states obtained by 2PPE are consistent with the results of UPS. Resonant excitations from the HOMO level to the LUMO+2-related level and the HOMO level to IPS are observed, confirming that the unoccupied levels are populated by photo excitation from the occupied level. We could obtain highly-reproducible and well-resolved 2PPE spectra by employing sub-micrometer light spot.

4. Lateral inhomogeneity of unoccupied states for PbPc films

In this chapter, we focus on the relation between unoccupied electronic structures and geometric inhomogeneity of organic films. Owing to complicated substrate- molecule and intermolecular interactions, the growth of organic films is typically inhomogeneous, and the lateral inhomogeneity complicates the electronic structures and carrier transportation. In chapter 3, it has shown that highly-resolved and well- reproducible 2PPE spectroscopy for lead phthalocyanine (PbPc) films became feasible by the micro-2PPE method. All occupied and unoccupied levels near the Fermi level (E_F) was observed in the well-ordered monolayer film. The well analyzed system is very suitable for characterizing the effect of lateral inhomogeneity on the electronic structure. The environment of molecules in sub-ML films is less uniform than in the well-ordered monolayer film. The fluctuation of the environment modulates the interface electronic structure. In particular, unoccupied levels are considered to be more sensitive to the environment than occupied levels. Because of the anti-bonding character, the unoccupied molecular orbital extends outside the molecule, resulting in enhanced interaction with neighboring molecules. The main issue is the environment-induced modulation of occupied and unoccupied levels through micro-2PPE spectroscopy and surface imaging. It is shown how the unoccupied levels of PbPc films are affected by the lateral distribution of molecules. It is found that the unoccupied levels are sensitive to surface morphology at the nm-scale.

4.1 Typical coverage-dependence of 2PPE spectra

The 2PPE spectra for sub-ML films are position-dependent even after the annealing. To demonstrate the typical coverage dependence, the most frequently observed 2PPE

spectra measured at photon energy of 4.33 eV are shown in **Fig. 4.1**. The vacuum level (VL) determined from the low-energy cutoff reproduces the work function change [21, 45]. The first (n = 1) image potential state (IPS) on bare HOPG appears at a final energy of 7.93 eV (IPS1, closed triangle). The binding energy from the vacuum level (E_{vac}) is 0.85 eV [17, 19]. The width of the IPS1 peak is 140 meV. The deposition of PbPc causes the IPS feature to broaden toward the higher final energy side by 0.3 eV, as shown in **Fig. 4.1** by the upside down closed triangle. We note that the broadening of the IPS feature occurs only toward the higher energy side, indicating that it is not due to a homogeneous effect such as lifetime broadening. At coverage values above 0.4 ML, a new component, IPS2, indicated in **Fig. 4.1** by an open triangle, appears at energy slightly below the IPS1 peak. As the coverage increases, the IPS2 component intensifies and shifts to lower final energy. The IPS2 component becomes a sharp peak at 7.85 eV for the 1 ML film. The IPS2 peak for the 1 ML film reproduces the IPS on the well-ordered 1 ML films [17, 19]. The IPS2 peak for the 1 ML film is stronger than the IPS1 peak for bare HOPG [19]. The broadened feature labeled by the upside down closed triangle disappears when the 1ML film is formed.

In addition to the IPS feature, four peaks labeled L0, L1, H-1, and H0 are observed. The peaks were assigned based on the photon energy dependence [17, 19]. The energy of the unoccupied level is given by (final energy) - $h\nu$, where $h\nu$ is the photon energy. The initial energy of the occupied level is given by (final energy) – $2h\nu$. The L0 and L1 peaks are due to the unoccupied levels derived from the lowest unoccupied molecular orbital (LUMO) and the next LUMO (LUMO+1). LUMO and LUMO+1 are degenerate in a free molecule. The degeneracy is lifted upon adsorption and the split levels appear as two peaks [17, 19]. The levels are populated by transitions from the occupied levels

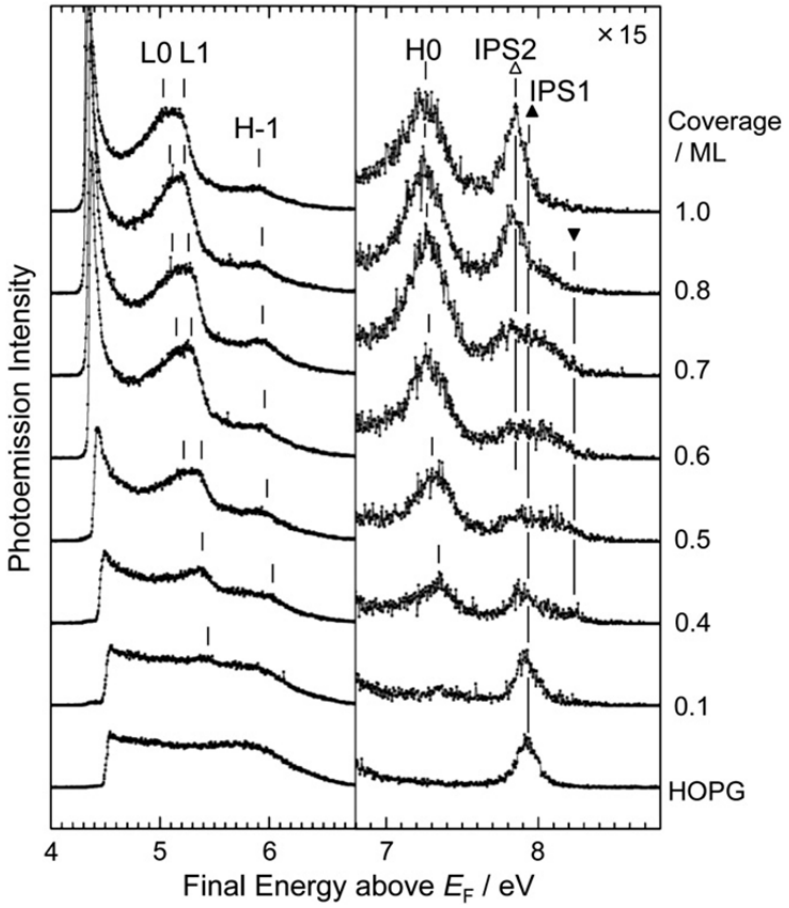

Fig. 4.1: Micro-2PPE results for different coverage of PbPc on HOPG measured with p-polarized light at photon energy of 4.33 eV. Coverage is indicated on the right. The horizontal axis is the final energy of photoelectrons with respect to the Fermi level (E_F). The traces in the right panel are expanded by a factor of 15 relative to those in the left panel. The peaks labeled L0 and L1 are due to split features derived from originally degenerate LUMO and LUMO+1 levels, respectively. The shoulder labeled H-1 arises from the HOMO-1 derived level, and the peak labeled H0, from the HOMO derived level. The IPS feature on the clean HOPG (IPS1) is indicated by a closed triangle and that on the well-ordered 1 ML film (IPS2), by an open triangle. The IPS features on sub-ML films are 0.3 eV wide, as indicated by the upside down closed triangle.

deeper than the next HOMO (HOMO-1) [19]. The peak denoted by H-1 is due to the coherent 2PPE from the HOMO-1 derived level. Optical transition between the HOMO and LUMO+2 levels is forbidden for a free molecule, but adsorption-induced symmetry degradation generates the peak labeled H0 [19]. The energy of the H0 peak is determined by the initial energy of the HOMO derived level: The peak due to the

LUMO+2 derived level appears at higher photon energies [17, 19].

The energies of these molecule-derived peaks shift as the coverage increases. The shifts are summarized in **Fig. 4.2**. These shifts cause no significant change in the resonant conditions between occupied and unoccupied levels. For example, although the H0 feature splits into two peaks when the photon energy exceeds the resonance [19], no such splitting is observed in **Fig. 4.1**. Thus, we can discuss the change in the unoccupied features without considering the pump processes. The H-1 and H0 peaks shift linearly with the coverage at a rate of 0.15 eV/ML. The shift rate is comparable to that of VL (0.18 eV/ML). That is, the ionization energies of the HOMO-1 and HOMO derived levels are almost unchanged by the coverage. The shift is similar to the results of the one-photon photoemission measurement [45]. In contrast to these peaks that are due to occupied levels, peaks L0 and L1 shift at a rate of 0.35 eV/ML. The unoccupied levels are not pinned toVL. The energies of the LUMO and LUMO+1 derived levels relative to VL are stabilized by 0.2 eV when the 1 ML film is formed. This stabilization is presumably due to the intermolecular interaction, that is, the unoccupied levels are stabilized when the molecules are densely packed. The unoccupied levels are more sensitive to the change in neighboring molecules than occupied levels. We note that the coverage-independent ionization energies for HOMO and HOMO-1 are not a general trend for organic molecular films. A coverage-induced shift in ionization energy has been observed for several systems [2]. In the case of CuPc on HOPG, the VL shift was very small (about 60 meV) and the HOMO energy shifted by 0.15 eV as the coverage increased. [15, 66]. Although the mechanism of the energy shift by intermolecular interaction in the surface-parallel direction is unclear, the stabilization of LUMO by 0.2

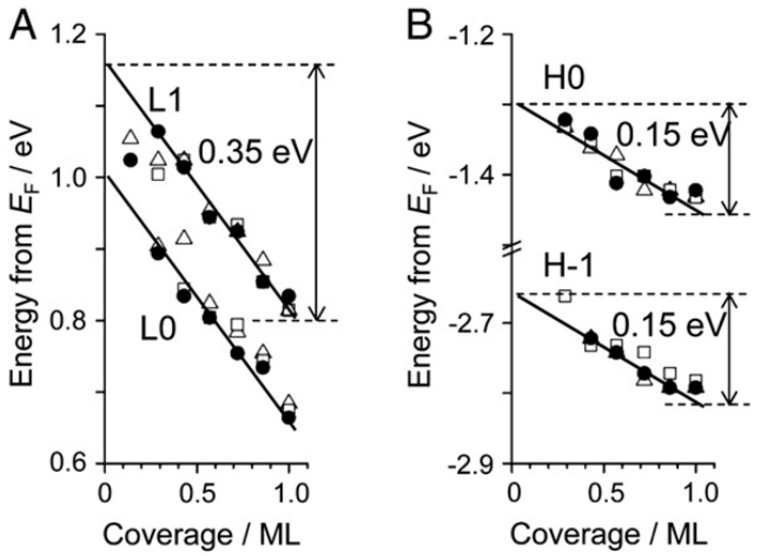

Fig. 4.2: The peak positions in **Fig. 4.1** are plotted as a function of coverage. The different marks show data points for different experimental runs. The energy shifts (0.35 eV) of the L0 and L1 peaks shown in (a) are larger than that for the H-1 and H0 peaks shown in (b). The shifts for the HOMO and HOMO-1 levels are both 0.15 eV/ML which is comparable to the VL shift of 0.18 eV / ML. The shifts for L0 and L1, larger by 0.2 eV than the occupied level shifts, are due to the intermolecular interaction.

eV is not surprising in view of the known trend of occupied levels. We consider a contribution of the substrate-mediated intermolecular interaction. Similar stabilization of LUMO was reported for vanadyl naphthalocyanine (VONc) on HOPG [81].

4.2 Lateral-dependence of the electronic structure

Next, we focus on the lateral distribution of the electronic structure. Photoelectron emission microscope (PEEM) images taken from Ref. [21] are shown in **Fig. 4.3**. The amount of deposition is equivalent to 0.3 ML. **Fig. 4.3A** and **Fig. 4.3B** show images of as-deposited and annealed films, respectively. These images were taken at photon energy of 5.70 eV. At the photon energy, photoemission occurs from the HOMO band of PbPc, and the brightness of the image represents the density of adsorbed molecules [21].

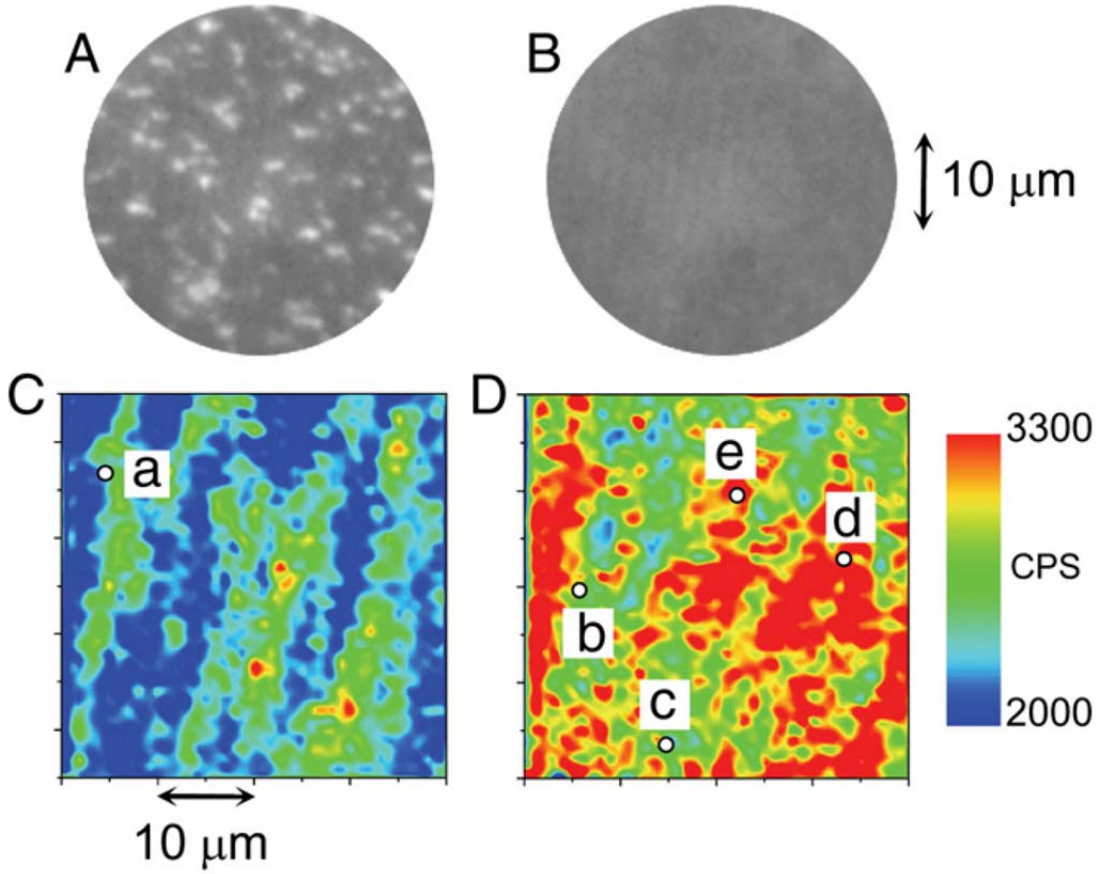

Fig. 4.3: Surface images of the 0.3 ML films. Top images are one-photon PEEM images of as-deposited film (a) and annealed film (b) measured with p-polarized light at photon energies of 5.70 eV. The brightness of the image is proportional to the molecular density. The bright patches in (a) due to the metastable bilayer are quenched by annealing, as shown in (b). The molecular density in (b) seems to be uniform. Bottom images are micro-2PPE images measured at the energy of the L1 peak. The photon energy is 4.33 eV. The lateral inhomogeneity of the as-deposited film (c) is enhanced for the annealed film (d). Comparison of (b) and (d) indicates that the intensity of the L1 peak is governed by a factor other than the number of molecules within the probe spot of 0.4 μm. Micro-2PPE spectra at points A to E are shown in **Fig. 4.4**.

The bright patches in **Fig. 4.3A** are due to islands of the metastable bilayer. The islands disappear upon annealing, as shown in **Fig. 4.3B**. The density of PbPc molecules in the annealed film is uniform within the lateral resolution of our PEEM (50 nm). PEEM images for films of different coverage are shown in Ref. [21]. The PEEM images for the annealed 0.6 and 1.0 ML films seem to be quite uniform.

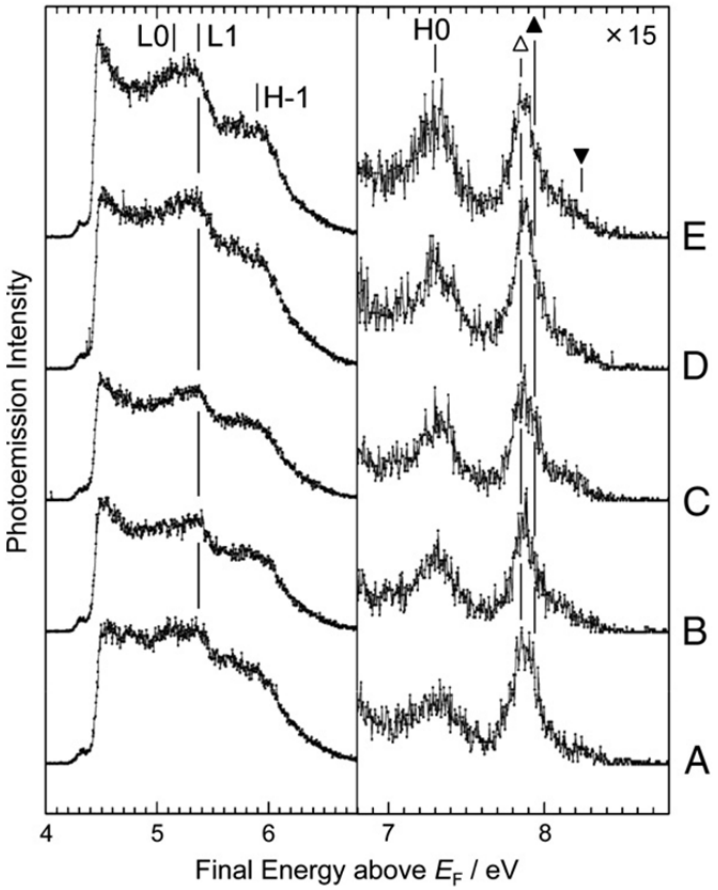

Fig. 4.4: Micro-2PPE spectra taken at points A to E in Fig. 4.3. Point A is on the as-deposited film, and B-E, on the annealed film. The VL cutoff for B to E is at a constant energy, in consistency with the uniform image in Fig. 4.3 (b). The L1 peak is broad at point A. It becomes intense and sharp at B and C, and is further enhanced at D and E. By contrast, the H-1 peak is only weakly dependent on the measured points. The inhomogeneity in Fig. 4.3 (d) corresponds to the intensity variation of the L1 peak. The intensity is governed by the size distribution of PbPc clusters schematically illustrated in **Fig. 4.5**. The energies of IPS1 and IPS2 in Fig. 4.1 are shown by vertical lines labeled by closed and open triangles. The IPS peak energy is higher than IPS2 and lower than IPS1, indicating that molecular clusters larger than 10 nm are not formed in the film.

The images in **Fig. 4.3C** and **D** are measured by the micro-2PPE method, in which the photoemission intensity at the energy of the L1 peak (5.35 eV, the vertical line in **Fig. 4.4**) is recorded while scanning the sample. **Fig. 4.3C** and **D** show images for the as-deposited and annealed films, respectively. The conditions for film preparation are similar to those corresponding to **Fig. 4.3A** and **B**. In sharp contrast to **Fig. 4.3B**, the

image in **Fig. 4.3D** is laterally inhomogeneous even after the annealing. The 2PPE spectra measured at points A to E in **Fig. 4.3** are shown in **Fig. 4.4**. The E_{vac} cutoffs are 4.40 eV for the spectra at points B to E. The uniform E_{vac} for points B to E is very similar to the uniform surface image in **Fig. 4.3B**. The L1 peak for the as-deposited film is broad and weak (spectrum for point A). At points B and C, the L1 peak is sharper than that for point A. The peak intensity is higher at points D and E than at points B and C. The overall increase in the photoemission intensity from **Fig. 4.3C** to **Fig. 4.3D** is the result of sharpening and enhancement of the L1 peak. The red areas in **Fig. 4.3D** correspond to the enhanced L1 peak as at points D and E. Interestingly, the lateral dependence of the H-1 peak is not as significant as that of the L1 peak. A similar position dependence of 2PPE spectra is observed for annealed films of 0.6 ML coverage.

The film in **Fig. 4.3B** appears to be uniform. Thus, the number of molecules within the probe area of the micro-2PPE (400 nm) should be the same for any of the sampling positions in **Fig. 4.3D**. The intensity variation of the L1 peak presumably arises from some inhomogeneity at a scale too small to be detected by the PEEM of 50 nm resolution.

4.3 Broadening of the IPS feature

We start our discussion with the broadening of the IPS feature. It is known that the IPS peak on the Cu(111) surface shows an up-shift and broadening by adsorption of Cu atoms onto the Cu(111) surface [82]. The shift can be understood by a simple particle-in-a-box model: the decrease in the mean terrace length due to the adsorbed Cu atoms causes an up-shift in the IPS energy, and the width of the IPS peak reflects the distribution of the terrace length. The analysis also successfully described the peak

positions and width of the IPS as well as the Shockley state features for polycrystalline copper [16]. A similar quantum confinement is observed for the IPS at Co nano-islands on Au(111) [83] to which a refined particle-in-a-box model was applied.

We analyze the change of the IPS features for PbPc/HOPG with a simple model. As the PbPc coverage increases, the mean length of the free HOPG surface area shortens, which in turn shortens the mean free path of IPS electrons. The decrease in mean free path leads to an up-shift of the IPS. The peak shape is determined by the length distribution of the free HOPG area. We do not assume two-dimensional (2D) confinement, but rather only the mean free path of the IPS electrons. We assume that the IPS electrons are scattered by the adsorbed molecules. The IPS wave function on metal surfaces has maximum amplitude at 0.5 nm outside the surface [63]. The substrate-molecule distance for organic films, typically 0.3 nm [84, 85], is considered to be effective in scattering the IPS electrons. We also assume that PbPc molecules in the low-coverage (0.3 ML) film are distributed randomly on the surface, rather than forming bilayer islands or μm-size crystals. This assumption is supported by the linear decrease in the work function and by the uniform PEEM images (**Fig. 4.3B**). A 2D-gas-like random distribution of molecules has been reported for low-coverage films of tin phthalocyanine (SnPc) on Ag(111) [84] and is also assumed for VONc on HOPG [81]. The repulsive intermolecular interaction by the electric dipole moment perpendicular to the molecular plane may be responsible for the random distribution.

As a rough estimation of the length of the free HOPG area, we employ a 1D particle-in-a-box model, $\varepsilon(L) = h^2/(8m^*L^2)$, where the energy ε of a particle (mass of m*) is determined by the length L of a 1D potential well, and h is the Planck constant. We take the mass of the IPS electron on HOPG to be 1.2 of the free electron mass. The

effective mass, determined from our angle-resolved 2PPE measurement, is in agreement with the value reported in the literature [50]. Details of the angle-resolved experiment will be described in the following chapter. An energy broadening of 0.3 eV leads to an estimation of the minimum length of the free HOPG area of about 1 nm. Though the estimation method used is primitive, this value is comparable to the lattice constant of 1.37 nm for CuPc on HOPG and MoS_2 [86]. A similar structure is known for PbPc on MoS_2 [87]. When the free length is longer than 10 nm, the IPS peak shift is smaller than 3 meV and cannot be detected. That is, the IPS profile is sensitive to the free length only when the length is sufficiently shorter than 10 nm. The broadened IPS feature without a clear peak observed for the 0.6 and 0.7 ML films in **Fig. 4.1** indicates that these films contain free HOPG areas whose mean lengths are randomly distributed in the range from 1 to 10 nm.

The IPS2 peak appears at 0.4 ML and, after a slight shift to lower energies, becomes strong for the > 0.7 ML films. The IPS2 peak is due to the IPS on PbPc film. As the IPS2 peak becomes clear, the broadened IPS feature becomes less significant. This indicates that closely-packed aggregates (2D crystals) of PbPc begin to grow at the coverage. A transition from 2D-gas-like distribution to 2D crystal formation is known for several types of Pc films [84]. Taking the mass of the IPS electron on PbPc film to be less than 2.5 of the free electron mass (our preliminary experimental result), the broad IPS2 peak for the 0.4 ML film suggests that 2D crystals or clusters of PbPc larger than 10 nm are scarcely formed on the surface. Thus, the film appears homogeneous when the surface image is taken with the PEEM of 50 nm resolution. The enhancement and sharpening of the IPS2 peak at >0.7 ML coverage indicate the growth of the cluster size. Clusters larger than 10 nm are formed at 0.8 ML and the PbPc layer is flat and

uniform in the 1 ML film.

4.4 Lateral-inhomogeneity of the L1 peak

The L0/L1 peaks are stabilized by 0.2 eV when a 1 ML film is formed. As the coverage increases, the length of the free HOPG area decreases, and the narrowing of the intermolecular distance leads to the formation of small clusters. The formation of PbPc clusters is evident from the appearance of the IPS2 peak at 0.4 ML. Also evident is the growth of the clusters at high coverage. The down-shift of the L0/L1 peaks is the result of the formation and growth of clusters. The interaction between neighboring molecules stabilizes the L0/L1 peaks. As the cluster size increases, the L1 peak shifts to lower energies and becomes sharper owing to the improved homogeneity of the environment. The shift and sharpening of the L1 peak are nearly parallel to the change in the IPS2 peak. The change in the L1 peak intensity in **Fig. 4.4** reflects the change in size of the molecular clusters. The IPS peak in **Fig. 4.4** is located at a slightly lower energy than IPS1. The IPS on bare HOPG should overlap with the IPS on the molecular clusters. The IPS peak is located at a slightly higher energy than IPS2 on the well-ordered 1 ML film. The up-shifted IPS indicates that the molecular cluster size is a few nm at all measurement points.

Fig. 4.5(a) and **(b)** shows schematic models of molecular distribution on the 0.3 ML surface. The number of black dots (molecules) in **Fig. 4.5(a)** and **(b)** is the same. **Fig. 4.5(a)** is a model for points B and C: there are scarcely any molecular clusters. The molecules are separated by free HOPG areas a few nm in length. The intermolecular interaction is weak and the L1 peak is located at a relatively high energy. Such area appears in **Fig. 4.3D** as green areas. At points D and E, among randomly distributed molecules, nm-clusters (<10 nm) are formed as shown in **Fig. 4.5(b)**. The increased

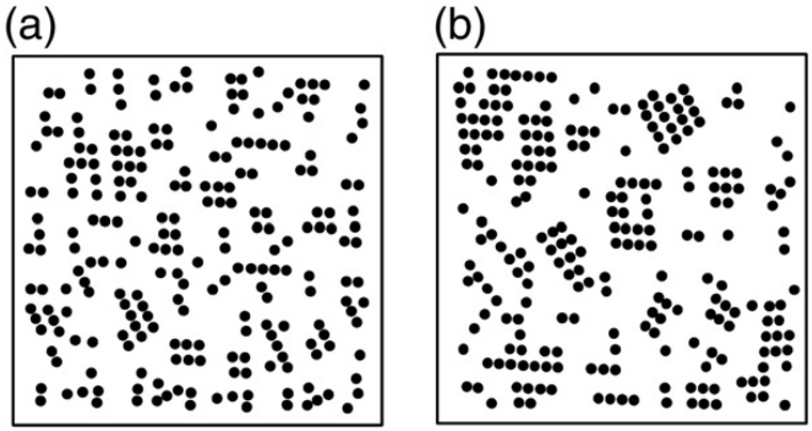

Fig. 4.5: Schematic representations of the size distribution of PbPc clusters. The number of dots (molecules) is the same for (a) and (b). The size of the drawing is approximately 40 nm^2. The area shown by (a), in which clusters are scarcely formed, is the model for points B and C. The model for points D and E is shown in (b). Clusters, smaller than 10 nm, are formed, which improves homogeneity of the molecular environment.

inter-molecular interaction results in an enhanced and stabilized L1 peak. The enhancement of the L1 peak for points D and E relative to that for points B and C is due to the improved homogeneity of the molecular environment. Such areas show up red in **Fig. 4.3D**. The inhomogeneous surface image in **Fig. 4.3D** reflects the size distribution of molecular clusters on the surface. As is mentioned in **Section 4.1**, the origin of the coverage-dependent stabilization of the L0 and L1 peaks is not clear. Similar stabilization for VONc/HOPG was attributed to the excited-state polarizability [81]. We are not certain if the electrostatic potential model is valid for clusters smaller than 10 nm.

Interestingly, the nm-scale structures shown in **Fig. 4.5** are accumulated to form areas several-10 μm in size, as observed in **Fig. 4.3**. Optical microscopy reveals that the surface of the present HOPG contains many corrugations and defects. This inhomogeneity of the substrate is thought to be responsible for the formation of the

large domains.

4.3 Chapter summary

The lateral resolution of micro-2PPE is 400 nm, and we can only observe the average of the electronic structure of molecular clusters. Nevertheless, information on the nm-clusters can be revealed by micro-2PPE spectroscopy. The present results demonstrate that unoccupied levels are very sensitive to the molecular environment. Micro-2PPE spectroscopy is a powerful method for investigating how intermolecular interactions affect unoccupied levels at surfaces. Both of the molecular distributions shown in **Fig. 4.5(a)** and **Fig. 4.5(b)** seem to be very random, though nm-clusters are formed in **Fig. 4.5(b)**. The distributions differ only in the degree of randomness. When observed with scanning tunneling microscopy or atomic force microscopy, the distributions may seem very similar. Possible tip-induced destruction may hinder identification of the difference. As long as the surface image is measured with the occupied level, the annealed sub-ML film is considered to be composed of 2D-gas-like, randomly distributed molecules. But a slight difference in the randomness causes a significant lateral inhomogeneity of unoccupied energy levels. Film uniformity can only be discussed after a detailed consideration of the physical properties of the measurement method.

It is interesting that the nm-clusters shown in **Fig. 4.5** aggregate to form several areas 10 μm in size (see **Fig. 4.3D**). The cause of the large-area formation is unclear at the present stage. In addition to the substrate inhomogeneity, mass dynamics of groups of molecular aggregates [67] may be considerable because the lateral structure is not stable according to day-by-day observation.

5. Dispersions of image potential states on surfaces of clean graphite and on lead phthalocyanine film

In this chapter, we focus on the dispersion of image states on clean HOPG surface and on 1ML PbPc/HOPG surfaces. Image potential is originated from surface electrostatic potential and we regard surfaces as homogeneous slab. Thus, the Image Potential State (IPS) theory, which described in **section 3.1.2**, has wide application. Therefore, with tremendous progress of solid-state physics, natures of image potential states on metal or dielectric solids are extensively studied. As shown in **chapter 4**, in cases of organic/inorganic surfaces, the film structure is usually laterally inhomogeneous and be composed of many grains (size of ~nm). From micro-2PPE result of film of PbPc/HOPG, in well-ordered organic/inorganic interfaces, image potential laterally affect ranges of more than several ten nm. In the 1 ML film, PbPc molecule forms well-ordered lattice structure. The lattice may form periodic potential and may effect on electron which excited to IPS. But lateral resolution of 2PPE is usually in order of 100 μm and obtained result is average of several domains and not clear. But micro-spot 2PPE enables focus laser light source on one domain. So, we can clearly observe how the periodic potential modulates band structure of IPS by Micro-spot 2PPE. To observe the effects, dispersions of image potential states on graphite surface (denoted as IPS1) and on the monolayer (1 ML) film (denoted as IPS2) of lead phthalocyanine (PbPc) are investigated by the micro-spot angle-resolved 2PPE (micro-AR-2PPE). On a graphite surface, whole dispersions of the two members of IPS1 (n = 1 and 2) are observed. The effective mass of electron in the n = 1 IPS1 becomes slightly light at high momentum region. The IPS1 peak is weakly visible at energy higher than the vacuum level. These results suggest the interaction between the

IPS1 and the interlayer band of graphite. HOPG is polycrystalline material and reported dispersion of IPS is not clear. Our result shows an advantage of micro-AR-2PPE which combine with high-energy resolution and high-lateral resolution. On PbPc film, back-folding and band gap formation of IPS2 is observed. 1-dimensional Kronig-Penny model is used to reproduce the effective mass and the shift of binding energy. The results shows micro-AR-2PPE measurement is possible on the case of organic thin films.

5.1 Image potential states on clean HOPG

Fig. 5.1(a) and **(b)** show AR-2PPE results for the image potential states (IPS) on the clean HOPG surface measured at the photon energy of 4.77 eV and 4.33 eV. The horizontal axis at the bottom is the emission angle (θ) from the surface normal. The left-hand side vertical axis shows the kinetic energy of photoelectron with respect to the vacuum level (VL) and, the right-hand side, the binding energy referred to VL. **Fig. 5.1(a)** and **(b)** are drawn by putting together the AR results measured by rotating the sample normal direction from the energy analyzer by angles of -5°, 0°, 10°, 20° and 30°. The borders of each image are indicated by gray solid lines. The energy and intensity of each AR result connect smoothly with each other at the borders. The AR results for **Fig. 5.1(a)** and **(b)** are fitted with the parabolic dispersion curves (see below). There are no differences of the fitting results for **Fig. 5.1(a)** and **(b)**, irrespective of the difference of the electron kinetic energies. These results show that our AR measurement is free from experimental artifacts such as electric field between the sample and the analyzer.

The highest energy of photoelectron in 2PPE is $E_F + 2h\nu$ where E_F is the Fermi energy and $h\nu$, the photon energy. The broken horizontal lines show the energy. In **Fig. 5.1(b)**, intensity of the $n = 1$ IPS peak (IPS1) is really vanishing above the broken line.

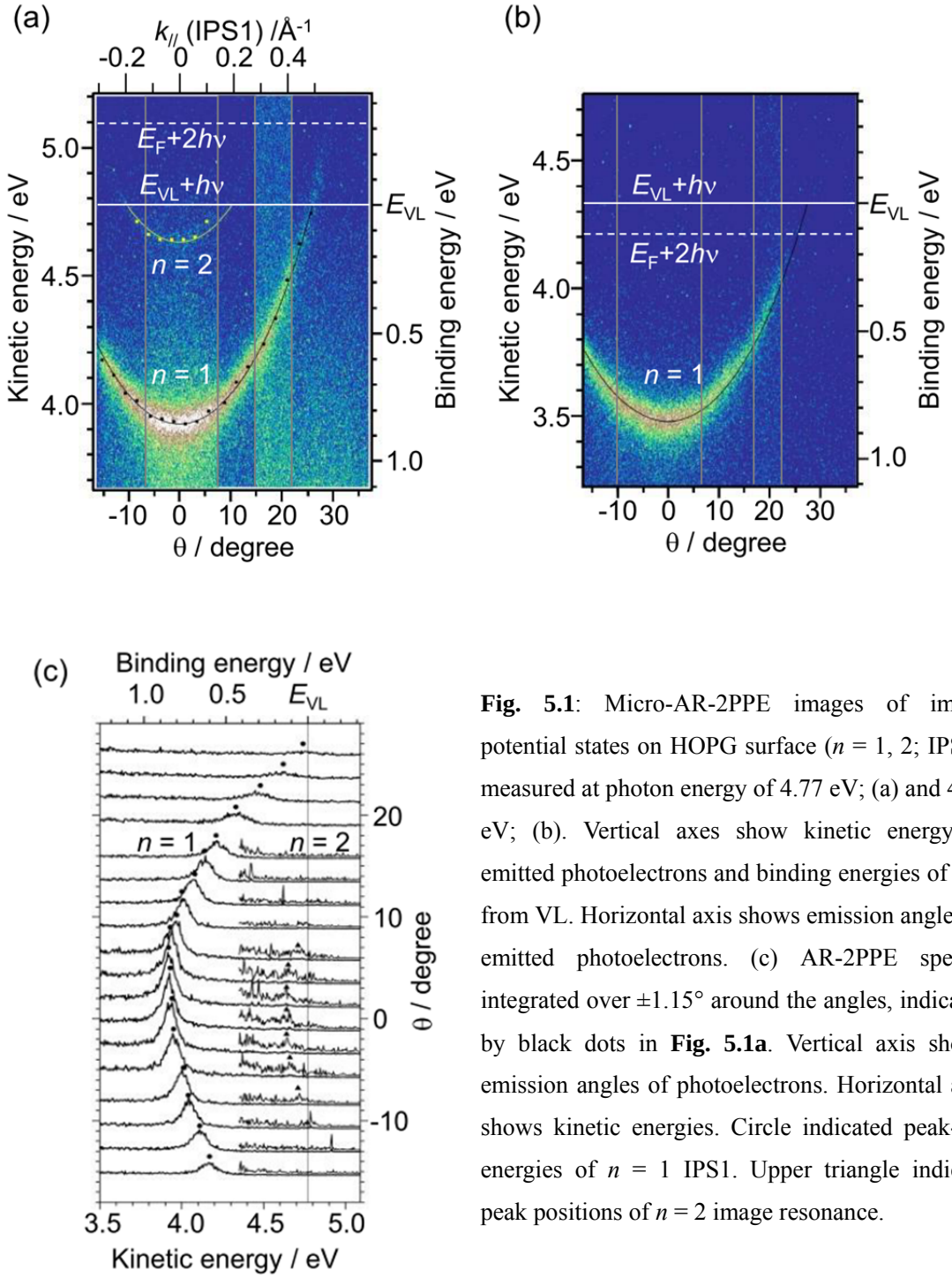

Fig. 5.1: Micro-AR-2PPE images of image potential states on HOPG surface (n = 1, 2; IPS1), measured at photon energy of 4.77 eV; (a) and 4.33 eV; (b). Vertical axes show kinetic energy of emitted photoelectrons and binding energies of IPS from VL. Horizontal axis shows emission angles of emitted photoelectrons. (c) AR-2PPE spectra integrated over ±1.15° around the angles, indicated by black dots in **Fig. 5.1a**. Vertical axis shows emission angles of photoelectrons. Horizontal axis shows kinetic energies. Circle indicated peak-top energies of n = 1 IPS1. Upper triangle indicate peak positions of n = 2 image resonance.

From the result, we can confirm that detected electrons were ejected by two-photon excitation process. The solid horizontal lines in **Fig. 5.1(a)** and **1(b)** correspond to E_{VL} + $h\nu$where E_{VL} is the energy of VL. It is interesting that the IPS1 in **Fig. 5.1(a)** is still

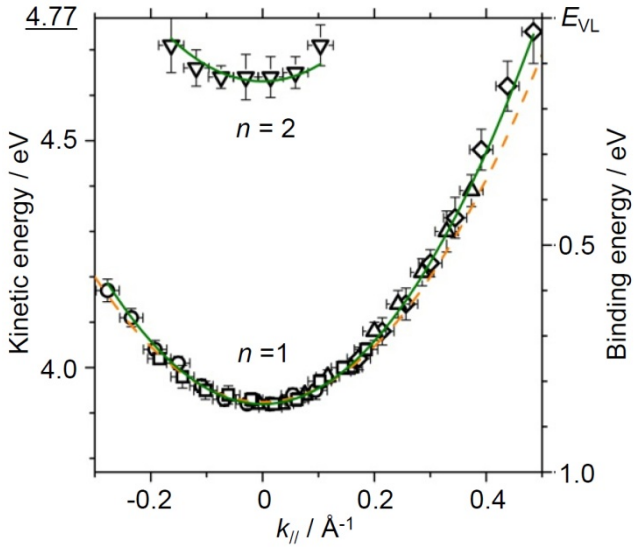

Fig. 5.2: Dispersion of IPS1 is shown. Peak positions of n = 1, 2 is plotted against $k_{//}$. Four symbols (circle, square, triangle, diamond) are used to distinguish results obtained from different measurements. By parabolic fitting, the effective of n = 1 IPS1 is m* / m_e = 1.10 ± 0.02 (solid curve). The fitting curve is shown as solid line. n = 2 image resonance is also fitted as m^* / m_e = 1.1. In the range of -0.2 < $k_{//}$ < 0.2, the effective mass of n = 1 IPS1 is m^* / m_e = 1.24 ± 0.08, shown as dot line.

visible even above the solid line, E_{VL} + $h\nu$. Since IPS is supported by the image potential converging to VL, it cannot exist at energy higher than VL. However, the excitation to IPS above E_{VL} is known in multi-photon photoemission from Cu(001).[ref] Occurrence of IPS above E_{VL} for large θ region corresponds to the total internal reflection of electrons at the surface-vacuum interface.

Fig. 5.1(c) shows the spectra integrated over ±1.15° around the angles indicated by black dots in **Fig. 5.1(a)**. The peak energies are plotted in Fig. 2 against the electron wavenumber parallel to the surface ($k_{//}$) defined by $k_{//} = (2m_eE_k / \hbar^2)^{1/2} \times \sin\theta$, where m_e is the mass of electron. The dispersion is fitted with a parabolic function of $E_k = \hbar^2 k_{//}^2 / 2m^*$, where m^* is the effective mass of electron. The IPS1 crosses VL at θ = 26.3°or $k_{//}$ = 0.495 Å^{-1}. The effective mass estimated by fitting in the range of -0.3 < $k_{//}$ < 0.5 Å^{-1} is m^*/m_e = 1.10 ± 0.02 (solid curve in **Fig. 5.2**). While the value fitted in the range of -0.2 < $k_{//}$ < 0.2 Å^{-1} is m^*/m_e = 1.24 ± 0.08 (dot curve in **Fig. 5.2**) in agreement with an

our former data [36] and an IPES result [51]. The decrease of m^* values at higher $k_{//}$ is small but is reproducible as can be seen in both **Fig. 5.1(a)** and **(b)**. The experimental bright points are located slightly above the fitted line. The results means that nearly free electron model is *not* proper approximation at the higher momentum region of IPS1. A calculated band structure suggests that IPS1 energetically overlaps with an unoccupied band of graphite (indicated as σ^*) [52]. The effective mass ratio of σ^* is ~0.9 in Γ-K direction [52]. Hybridization of IPS1 with the σ^* band causes the decrease in the effective electron mass ratio. The hybridization is rather resemble to the hybridization between the unoccupied Shockley state and the bulk states was reported for Cu(111) [90].

The second member (n = 2) of the IPS is weakly observed in **Fig. 5.1(a)**. The state is above the bottom of the σ^* band and should be called as an image resonance. The intensities of the n = 2 image resonance is too weak for quantitative discussion of the dispersion, but it seems to fit well to a parabolic curve of m^*/m_e = 1.1 as shown by the thin solid curve. The bottom of the band is at 0.14 eV below VL in agreement with the value in references [36, 48]. The binding energy of IPS is typically fit on an equation of $E_n = E_{VL} - 0.85/(n + \delta)^2$ eV, where δ is the quantum defect [59]. The obtained δ values for n = 1 and 2 IPS on HOPG are 0 and 0.46, respectively. The largely different δ value should be a result of the interactions between IPS and the bulk band structure.

5.2 Image potential states on 1ML PbPc film

Fig. 5.3 shows our preliminary STM image of the 1 ML PbPc film on HOPG. The molecules form a well-ordered nearly square lattice of about 14 Å spacing. The lattice constant is comparable to the reported value of 13.8 Å for CuPc film on HOPG [86]. The IPS on the film (denoted as IPS2) is located at 3.51 eV above E_F. The work

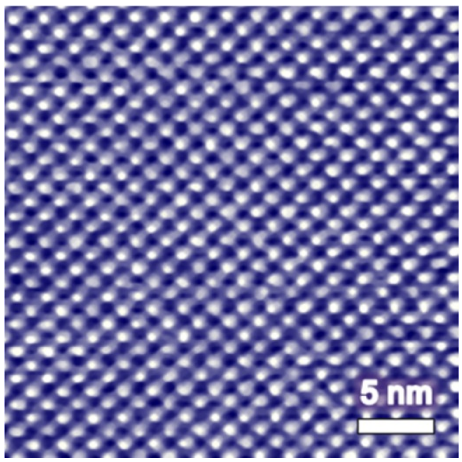

Fig. 5.3: A STM image (30 × 30 nm^2, V_s = + 0.51 V, I = 0.30 nA) of 1ML PbPc film on HOPG. The molecules are sitting on a well-ordered nearly rectangular lattice of ~ 14 Å spacing.

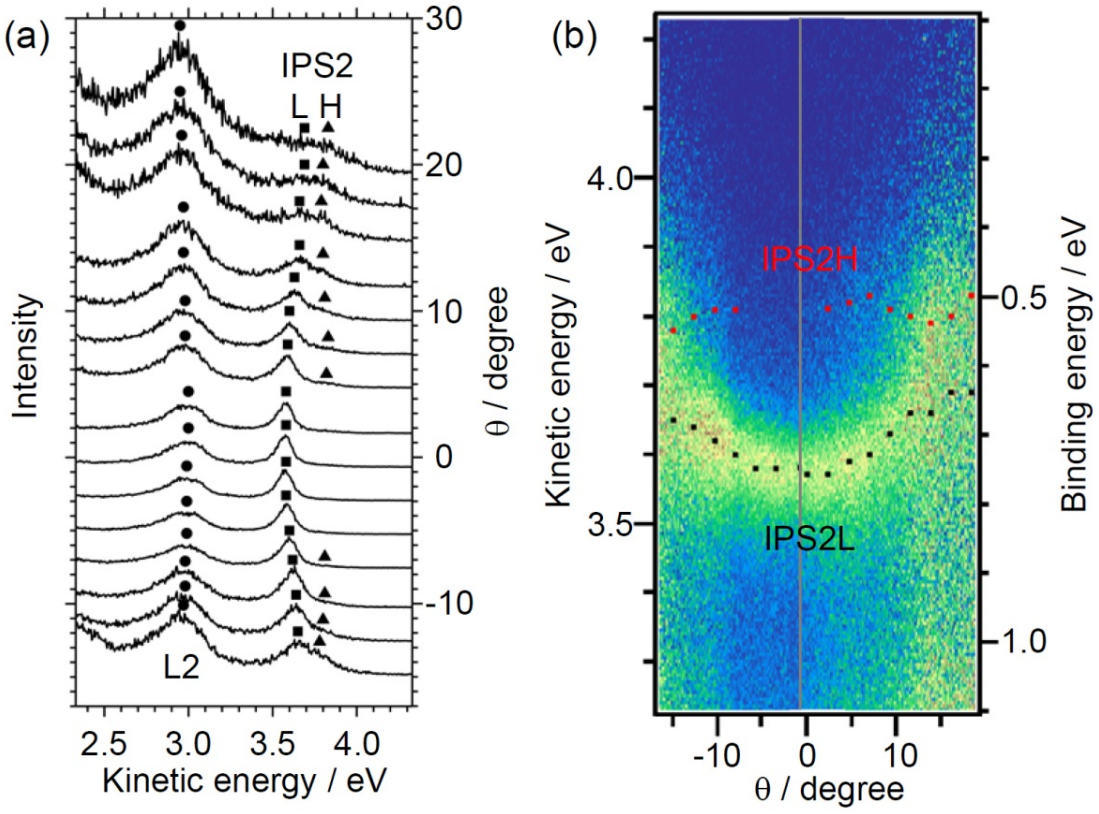

Fig. 5.4: (a) AR-2PPE spectra of 1 ML PbPc / HOPG. IPS on PbPc film (IPS2) is split to two structures (IPS2 L and H) and band folding is observed. The spectra are normalized by intensity of IPS2 L to enhance band folding at large emission angles. A peak (L2) derived from LUMO+2 states of PbPc are also observed in the spectra. (b) AR-2PPE image of 1 ML PbPc / HOPG, normalized the intensity of IPS2 L is shown. AR-2PPE spectra integrated over ±1.15° around the angles, indicated by black dots in **Fig. 5.1(a)**.

function of 1ML PbPc/HOPG is 4.27 eV and the binding energy relative to VL is 0.76 eV [19, 36]. The micro-spot AR-2PPE spectra and the AR data are shown in **Fig. 5.4(a)** and **(b)**, respectively. The photon energy is 4.33 eV. Because the photoemission intensity rapidly decreases as the emission angle increases, the spectra and the AR image is normalized to the peak height at the solid square (denoted as IPS2L) in **Fig. 5.4(a)**. It is interesting that the IPS2 peak becomes broad at large emission angle, and a weak peak is seen as shown by triangle in **Fig. 5.4(a)** (denoted as IPS2H). The energies of the circles and triangles are plotted in **Fig. 5.5** against $k_{//}$. In the former report [36], the lower part of the IPS2 was fitted to the parabola curve of $m^* / m_e = 2.2 \pm 0.3$ in the ranges of $-0.1 < k_{//} < 0.2$ Å^{-1} as shown by broken line in **Fig. 5.5**. By extending the measured $k_{//}$ range, deviation from the broken line is evident at high $k_{//}$. The IPS2H is the folding of the band at the Brillouin zone boundary. A gap is formed between the IPS2L and IPS2H components.

The modifications of the IPS band structures by periodic potentials induced by super-lattice have been discussed for several surfaces. Binding energies of IPS on vicinal noble metal surfaces (Au(788) etc.) were analyzed by 1D Kronig-Penny model which assumed transmission probability at the step edge [90, 91]. The modifications of IPS by periodic potential are also observed in several organic/metal surfaces. As for benzene covered Cu(111) surface, two type of IPS were observed; free-electron like IPS on benzene monolayer and modulated IPS on benzene bilayer. The modulated IPS for bilayer film was reproduced by a Kronig-Penny model [92]. The dispersions of IPS on CuPc / Ag(111) and FePc / Ag(111) were explained by 2D Kronig-Penny models [34].

We analyze the dispersion by adopting 1D Kronig-Penny model because the lattice is nearly square. With the δ-functional barrier, the band structures are described as [22]

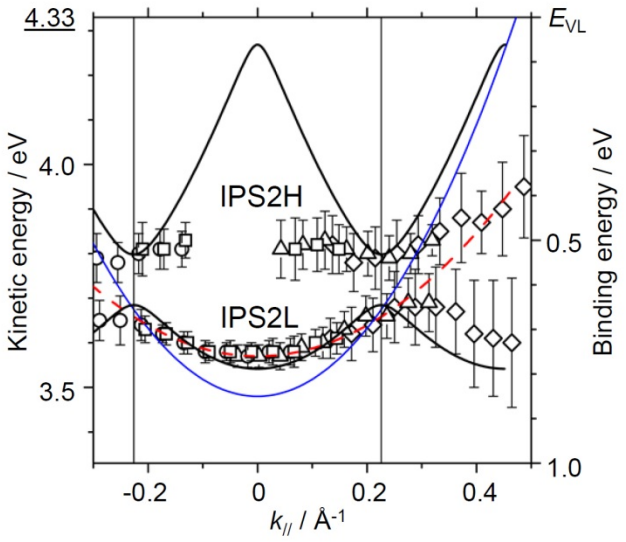

Fig. 5.5: Dispersion of IPS2 is shown. The photon energy is at 4.33 eV. Peak positions of IPS2 on **Fig. 5.4a** are plotted against $k_{//}$. Four symbols (circle, square, triangle, diamond) are used to distinguish results obtained from different measurements. The idealized dispersion curve of free-electron is shown as thin solid line. The observed dispersion is changed from free-electron. Parabolic fitting of IPS2L in the range of $-0.1 < k_{//} < 0.2$ is shown as dot-dashed curve. The effective mass is $m^* / m_e = 2.2 \pm 0.3$. Calculated band structure from Kronig-Penny model which assumed periodic potential formed by super-lattice of PbPc, is shown as bold solid curve. The dispersion curve of IPS1 is also shown as thin solid curve. By Kronig-Penny model, we can qualitative explanation why IPS2 is up-sifted and why band splitting is occurred.

$$P \times \sin(Ka) / Ka + \cos(Ka) = \cos(ka) \qquad \textbf{(5.1)}$$

where P is a parameter related to the transmission probability through the barrier. a is the periodicity of the potential and k, an index to label the solutions. The eigenvalue of the Schrödinger equation ε is expressed as $\varepsilon = \hbar^2 K^2 / 2m$. K is the wave number of plane waves. The calculated band structure of **eq (5.1)** is shown by the thick solid lines in **Fig. 5.5**. Also shown by the thin solid line in **Fig. 5.5** is the dispersion curve of IPS1 on clean graphite. The zone boundary is shown in **Fig. 5.5** by vertical lines. With the parameters of 13.9 Å and 1.7 for a and P, respectively, the curvature of the IPS2L band and the band gap at the zone boundary are semi-quantitatively reproduced. The effective mass of IPS2 is significantly heavier than that of IPS1 because the electron is trapped by

the molecule. The energy separation between IPS1 and IPS2L at $k_{//} = 0$ is also roughly reproduced. The periodicity a is in good agreement with the lattice constant in **Fig. 5.3**. The dimension-less parameter P originates from potential at the zone boundary. This parameter determines magnitudes of band gap at the zone boundary and the binding energy of bands at Γ point. From the fitted P value of 1.7, the potential barrier at the zone boundary can be evaluated as $V_0 b = 0.93$ eV Å, where V_0 is the barrier height, and b, the width of the barrier. The $V_0 b$ value is slightly smaller than that for steps on Au(788) (1.2 eVÅ) and those for FePc and CuPc/Ag(111) (1.5 eVÅ). Because IPS2 is hybridized with an unoccupied molecular orbital [36], an electron trapped in a molecule may easily transmit to nearby molecules. The dispersion of the IPS2H component is smaller than the calculation. Because the band width of the unoccupied molecular level hybridizing with IPS2 should be narrower than 0.3 eV similarly to the L2 peak in **Fig. 5.4(a)**, the energy of the hybridized IPS2 cannot be high as the free electron.

In PbPc/HOPG system, interactions between molecule-derived levels and IPS2 should be taken into account. The energy levels of the PbPc film are shown in **Fig. 5.6(d)**. The highest (lowest) occupied (unoccupied) molecular orbital derived level is denoted as H0 (L0) and the deeper (higher) lying levels are denoted by H-1 (L1 and L2). The IPS2 is excited from occupied band of HOPG with non-$k_{//}$ conserving process when the pump photon is off-resonant from the H0-IPS2 energy separation. The intensity becomes high as the pump photon energy becomes close to the H0-IPS2 resonance of 4.84 eV [36]. The H0-IPS2 resonance may affect the dispersion of the IPS2. In addition, the H0-L2 resonance may affect the dispersion of the IPS2. In addition, the H0-L2 resonance may have some influence on the IPS2 if the L2 and the IPS2 are interacting. In order to clear these possibilities, photon energy dependence is shown in

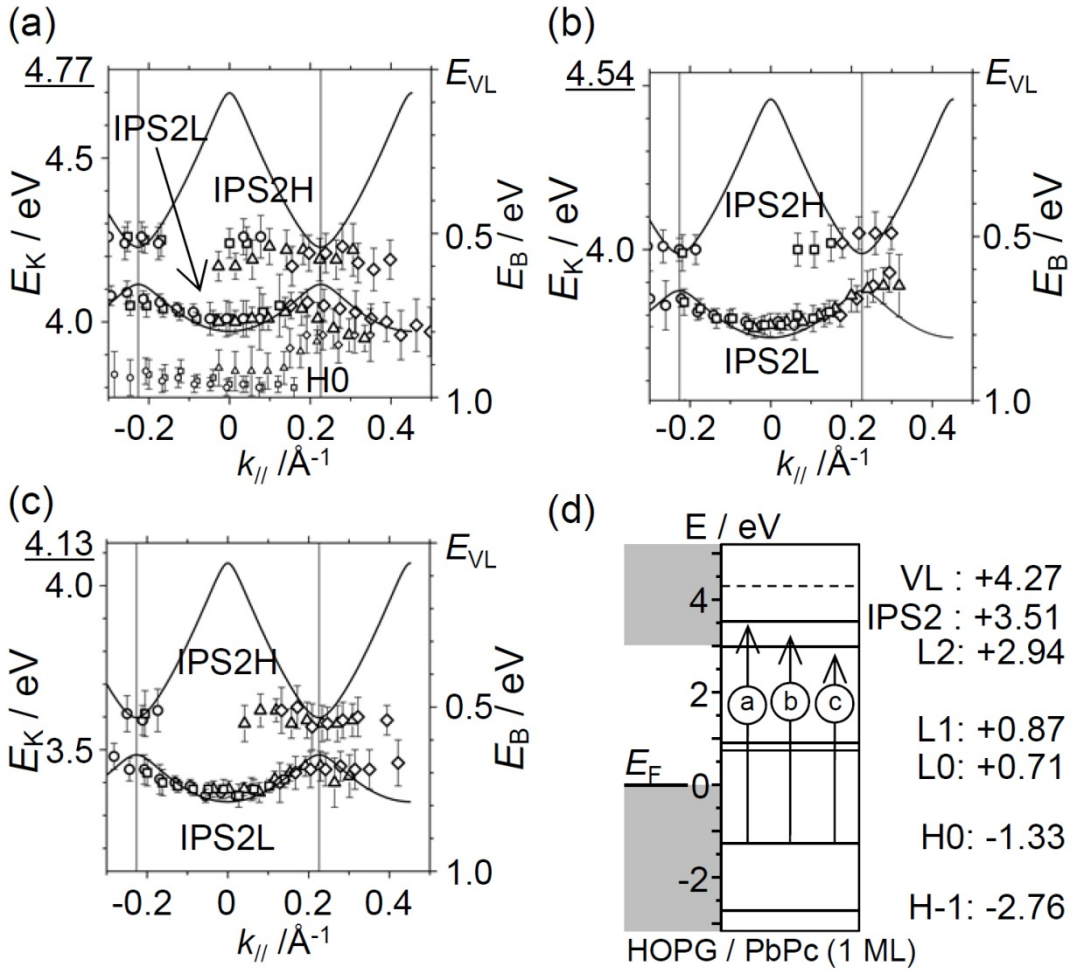

Fig. 5.6: Dispersion of IPS2 is shown. The photon energy is at 4.77 eV; (a), 4.54 eV; (b), and 4.13 eV; (c). Peak positions of IPS2 are plotted against $k_{//}$. Four symbols (circle, square, triangle, diamond) are used to distinguish results obtained from different measurements. (d) Energy diagram of 1ML PbPc / HOPG is shown. Excitation from HOMO to IPS2 is considerable at photon energy of 4.77 eV in **Fig. 5.5a**, however, there are no significant difference on dispersion of IPS2.

Fig. 5.6(a)-(c). The photon energy is the same as the kinetic energy labeled by the underline. In **Fig. 5.6(a)** where the photon energy is close to the H0-IPS2 resonance, the IPS2 peak becomes strong and partially overlapped with the HOMO peak. The photon energy in **(b)** is in between the H0-L2 and the H0-IPS2 resonances. **Fig. 5.5** is measured at the H0-L2 resonance. The result in **Fig. 5.6(c)** is for the photon energy below the H0-L2 resonance. The black lines are the model results calculated with the same parameters as **Fig. 5.5**. Irrespective of the different photoelectron energies and different

resonant conditions, the model curves fit with experimental results in a similar extent as **Fig. 5.5**. The resonance between H0 and L2 derived levels causes no effect on the dispersion of the IPS2. The resonance between H0 and IPS2 does not cause significant change of the dispersion of IPS2. The result confirms that interaction between the L2 derived level and IPS2 is negligibly small.

We described that the unoccupied molecular orbital hybridizing with IPS2 may be LUMO+3 [36]. Taking into account of the many nodes of the π-orbital within the molecular plane, and taking into account that the molecules are lying flat on the substrate, it seems rather difficult to consider the hybridization of LUMO+3 with plane wave of IPS2. In C_{60} film, super-atom molecular orbital (SAMO) and their hybridization into the nearly free electron bands of fullertites are known [93-96]. Similarly, the diffuce orbitals may be contributing to the hybrization between IPS2 and molecule-derived unoccupied states.

5.3 Chapter summary

In this chapter, dispersions of image potential states on graphite surface (denoted as IPS1) and on 1 monolayer (ML) film (denoted as IPS2) of lead phthalocyanine (PbPc) are investigated by the micro-spot angle-resolved two-photon photoemission (micro-AR-2PPE) spectroscopy. On the graphite surface, whole dispersions of the two members of IPS1 (n = 1 and 2) are observed. The effective mass of electron in the n = 1 IPS1 becomes slightly light at high momentum region. These results suggest the interaction between the IPS1 and the unoccupied σ-band of graphite. On the PbPc film, the IPS2 band forms a band gap and back-folds at the boundary of the Brillouin zone. 1-dimensional Kronig-Penny model (see, **Fig. 5.7**) is used to reproduce the effective mass and the shift of binding energy.

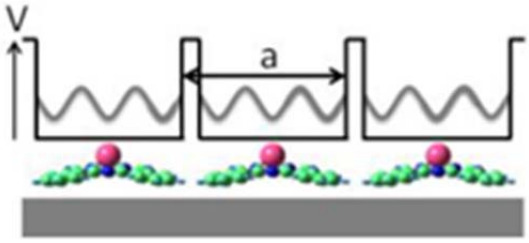

Fig. 5.7: Schematic image of the periodic potential which formed on well-ordered PbPc monolayer

6. Delocalization of an unoccupied level which derive on monolayer film of lead phthalocyanine surfaces

In this chapter, we focus on the issue that localization or delocalization problems of the unoccupied states of the first organic layer. Recently, there are several reports of delocalized unoccupied states on the surface [29-35]. However, observed states are strongly mixed with surface state or bulk state of substrate. There is no observation of delocalized, unoccupied levels of the first organic layers, which derived from *pure molecular orbital*s of organics.

One of the reported interfaces is between PTCDA/Ag(111). Ag(111) surface has a 2D free-electron like *Shockley state*. The state is partially occupied (below E_F) near the Γ point. In the case of PTCDA/Ag(111) surface, the state is up-shifted to above E_F (unoccupied) and form an *interfacial state* (IS) by hybridization with unoccupied states of the PTCDA molecule [29-31]. The dispersion of the IS is m*~1 around the Γ point, and they show band gaps and band-folding corresponds to the reciprocal lattice to the super-lattice of the PTCDA film. We can say the IS is delocalized, but it isn't mean that a pure, unoccupied molecular orbital is delocalized among neighboring PTCDA molecules and forming a band, because that the *Shockley state* is delocalized.

Recently, fullerene (C_{60})/metal surfaces are studied extensively and delocalized super-atomic states are observed [93-96]. C_{60} is the most famous n-type organic semiconductor; therefore, unoccupied states of C_{60} are extensively studied. In STM and STS studies of sub-ML or 1 ML of C_{60}/Cu(111) surfaces, LUMO and LUMO+1, LUMO+2 state of the molecule is observed. Super-atom states (SAMO) which has higher energy also observed and their hybridization into the nearly free electron bands of fullertites are reported [93, 94]. The SAMO states are also observed by 2PPE study

and their dispersion is observed [95, 96]. The result shows the SAMO states are delocalized.

As shown as above, there are several studies on the unoccupied levels at organic/inorganic interfaces. However, observed unoccupied states of organic thin films may be strongly hybridized with electronic structures of substrates. Facing issues in this chapter is that unoccupied states which originate molecular orbitals on organic/inorganic interfaces are delocalized even if molecule-substrate interaction is weak (hybridization with bulk structure is weak).

Therefore, we studied dispersion of the L2 level (which derived from LUMO+2 molecular orbital of PbPc) on 1ML PbPc/HOPG surface. We used AR Micro-spot 2PPE to measure dispersion of the L2 level. All occupied and unoccupied states around the Fermi level are observed and determined their origin in **chapter 3**. We have confirmed that monolayer film of PbPc on HOPG forms well-ordered structure, studied by PEEM. We have found that even if the film structure is laterally homogeneous, unoccupied levels (L0/L1) are *inhomogeneous*, which has been shown in **chapter 4**. Thus even in the case of measuring dispersion of well-ordered organic films, the observed results may shows position dependence. AR Micro-2PPE can get reproducible dispersion measurements by choosing the light spots on highly well-ordered domains and avoid effects of defects and scratches on the sample. We have shown dispersion of the image potential state on the film (IPS2) in **chapter 5**. We can detect dispersion of L2 by the same method and can discuss delocalization of the L2 from the dispersion. Furthermore, momentum distribution of excited electrons in L2 is derived from relations between photoemission intensity and wave momentum of photoelectron. From the distribution, extent of wave function of L2 in real space is estimated as several nm. The result shows

the fact that excited electrons on L2 are delocalized among several molecules..

6.1 Results

The micro-spot AR-2PPE spectra and the AR data are shown in **Fig.6.1(a)** and **(b)**. These data are obtained from the same sample as **Fig. 5.4(a)**. **Fig.6.1(a)** and **(b)** are drawn by putting together the AR results measured by rotating the sample normal direction from the energy analyzer by angles of -5°, 0°, 10°, and 20°. The photon energy is 4.33 eV. Two peak structures, indicated as IPS2 and L2 are observed. Kinetic energy of photoelectrons from IPS2 is 3.57 eV and that of L2 is 2.99 eV at 0°. The photoemission intensity rapidly decreases at the high emission angle. Therefore, intensities of the AR image need to be normalized to each emission angles to considering to band structures at high emission angle. We also consider the secondary electron which is overlapping on the L2 peak in high emission angle, because that photoelectron has positive dispersions at cut-off region of the spectra.

We did data processing as following. (1) 2D images of AR Micro-spot 2PPE (**Fig. 5.4(a), (b)**) is corrected. These images are normalized by the intensity of IPS2L (by each angles). (2) From normalized images, angle integrated spectra (**Fig.6.2(a)**; integrated over ±1.15° around the angles indicated by black dots in **Fig.6.1(a)**) are created. Peak positions of IPS2L, H, L2, H0 are indicated by square, triangle, circle, diamond. (3) We assumed that backgrounds of secondary electrons in 2PPE spectra are expressed as a single exponential function (solid lines in **Fig.6.2(b)**). Spectra which subtract the backgrounds from **Fig.6.2(b)** are created (**Fig.6.2(c)**). The positions of the peaks were not changed by subtracting process (Positions of square, triangle, circle, diamond are same as **Fig. 6.2(a)** and **(b)**.) (4) By sums up of the spectra of **Fig.6.2(c)**, we recreated the intensity map in **Fig.6.1(c)** and **(d)**. Validity of the analysis is discussed

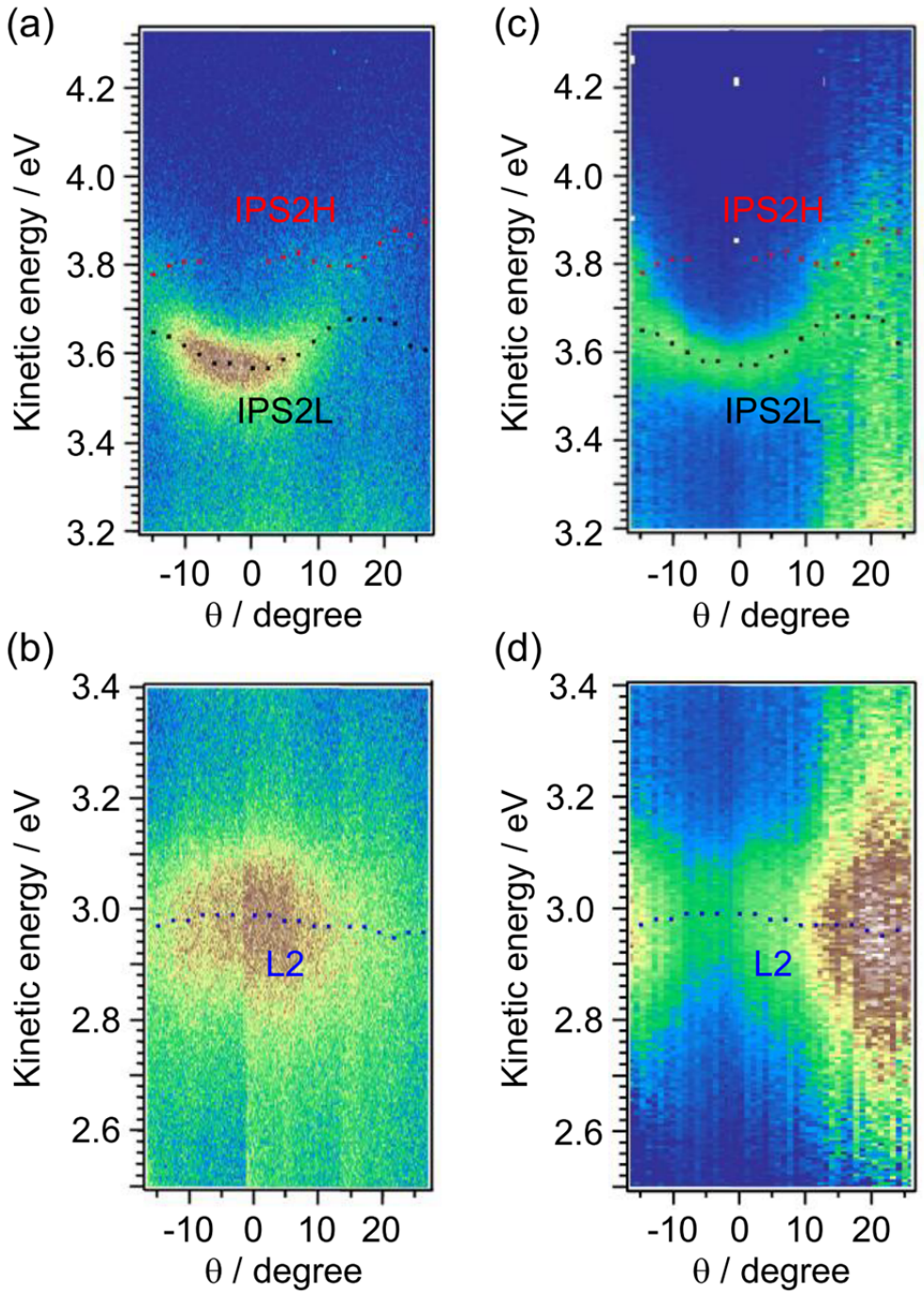

Fig. 6.1: Micro-AR-2PPE images of image potential states on 1ML PbPc/HOPG surface; (a) and images of L2; (b). These spectra are measured at photon energy of 4.33 eV. Vertical axes show kinetic energy of emitted photoelectrons. Horizontal axis shows emission angles of emitted photoelectrons. To analysis momentum distribution of the L2 state, these images are normalized by the intensity of the IPS2L peaks (black dots). Then backgrounds of secondary electrons are subtracted. Finally, we obtained the images (c) (IPS region) and (d) (L2 region).

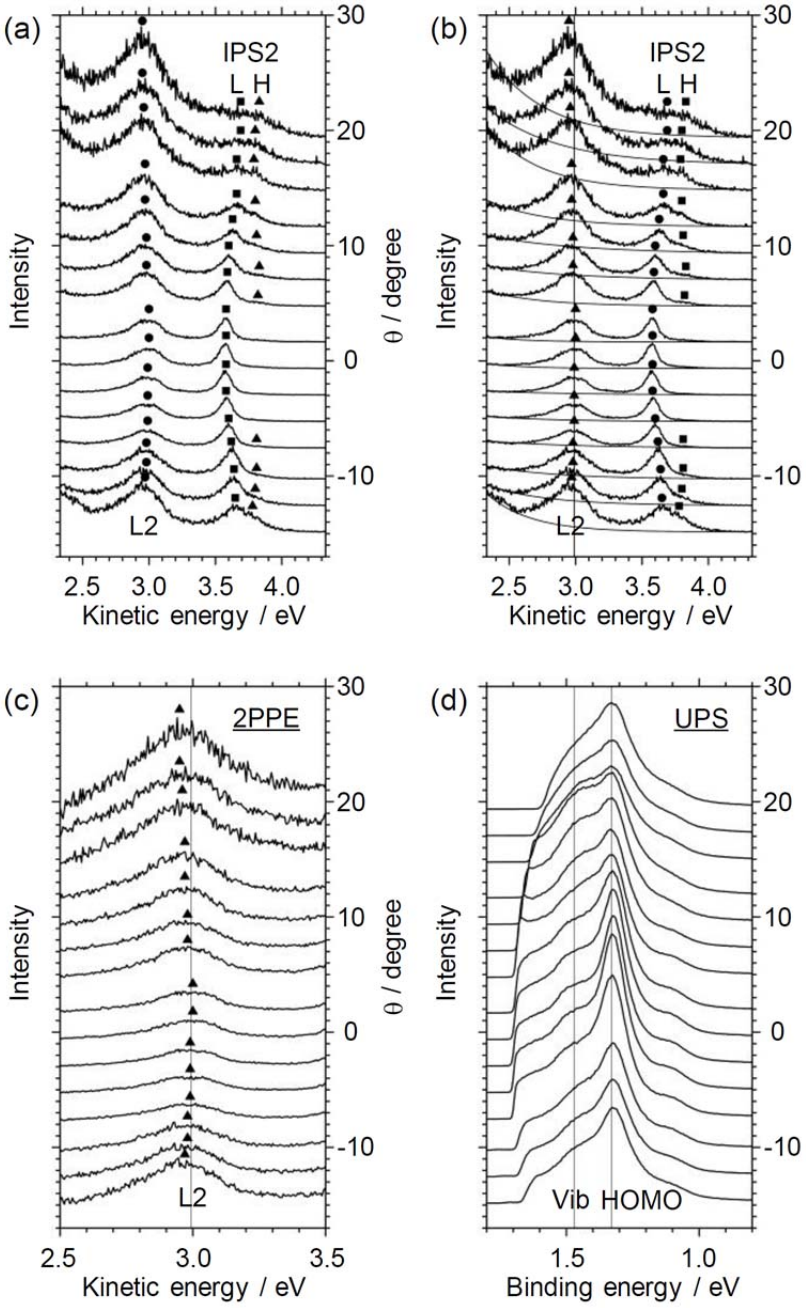

Fig. 6.2: (a) Intensity normalized AR-2PPE spectra of 1 ML PbPc / HOPG, integrated over ±1.15° around the angles by black dots in **Fig.6.1(d)**. The spectra are normalized by intensity of IPS2 L to enhance band folding at large emission angles. (b) Backgrounds formed by secondary are added on (a). Negative dispersion of the L2 levels (derived from LUMO+2 states of PbPc) is observed. (c) After subtracting the backgrounds. The indicated peak positions of the L2 are same as (a). (d) AR-UPS spectra of 1 ML PbPc / HOPG, measures on the same sample. The photon energy is 6.05 eV, with P-polarized light. The sample bias is -3V. HOMO peak and their vibrational structures (indicated as vib.) are observed and reproduced former results in **section 3.2.2** and **ref. [26**, **36]**.

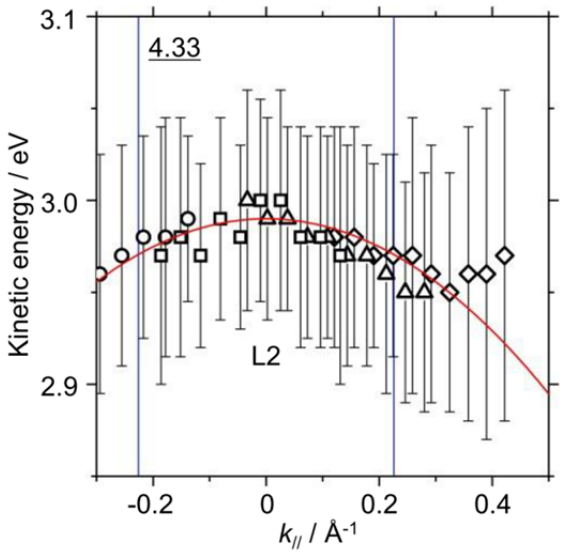

Fig. 6.3: Dispersion of L2 is shown. Peak positions of L2 is plotted against $k_{//}$. Four symbols (circle, square, triangle, diamond) are used to distinguish results obtained from different measurements. By parabolic fitting, (in the range of $-0.3 < k_{//} < 0.3$) the effective of L2 is $m^* / m_e = -10$ (solid curve). The fitting curve is shown as red line. The blue solid lines indicated the zone boundaries of IPS2L, which have been shown in **chapter 5**.

in the following section.

We focus our attention on the L2 level, which derived from the LUMO+2 orbital of PbPc. In **Fig.6.2(c)**, 2PPE spectra, around the L2 peak are shown. The dispersion relation of the L2 peak (indicated by triangles in **Fig.6.2(a)** and blue dots in **Fig.6.1(d)**) are plotted in **Fig.6.3**, against $k_{//}$. The L2 shows slight negative dispersion. It means that excited electrons, to the L2 level, are delocalized. The L2 was fitted to the parabola curve of $m^*/m_e = -10$ in the ranges of $-0.3 < k_{//} < 0.3$ Å^{-1} as shown by the red curve in **Fig.6.3**. In **chapter 5**, we have shown that IPS2 shows band-folding and band gaps. Therefore we expect to observe such structures of the L2 band at Brillouin zone boundary. But the band width of the L2 band is wider than their small dispersion, we couldn't observe band gaps and band folding of the L2 band.

We also measured dispersion of HOMO level by AR Micro- UPS. By replacing the light source to 4th harmonics of the titanium: sapphire laser, we can apply

micro-AR-2PPE and micro-AR-UPS for the same sample within the same equipment. **Fig.6.2(d)** shows micro-AR-UPS spectra of HOMO for same sample to **Fig.6.2(a)-(c)**. HOMO levels which derived from π orbitals of the phthalocyanine, does *not* show dispersions. To correct low energy photoelectrons, we had to apply sample bias (-3V) for AR-UPS study. The field may effect on the pathway of the emitted electrons, thus we cannot convert emission angles to $k_{//}$ and cannot discuss E-$k_{//}$ relations. However, the localized HOMO level (H0) match with former studies about HOMO band of PbPc and several phthalocyanine surfaces, measured by AR-UPS [8].

6.2 Negative dispersions of the L2 state

We start our discussions from the electron excitation process to the L2 levels. The photon energy in **Fig.6.1(a)** is 4.33 eV. The energy is corresponds to the energy difference of HOMO and L2 of the 1ML PbPc film. Considering the spatial overlaps of the wave functions, we think that most of the excited electrons in L2 are excited from HOMO. Spectroscopies of organic solids frequently observe Frenkel exciton [97] and exciton states are also observed in 2PPE spectra [11]. Exciton peak in 2PPE shows no dispersion because electrons are strongly localized and $k_{//}$ are not conserved. We obtained **Fig.6.1(a)** in zero delay condition (no delays between pump and probe pulses) and at room temperature. In the condition, we only observed delocalized L2 state. Thus, excited electrons in L2 are delocalized soon after photoexcitation.

In order to clear the possibility of dispersion change at the HOMO-L2 resonance, photon energy dependence is examined. The 2PPE spectra with various photon energies are shown in **Fig.6.4**. Dispersion relations in **Fig.6.4(a)-(c)** are shown in **Fig.6.5**. The photon energy is the same as the kinetic energy labeled by the underline. In the photon energy of 4.77 eV, the HOMO peak is above; far away from the L2 peak. The photon

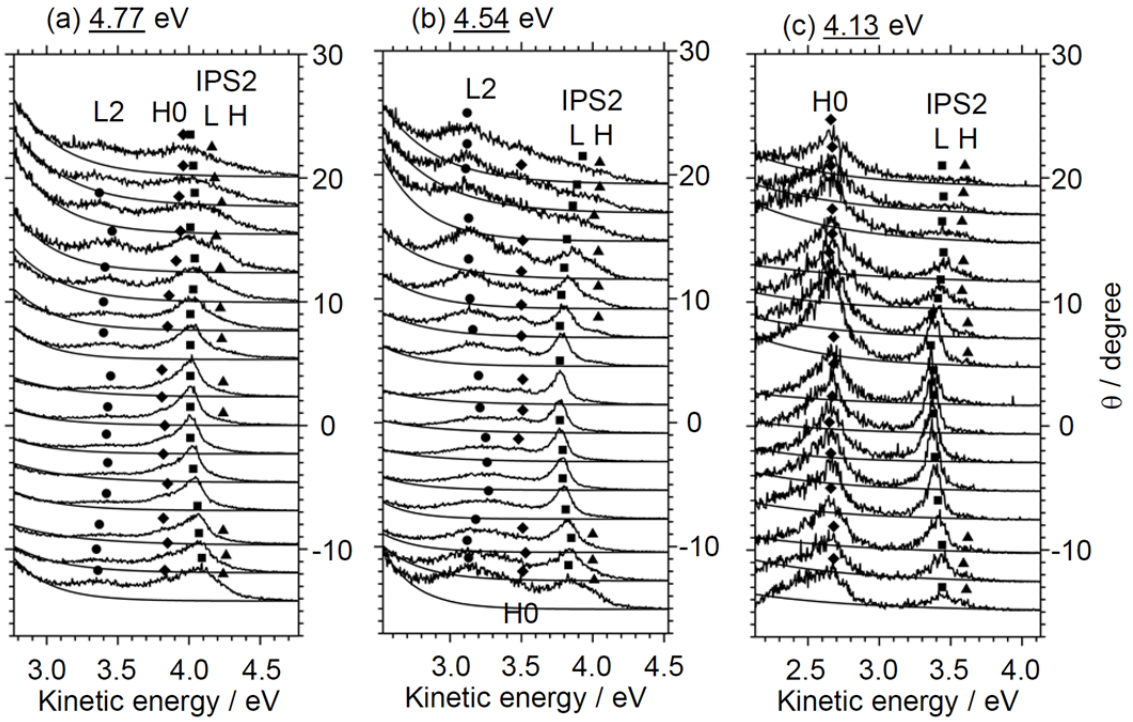

Fig. 6.4: 2PPE spectra with different photon energies are shown. The photon energies are shown in the figure with underline. These spectra are integrated over ±1.15°in 2D AR-2PPE images of 1 ML PbPc / HOPG, normalized by intensity of IPS2 L. Backgrounds are show as thin solid curves. Negative dispersion of the L2 levels (derived from LUMO+2 states of PbPc) is observed.

energy of 4.54 eV is in between the H0-L2 and the H0-IPS2 resonances. We observed a broad peak and we cannot divide the peak to HOMO and L2. **Fig.6.3** is measured at the H0-L2 resonance (4.33 eV). The result of 4.13 eV is for the photon energy below the H0-L2 resonance. We cannot observe the L2 peak and only HOMO peak (*localized*) is observed. The black lines in **Fig.6.5(a)-(c)** shows a parabola curves with the same parameters as **Fig.6.3**. Irrespective of the different photoelectron energies and different resonant conditions, the resonance between H0 and IPS2 does not cause significant change of the dispersion of L2. The observed dispersion of **Fig.6.3** is that of L2. The result means that excited electrons in L2 does not significant affect to holes created in HOMO. We consider the reason why electrons do not effect on holes is that holes which created in HOMO are rapidly shielded by substrate. On small-molecule adsorbed

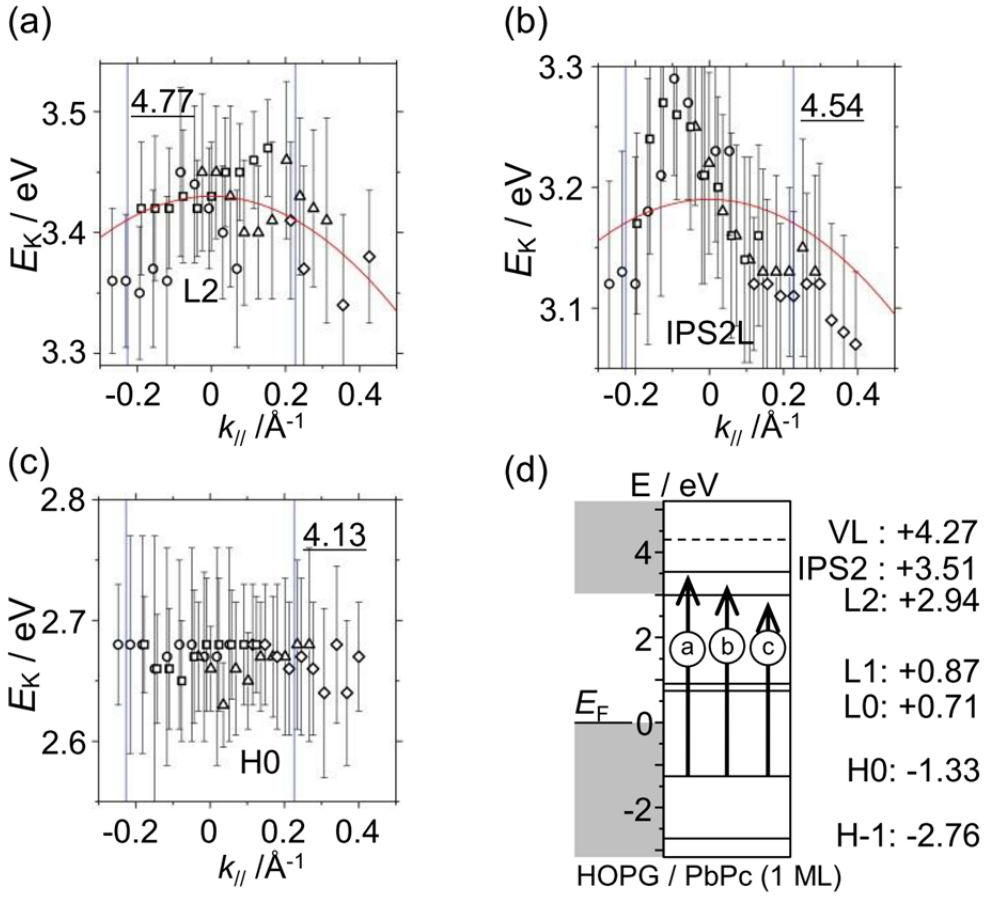

Fig. 6.5: Dispersion of L2 (HOMO; (c)) is shown. The photon energy is at 4.77 eV; (a), 4.54 eV; (b), and 4.13 eV; (c). Peak positions of the L2 (H0) in these figures are adopted from **Fig. 6.4** (a), (c), (e) and plotted against $k_{//}$. Four symbols (circle, square, triangle, diamond) are used to distinguish results obtained from different measurements. (d) Energy diagram of 1ML PbPc / HOPG is shown. Resonance from HOMO to L2 is considerable at photon energy of 4.33 eV in **Fig.6.3**, however, there are no significant difference on dispersion of L2.

surfaces, TR-2PPE shows that excited electrons into delocalized IPS are localized after several hundred fs [9-11, 41]. The effects are explained with redistribution of electrons of dielectric adsorbate (*electron solvation*) [98, 99]. The band of amorphous ice layer on metal shows change of binding energy within several hundred fs, because of dipole effect. In case of L2 we don't observe such a dynamic localization effect, because of the short lifetime of the L2 states. Fermi liquid model estimates that lifetimes of excited electrons are proportional to $1/(E - E_F)^2$ [100]. Our former study shows that life time of

L2 is 134 fs [36]. Thus, the excited electrons are relaxed without dynamic localization effects.

6.3 Momentum distribution of the L2 state

Next, we discuss wave momentum distributions of excited electrons in L2, and then discuss with lateral distribution of excited electrons. At the beginning we consider why photoelectron intensity in **Fig.6.1(a)** show emission angle dependence. There are three main reasons for the intensity difference; (1): the electron energy analyzer has different efficiency of detecting photoelectrons for different emission angles. (2): The intensity of L2 has wave-momentum dependence; because of that transition probability from initial state to L2 is different. From now, we evaluate our data analysis described in **section 6.1** is proper or not. We normalized **Fig.6.1(a)** by the intensities of IPS2L. Electrons are excited from bulk band of HOPG to L2 level. We think the transition probability from bulk band to IPSL2 does not show angle dependence. Then, we think intensity-angle relation in **Fig.6.1(d)** derived from the efficiency of the analyzer. The efficiency is intrinsic to the analyzer and is not to depend on the kinetic energy of the photoelectron (the energy difference of L2 and IPS2L is too small). By normalizing the AR image, the efficiency is corrected and we only consider momentum distributions of L2; case (2). After subtract the background, obtained images (**Fig.6.1(d)**) reflect momentum ($k_{//}$) distributions of the L2. In **Fig.6.1(d)**, intensity of L2 at 10° is 3 times greater than that of 0°. The reason of these differences is not originated from the weak intensity of IPS2 by scattering super-lattice. Large emission angles correspond to high wave momentums. Therefore, short wavelength components of L2 are larger than long wavelength components.

We can qualitatively explain L2's negative dispersion by tight-binding model. The

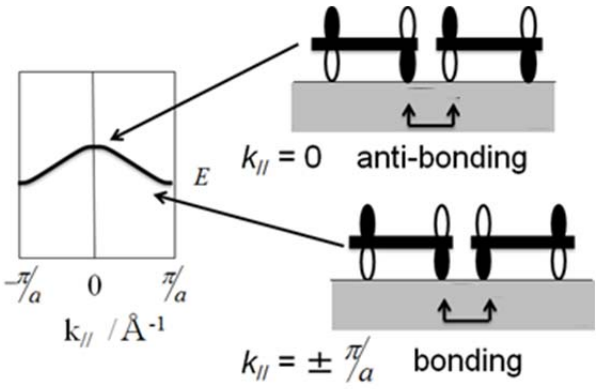

Fig. 6.6: Schematic images of band formation of the L2 level.

first layer of PbPc film lays flat to the substrate. The origin of the L2 is π* orbitals of PbPc. As shown as **Fig.5.3**, monolayer of PbPc forms square lattice and the nearest intermolecular distances are ~1.4 nm. If π* molecular orbitals of neighboring PbPc molecules interact together, we can explain the negative orbitals of L2. P_Z orbitals form π bands in the solid material. Analogy with the fact, we can illustrate the concept in a schematic way in **Fig.6.6**. We must consider the effect of the substrate on the delocalization of L2 level. Interactions of the neighboring π* orbitals of the film seems to be small. It is because that there are C-H bonds exist between π* orbitals. Therefore, electrons in π* may be repelled and not extend to the neighboring molecules. One of the possible explanation is that L2 states are not π* molecular orbitals but SAMO states like C_{60}/Cu(111) [92-95]. The difference of L2 (π*) and HOMO (π) can be explained that L2 is delocalized inter-molecular state thus overlapping integral is large but localized HOMO state only has small overlapping integral. Further STM/STS study may answer the hypothesis is correct or not. Another possibility is that localized π* molecular orbitals have substrate-mediated interactions. In **section 3.4**, we have shown that electronic levels of adsorbed molecules are broadening by molecule-surface interactions, even in weak chemisorption case [59]. On pentacene/metal surfaces HOMO shows

dispersions by surface mediated interactions [80]. There are discussions about unoccupied electronic structures of graphite, but L2 seems in the band gaps at the Γ point. So, molecule-substrate interactions seem small. But, we have observed indirect transitions via π* state of graphite on clean HOPG surface and indirect transition from HOMO-1 via π* on PbPc/HOPG surface at the Γ point, by 2PPE [18]. If we think interactions with substrate, high wave number comportments may efficiently mixing the bulk structures by phonon mediated interactions. If $k_{//} = \pi/a$, neighboring π*orbitals has same phase thus bonding is formed with mixing substrate bands and intensity is stronger than $k_{//} = 0$.

6.4 Estimation of the spatial extent of the L2 state

Finally, we consider real space extent of the L2 electrons. We have observed negative distribution of the L2 state. The intensity distribution of the L2 is not homogeneous and shows strong angle dependence. The intensity is strong in the range of 5~10 degree; correspond to 0.1~0.2 Å^{-1}. From the inverse Fourier transform, the spatial extent of the electrons are described as [41]

$$\psi(x) = \int \psi(k_{//}) e^{-ik_{//}x} dk \qquad (6.1)$$

thus the spatial extent of the excited electron can be estimated. Recent hi-resolution ARPES of PTCDA/Ag(110) enables to discuss the topography of orbitals from deconvoluted photoemission spectra [101]. From photoelectrons with E_k = 2.90 eV and emission angles θ = 10° from normal has wave moments of $k_{//}$ = 0.15 Å^{-1}. Thus, from the relation $\lambda = 2\pi / k_{//}$, the photoelectrons spread to 4.2 nm in real space. Therefore, the angle-distribution of photoelectrons in L2 suggests that electrons excited in L2 spread among several molecules. Thus, the L2 state shows intermediate behaves between

delocalized free-electrons (band conduction) and localized state (hopping). The result is agree with proposal mechanism by an electron conductive measurement [102].

6.5 Chapter summary

In this chapter, monolayer of lead phthalocyanine (PbPc) film on graphite (HOPG) surface is investigated by Micro-spot angle-resolved 2 photon photoelectron spectroscopy (micro-spot AR-2PPE). We found negative dispersions of an unoccupied level (L2) on film, which derived from LUMO+2 state of PbPc. On the other hand, HOMO state is localized and has no dispersion. The result suggests that L2 is delocalized by intermolecular interactions at the interfaces and extent of wave-function may determine localization and delocalization of the states. The L2 level is weak at shorter wave number (long wavelength) and intense at high wave number (short wavelength). From relations between intense and emission angle of the photoelectron of L2, we estimate extent of the wave-function in real space. From the analysis, we estimated that excited electrons to the L2 level are delocalized among several molecules.

7. Conclusion

In this thesis, I tried to reveal the nature of unoccupied levels at the interfaces because that the level has important role in electron transportations in functional organic materials. We focused on the energy positions and dispersions of such levels. To get reproducible experimental results, we have developed micro-spot 2PPE equipment and tried scanning imaging and angle- resolved 2PPE with high reproducibility. We measured unoccupied levels on PbPc/HOPG interfaces with varying coverage from bare surface to monolayer. Because of their well-ordered structures, we can ignore problem of effect on structure differences during the experiments.

From section 3, we observed that the resonance effect from a occupied level in the film to an unoccupied level in the film. The L2 peak is not observed with photon energy below H0-L2 energy difference. The result suggests that the L2 level in the interfaces is excited in the film, not from the substrate.

From section 4, we found that the L0/L1 level of the 0.3ML film has lateral inhomogeneity even in the well-ordered films in the structural view point. Obtained results shows intermolecular interactions effect on the electronic levels of the L0/L1 states and IPS1. Our results suggest that structural fluctuation of nm order has strong influences on the electronic structures.

From section 5, we confirmed that IPS band structures on well-ordered film structures effect on the periodic potential of the film. From a simple Kronig-penny model, we can explain reduce of their binding energy and heavier effective mass of the IPS.

From section 6, we observed negative dispersions of the L2 state. The results show delocalized nature of the L2. We also found that the observed momentum distribution of

electrons in the L2 state is not homogeneous but strongly enhanced in high momentum numbers. The result shows the wave function of L2 is spread among several molecules. The result agrees with the concept between band model and hopping model.

These experiments revealed interesting behaves of unoccupied states at the interfaces. However, obtained results are not enough to generalize all organic/inorganic interfaces, because of infinite number of organics are exist and their interactions between organic-substrate and molecules are case by case. Thus further studies of different samples are required to obtain generalizable results.

References

[1] H. Ishii, K. Sugiyama, E. Ito, K. Seki, Adv. Mater. **11**, 605 (1999).

[2] W.R. Salaneck, K. Seki, A. Kahn, J. J. Pireaux, *Conjugated Polymer and Molecular Interfaces* (Marcel Dekker, New York, 2002).

[3] W.R. Salaneck, S. Stafström, J-L. Brédas, *Conjugated Polymer surfaces and Interfaces* (Cambridge University Press, 2003).

[4] H. Lüth, *Surfaces and Interfaces of Solids* (Springer-Verlag, Berlin Heidelberg 1993).

[5] G.A. Somorjai, Y. Li, *Introduction to Surface Chemistry and Catalysis* (John Wiley & Sons, 2010)

[6] S. Hüfner, *Photoelectron Spectroscopy* (Springer-Verlag, Berlin 2003).

[7] S. Braun, W.R. Salaneck, M. Fahlman, Adv. Matter. **21**, 1450 (2009).

[8] N. Ueno, S. Kera, Prog. Surf. Sci. **83** (2008) 490.

[9] U. Bovensiepen, H. Petek, M. Wolf, *Dynamics at Solid State Surfaces and Interfaces vol. 1: Current Developments* (Willy-VCH, Weinheim, 2010).

[10] X. -Y. Zhu, Surf. Sci. Rep. **56**, 1 (2004).

[11] M. Muntwiler, Q. Yang, X.-Y. Zhu, J. Electron Spectrosc. Relat. Phenom. **174**, 116 (2009).

[12] K. Giesen, F. Hage, F.J. Himpsel, H.J. Riess, W. Steinmann, Phys. Rev. Lett. **55**, 300 (1985).

[13] H. Petek and S. Ogawa, Prog. Surf. Sci. **56**, 239 (1997).

[14] S. Pawlik, M. Bauer, M. Aeschlimann, Surf. Sci. **377-379**, 206 (1997).

[15] T. Munakata, T. Masuda, N. Ueno, A. Abdureyim, Y. Sonoda, Surf. Sci. **507-510** (2002) 434.

[16] T. Munakata, T. Sugiyama, T. Masuda, N. Ueno, Phys. Rev. B 68 (2003) 165404.

[17] I. Yamamoto, M. Mikamori, R. Yamamoto, T. Yamada, K. Miyakubo, N. Ueno, T. Munakata, Phys. Rev. B 77 (2008) 115404.

[18] M. Shibuta, K. Yamamoto, K. Miyakubo, T. Yamada, T. Munakata, Phys. Rev. B 80 (2009) 113310.

[19] M. Shibuta, K. Yamamoto, K. Miyakubo, T. Yamada, T. Munakata, Phys. Rev. B 81 (2010) 115426.

[20] I. Yamamoto, N. Matsuura, M. Mikamori, R. Yamamoto, T. Yamada, K. Miyakubo, N. Ueno, T. Munakata, Surf. Sci. **602**, 2232 (2008).

[21] R. Yamamoto, I. Yamamoto, M. Mikamori, T. Yamada, K. Miyakubo, T. Munakata, Surf. Sci. **605**, 982 (2011).

[22] C. Kittel, *Introduction to Solid State Physics* (Wiley, New York 2005).

[23] K. Nomura, H. Ohta, A. Takagi, T. Kimiya, M. Hirano, H. Hosono, Nature 432, **488** (2004).

[24] O.D. Jurchescu, M. Popinciuc, B.J. van Wees, and T.T. M. Palstra: Adv. Mater., 19, 668 (2007).

[25] J. Takeya, M. Yamagishi, Y. Tominari, R. Hirahara, Y. Nakazawa, T. Nishikawa, T. Kawase, T. Shimoda, S. Ogawa, Appl. Phys. Lett. **90**, 102120 (2007).

[26] M. Yamagishi, J. Soeda, T. Uemura, Y. Okada, Y. Takatsuki, Y. Nakazawa, K. Takimiya, J. Takeya, Phys. Rev. B **81** 161306(R) (2008).

[27] S. Machida, Y. Nakayama, S. Duhm,Q. Xin, A. Funakoshi, N. Ogawa, S. Kera, N. Ueno, H. Ishii, Phys. Rev. Lett. **104**,156401 (2010).

[28] Ding, H.; Reese, C.; Mäkinen, A. J.; Bao, Z.; Gao, Y. Appl. Phys. Lett. 2010, 96, 222106.

[29] C.H. Schwalb, S. Sachs, M. Marks, A. Schöll, F. Reinert, E. Umbach, U. Höfer, Phys. Rev. Lett. **101**, 146801 (2008).

[30] S. Sachs, C.H. Schwalb, M. Marks, A. Schöll, F. Reinert, E. Umbach, U. Höfer, J. Chem. Phys. **131**, 114701 (2009).

[31] M. Marks, N.L. Zaitsev, B. Schmidt, C.H. Schwalb, A. Schöll, I.A. Nechaev, P.M. Echenique, E.V. Chulkov and U. Höfer, Phys. Rev. B **84**, 081301 (2011).

[32] Q. Yang, M. Muntwiler, X.-Y. Zhu, Phys. Rev. B **80**, 115214 (2009).

[33] E. Varene, I. Martin, P. Tegeder, J. Phys. Chem. Lett. **2**, 252 (2011).

[34] E.A. Muller, J.E. Jhons, B.W. Caplins, C.B. Harris, Phys. Rev. B **83**, 165422 (2011).

[35] M.P. Steele, L.L. Kelly, N. Ilyas, O.L.A. Monti, J. Chem. Phys. **135**, 124702 (2011).

[36] M. Shibuta, K. Miyakubo, T. Yamada, T. Munakata, J. Phys. Chem. C **115**, 19269 (2011).

[37] K. Boger, M. Winelt, T. Fauster, Phys. Rev. Lett. **92**, 126803 (2004).

[38] M. Roth, T. Fauster, M. Weinelt, Appl. Phys. A **88**, 497 (2007).

[39] J. Güdde, M. Rohleder, T. Meier, S.W. Koch, U. Höfer, Science **318**, 1287 (2007).

[40] D.F. Padowitz, W.R. Merry, R.E. Jordan, C.B. Harris, Phys. Rev. Lett. **69**, 3583 (1992).

[41] P. Szymanski, S. Garret-Roe, C.B. Harris, Prog. Surf. Sci. **78**, 1 (2005).

[42] J. Stähler, C. Gahl, U. Bovensiepen, M. Wolf, J. Phys. Chem. B 110, 9637 (2006).

[43] S. Ryu, J. Chang, H. Kwon, S.K. Kim, J. Vac. Sci. Tecnol. A **24**, 1454 (2006).

[44] J.E. Johns, E. Muller, M.J. Frechet, C.B. Harris, J. Am. Chem. Soc. **132**, 15720 (2010).

[45] S. Kera, H. Fukagawa, T. Kataoka, S. Hosoumi, H. Yamane, N. Ueno, Phys. Rev. B **75**, 121305(R) (2007).

[46] G. Attard, C. Barnes, *Surfaces* (Oxford University Press, New York 1998).

[47] W. Demtröder, *laser spectroscopy vol. 1: Basic Principles* (Springer-Verlag, 2008).

[48] J. Lehmann, M. Merschdorf, A. Thon, S. Voll, W. Pheiffer, Phys. Rev. B **60**, 17037 (1999).

[49] B. Reihl, J.K. Gimzewski, J.M. Nicholls, E. Tosatti, Phys. Rev. B **33**, 5770 (1986).

[50] I. Schäfer, M. Schlüter, M. Skiboeski, Phys. Rev. B **35**, 7663 (1987).

[51] R. Claessen, H. Carstensen, M. Skibowski, Phys. Rev. B **38**, 12582 (1988).

[52] N.A. Holzwarth, S.G. Louie, S. Rabii, Phys. Rev. B **26**, 5382 (1982).

[53] R.F. Willis, B. Fitton, G.S. Painter, Phys. Rev. B **9**, 1926 (1974).

[54] R.C. Tatar, S. Rabii, Phys. Rev. B **25**, 4126 (1982).

[55] F. Maeda, T. Takahashi, H. Ohsawa, S. Suzuki, H. Suematsu, J. Phys Chem. Solids **69**, 2996 (2008).

[56] G. Moos, C. Gahl, R.Fasel, M. Wolf, T. Hertel, Phys. Rev. B **38**, 12582 (1988).

[57] S. Pagliara, G. Galimberti, S. Mor, M. Montagnese, G. ferrini, M.S. Grandi, P. Galinetto, F. Parmigiani, J. Am. Chem. Soc. **133**, 6318 (2011).

[58] M. Montagnese, S. Pagliara, S. dal Conte, G. Galimberti, G. Ferrini, F. Paramigiani, arXiv:0910.4473v2.

[59] H. –L. Dai, W. Ho, *Laser spectroscopy and photo-chemistry on metal surfaces Part: 1*, chapter5 (world scientific, Singapore 1994).

[60] J. Güdde, U. Höfer, Prog. Surf. Sci. **80**, 49 (2005).

[61] M. J. Seaton, Rep. Prog. Phys. **46**, 167 (1983).

[62] C. Foot, *Atomic Physics* (Oxford University Press, New York 2005).

[63] E.V. Chulkov, V.M. Silkin, P.M. Echenique, Surf. Sci. **437**, 330 (1999).

[64] M. C. Desjonquères, D. Spanjaard, *Concepts in Surface Physics* (Springer-Verlag, Berlin Heidelberg 1995).

[65] T. Munakata, T. Sugiyama, T. Masuda, M. Aida, N. Ueno, Appl. Phys. Lett. **85**, 3584 (2004).

[66] T. Sugiyama, T. Sasaki, S. Kera, N. Ueno, T. Munakata, Appl. Phys. Lett. **89**, 202116 (2006).

[67] T. Sugiyama, T. Sasaki, S. Kera, N. Ueno, T. Munakata, Chem. Phys. Lett. **449**, 319 (2007).

[68] N. Papageogiou, Y. Ferro, E. Salomon, A. Allouche, J.M. Layet, Phys. Rev. B **68**, 235105 (2003).

[69] K. Shudo and T. Munakata, Phys. Rev. B **63**, 125324 (2001).

[70] K. Shudo, S. Takeda, and T. Munakata, Phys. Rev. B **65**, 075302 (2002).

[71] M. Kutschera, M. Weinelt, M. Rohlfing, and T. Fauster, Appl. Phys. A **88**, 519 (2007)

[72] Y. Zhang, X. Cai, X. Zhang, H. Xu, Z. Liu, J. Jiang, Inter. J. Quantum Chem. **107**, 952 (2007).

[73] H. Yamane, H. Honda, H. Fukagawa, M. Ohyama, Y. Hinuma, S. Kera, K.K. Okudaira, N. Ueno, J. Electr. Spectrosc. Relat. Phenom. **137-140**, 223 (2004).

[74] A. Nilsson, L.G.M. Pettersson, Surf. Sci. Rep. **55**, 49 (2004)

[75] S. Link, A. Scholl, R. Jacquemin, W. Eberhardt, Solid State Comm. **113**, 689 (2000).

[76] D. Cahen, A. Kahn, E. Umbach, Mater. Today **8**, 32 (2005).

[77] I.G. Hill, A. Kahn, Z.G. Soos, R.A. Pascal, Jr., Chem. Phys. Lett. **327**, 181 (2000).

[78] A. Groß, Theoretical Surface Science A Microscopic Perspective (Springer-Verlag, Berlin Heidelberg 2003).

[79] Y. Sonoda, T. Munakata, Chemical Physics Letters 445 198 (2007).

[80] H. Yamane, D. Yoshimura, E. Kawabe, R. Sumii, K. Kanai, Y. Ouchi, N. Ueno, K. Seki, Rev. B **76**, 165436 (2007).

[81] M.P. Steele, M.L. Blumenfeld, N. Ilyas, O.L.A. Monti, J. Phys. Chem. Lett. **1**, 2011 (2010).

[82] Th. Fauster, Ch. Reuß, I.L. Shumay, M. Weinelt, F. Theilmann, A. Goldmann, Phys. Rev. B **61**, 16168 (2000).

[83] K. Schouteden, C. Van Haesendonck, Phys. Rev. Lett. **103**, 266805 (2009).

[84] C. Stadler, S. Hansen, I. kröger, C. Kumpf, E. Umbach, Nature Physics 5 (2009) 153.

[85] J.D. Baran, J.A. Larsson, R.A.J. Woolley, Yan Cong, P.J. Moriarty, A.A. Cafolla, K. Schulte, V.R. Dhanak, Phys. Rev. B **81**, 075413 (2010).

[86] C. Ludwig, R. Stromaier, J. Petersen, B. Gompf, and W. Eisenmenger, J. Vac. Sci. Technol. B **12**, 1963 (1994).

[87] R. Strohmaier, C. Ludwig, J. Petersen, B. Gompf, W. Eisenmenger, J. Vac. Sci. Technol. B **14**, 1079 (1996).

[88] F. Bisio, M.Nyvlt, J. Franta, H. Petek, J. Kirschner, Phys. Rev. Lett., **96**, 087601 (2006).

[89] A. Ünal, C. Tusche, S. Ouazi, S. Wedekind, C. T. Chiang, A. Winkelmann, D. Sander, J. Henk, J. Kirschner, Phys. Rev. B **84**, 073107 (2011).

[90] J. E. Ortega, A. Mugarza, V. Repain, S.Rousset, V. Pérez-Dieste, A. Mascaraque, Phys. Rev. B **65** (2002) 165413.

[91] O. Sánchez, J. M. García, P. Segovia, J. Alvarez, A. L. Vázquez de Parga, J. E. Ortega, M. Prietsch, R. Miranda, Phys. Rev. B **52** (1995) 7894.

[92] D. Velic, A. Hotzel, M. Wolf, G. Ertl, J. Chem. Phys. **109**, 9155 (1998).

[93] M. Feng, J. Zhao, H. Petek, Science **320**, 359 (2008).

[94] J. Zhao, M. Feng, J. Yang, H. Petek, ACS Nano **3** 853 (2009).

[95] W.L. Chan, J. Tritsch, A. Dolocan, M. Ligges, L. Miaja-Avila, X.-Y. Zhu, J. Chem. Phys. **135**, 031101 (2011).

[96] G.D. Dutton, D.B. Dougherty, W. Jin, J.E. Reutt-Robey, S.W. Robey, Phys. Rev. B **84**, 195435 (2011).

[97] M. Fox, *Optical Properties of Solids* (Oxford University Press, Oxford 2010).

[98] U. Bovensiepen, C. Gahl, M. Wolf, J. Phys. Chem. B **107**, 8706 (2003).

[99] U. Bovensiepen, C. Gahl, J. Stähler, M. Bockstedte, M. Meyer, F. Baletto, S. Scandolo, X.-Y. Zhu, A. Rubio, M. Wolf, J. Phys. Chem. C **113**, 979 (2009).

[100] N.W. Ashcroft, N.D. Mermin, *Solid State Physics* (Thomson Learning, 1976).

[101] P. Puschnig, E.–M. Reinisch, T. Ules, G. Koller, S. Soubatch, M. Ostler, L. Romaner, F. S. Tautz, C. Ambrosch-Draxl, M.G. Ramsey, Phys. Rev. B **84**, 235427 (2011).

[102] M. Yamagishi, J. Soeda, T. Uemura, Y. Okada, Y. Takatsuki, T. Nishikawa, Y. Nakazawa, I. Doi, K. Takimiya, J. Takeya, Phys. Rev. B. **81**, 161306 (R) (2010).

Publications

1. *Lateral inhomogeneity of unoccupied states for PbPc films*
   R. Yamamoto, I. Yamamoto, M. Mikamori, T. Yamada, K. Miyakubo, T. Munakata, Surf. Sci. **605**, 982 (2011).

2. *Dispersions of image potential states on clean graphite and on lead phthalocyanine surfaces*
   R. Yamamoto, T. Yamada, M. Taguchi, H. S. Kato, T. Munakata, (submitted).

3. *Dispersions of molecular derived unoccupied state on lead phthalocyanine surfaces*
   R. Yamamoto, T. Yamada, M. Taguchi, H. S. Kato, T. Munakata, (in preparation).

4. *Resonant two-photon photoemission study on electronically excited states at an interface of lead phthalocyanine (PbPc)/graphite*
   I. Yamamoto, M. Mikamori, R. Yamamoto, T. Yamada, K. Miyakubo, N. Ueno, T. Munakata, Phys. Rev. B **77**, 115404 (2008).

5. *Imaging of electronic structure of lead phthalocyanine films studied by combined use of PEEM and Micro-UPS*
   I. Yamamoto, N. Matsuura, M. Mikamori, R. Yamamoto, T. Yamada, K. Miyakubo, N. Ueno, T. Munakata, Surf. Sci. **602**, 2232 (2008).

Acknowledgement　謝辞

(Written in Japanese)
本研究を行う上で多くの方々にご支援をいただきました。

指導教授の宗像利明先生には、お忙しい中懇切丁寧にご指導をいただきました。実験技術や結果の考察に加えまして、大学院の生活の中でも様々な助言をいただきました。ご迷惑をおかけいたしましたことも多いかと存じます。大学院で充実した日々を過ごせましたのは先生のご指導おかげです。お礼を申し上げます。

山田剛司助教には学部生のころから、装置のトラブル修理や実験結果の解釈に悩んだ時など多くの難問を解決していただきました。更に研究を進めるうえで必要な概念の多くを丁寧に教えていただきました。ご迷惑をおかけいたしましたことも多いかと存じますが、親身に相談にのってくださり、お礼を申し上げます。

山本勇博士、渋田昌弘博士には公私ともに沢山お世話になりました。生意気なわたくしがこれまでの実験をなんとか進めることができましたのは、お二方の寛容さと忍耐のおかげです。ありがとうございました。

宮久保圭祐准教授にはお忙しい中でも、困ったときに惜しまず様々な助けをいただきました。また、物理化学の幅広い見方を教えていただきました。ここにお礼を申し上げます。

本論文の実験および学部・修士課程の実験を行うにあたりまして多くの方々と共同で実験を行いました。山本勇博士、三賀森雅和氏、阿弥曜平氏、古澤潤氏、南隆文氏、山西正将氏にお礼申し上げます。ご迷惑をおかけいたしたことも多々ありますが、みなさまの寛容のおかげでなんとか本研究を終えることができました。ありがとうございます。

研究の考察をまとめるうえで、加藤浩之准教授、大山浩准教授、蔡徳七助教の先生方に貴重なご指導をいただきました。ここにお礼を申し上げます。

表面化学研究室の学生・秘書のみなさまには数えきれないほどの助けをいただきました。ここにそのすべてを記すことは不可能ですのでお礼だけの馬蹄と思います。ありがとうございます。

小林光教授、中澤康浩教授の両先生に年末年始のお忙しい中、多くのご指導をいただきました。両先生と中澤研のみなさまにお礼を申し上げます。

多くの方々の助けがありまして、本研究をまとめることができました。ここに名前を記せなかった方々にもお礼を申し上げます。

最後に、どんなに自分勝手で迷惑をかけても文句も言わずに暖かく見守ってくれた父母と妹に感謝の気持ちを伝えたいと思います。